Build orientation, part size geometry, and scan path influence on the microstructure and fatigue life of Ti-6Al-4V fabricated by Electron Beam Melting

A Thesis Presented for the
Master of Science
Degree
The University of Tennessee, Knoxville

Andrew Harrison Chern
May 2018

Copyright © 2018 by Andrew Harrison Chern
All rights reserved.

ACKNOWLEDGEMENTS

I would like to start by thanking my advisor, Dr. Chad E. Duty, for his assistance, guidance, and patience. Dr. Duty went in front of the graduate program director for my admission to the graduate program and I hope that my work has met his expectations and his efforts were worth it. I thoroughly enjoyed working and studying under him for my graduate studies. I would also like to thank Dr. Peeyush Nandwana of ORNL and Dr. Robert McDaniels of VEXTEC for their technical expertise, direction, and always challenging me to do my best work and push to find answers and solutions. Without them, this project would not have been possible and I would not have the technical knowledge I have today.

I would like to extend a sincere thank you to my graduate committee, Dr. Ryan Dehoff, Dr. Peter Liaw, and Dr. Sudarsanam Suresh Babu for their guidance and advice. I would also like to thank Dr. Michael Kirka, Sean Yoder, Dr. John Dunlap, and Zane Palmer for their assistance with the project content and equipment training. And for always having positive attitudes and making coming to the office enjoyable, I would like to acknowledge my fellow members of our lab - Christine, Dylan, James, Vidya, and Zeke.

Lastly, I would like to thank my parents and family for supporting me throughout my graduate and undergraduate studies. It was not always easy, but their unwavering support always gave me the extra push to keep trying and not to stop until I had achieved my goals.

This work was funded by the Department of the Navy and VEXTEC Corporation.

ABSTRACT

Electron beam melting (EBM), a powder bed fusion process, is a rapidly-developing metal additive manufacturing method that allows for fabrication of complex geometries directly from a computer file that would be difficult or impossible to fabricate by traditional methods. EBM holds significant interest in the aerospace industry for the high-strength titanium alloy, Ti-6Al-4V, because of its promising opportunity to reduce buy-to-fly ratios. However, a fundamental understanding of the fatigue-damage tolerance, underlying mechanisms, and impact of processing conditions is required for use of EBM fabrication of critical flight components. To investigate how the EBM process affects components, different parameters were varied and the resulting microstructure and mechanical properties were characterized using 4-point bend fatigue tests, tensile tests, Vickers microhardness indentations, scanning electron microscopy, and optical microscopy.

The orientation, scan path, and surface finish were varied and the effects on microstructure, tensile properties, and fatigue behavior are reported and discussed. As expected, the surface roughness left by the EBM fabrication adversely impacts the fatigue behavior and sufficient machining is required to remove all surface roughness effects. It was discovered that the build orientation affects the tensile ductility and fatigue life, but the strength and hardness are largely independent of orientation. The EBM Ti-6Al-4V shows similar fatigue life to conventional material, but is limited by porosity defects. The altered processing parameters affected the fatigue behavior, but promising results indicate that EBM can be a viable manufacturing method for flight critical components.

TABLE OF CONTENTS

1. Introduction and Background 1
1.1. Ti-6Al-4V 1
1.2. Electron Beam Melting Additive Manufacturing 6
1.3. Fatigue 9
1.4. Analysis Techniques, Motivation, and Purpose 12
2. Literature Review 14
2.1. Ti-6Al-4V Microstructure 14
2.1.1. Crystal Structure and Phases 14
2.1.2. Phase Transformations 15
2.1.3. Traditionally Manufactured Microstructures 18
2.2. Fatigue Mechanisms and Properties of Ti-6Al-4V 22
2.3. Electron Beam Melting 26
2.3.1. EBM Microstructural Evolution and Mechanical Properties 27
2.3.2. Electron Beam Melting Defects 31
2.3.3. Selected EBM Parameters that Effect Microstructure and Mechanical Properties 32
2.4. Fatigue Behavior of EBM Fabricated Ti-6Al-4V 40
2.4.1. Orientation Effects – As-Built Surface with As-Built Material 46
2.4.2. Orientation Effects – Machined Surface with As-Built Material 48
2.4.3. Machining Effects - Machined Surface with As-Built Material 50
2.4.4. HIP Effects 52
2.4.5. EBM Fatigue Properties – Summary 56
2.4.6. Fatigue Endurance Limits 58
2.5. Comparison to Other Common Aerospace Alloys 61
2.6. Literature Review Conclusions 63
3. Materials and Methods 66
3.1 Build Design and EBM Variables of Interest 66
3.1.1. Build Design 66
3.1.2. Build Orientation 67
3.1.3. Local Surface Finish 68
3.1.4. Scan Path 68
3.1.5. Part Geometry and Wall Thickness 68
3.1.6. Materials 69
3.1.7. EBM Build Parameters 69
3.1.8. Experimental Matrix - Four Point Bend Fatigue Tests 72
3.2. Procedure 72
3.2.1. Microstructure Characterization 72
3.2.2. Vickers Microhardness Measurements 73
3.2.3. Tensile Tests 74
3.2.4. Finite Element Computations and Statistical Analysis 74
3.2.5. Four Point Bend Fatigue Test Specimen Preparation and Test Set Up 76
4. Results and Discussion 83

4.1 Microstructure 83
4.2 Vickers Hardness Indentations 85
4.3 Tensile Tests 88
4.4 ANSYS Structural Simulation and Stress Concentration Factor 91
4.5. 4-Point Bend Fatigue Results 94
4.5.1. Surface Roughness Effects 94
4.5.2. Effects of Build Orientation 102
4.5.3. Effects of Build Geometry and Volume on Fatigue Life 110
4.5.4. Effects of Scan Path on Fatigue 111
4.5.5. Comparison to Conventional Ti-6Al-4V 118
5. Recommended Practice for Fatigue Applications 122
5.1. Current Recommended Best Design Practice 122
5.2. Surface Roughness 123
5.3. Porosity 126
5.4. Microstructure 127
6. Conclusions 130
List of References 133
Appendix 149
Vita 154

LIST OF TABLES

Table 1. Mechanical Properties of Conventionally Processed Ti-6Al-4V 21
Table 2. Chemical Composition of Ti-6Al-4V Powder..... 70
Table 3. Summary of the EBM Build Process Conditions and Parameters..... 71
Table 4. Experimental Test Matrix – 4 Point Bent Fatigue Testing 72
Table 5. Average Tensile Properties..... 88
Table 6. ANSYS FE Analysis Parameters..... 92
Table 7. Fatigue Data Reference Chart..... 150
Table 8. Example Calculations for Crack Growth Rate, da/dN..... 153

LIST OF FIGURES

Figure 1. Comparison of different manufacturing processes used to produce a complex turbine blisk [19]. 5
Figure 2. Schematic of the EBM machine. 8
Figure 3. Figure demonstrating increasing use of Ti alloys in Boeing's fleet. Operating empty weight percent of Titanium has steadily increased over time [31]. 11
Figure 4. Pseudo-phase diagram of Ti-6Al-4V showing the β transus, α + β phase fields, martensitic start temperature as a function of V content. Figure adapted from [38]. 15
Figure 5. Optical Micrographs of Lamellar Ti-6Al-4V (a.) [49] and Widmanstätten or basket weave Ti-6Al-5Nb (b.) [50]. In both images, the α phase is the lighter grains and the β phase is darker. 19
Figure 6. An optical micrograph of a fully martensitic α′ structure obtained by cooling at 525°C/s [42]. 20
Figure 7. An optical micrograph of the bimodal (duplex) microstructure of Ti-6Al-4V [37]. 22
Figure 8. An optical micrograph demonstrating a coarse lamellar microstructure's crack path tortuosity (a) and a schematic of the differing crack paths between α-β annealed and β annealed microstructures (b) [37]. 23
Figure 9a-c. Crack formation and the role of grain boundaries and macrozones [60]. 24
Figure 10. Young Modulus (stiffness) of α Ti as a function of loading angle [6]. 25
Figure 11. Electron beam melting cooling curve and thermal history of Ti-6Al-4V. Figure adapted from [42] and [79] 28
Figure 12. Optical micrographs of EBM manufactured Ti-6Al-4V where (a) is an image of the X-Y plane and (b) is an image of the z/build direction [80]. 29
Figure 13. Schematic of the equiaxed to columnar transition and α morphologies observed in the EBM-fabricated Ti-6Al-4V. Figure adapted from reference [10]. 30
Figure 14. Optical micrographs of gas porosity (a.) and a lack-of-fusion defect (b.) [91] 31
Figure 15. EBM process deficiencies melt ball formation (a) [20] and layer delamination (b) [93]. 32
Figure 16. Powder Reclamation system and recycling procedure of powder in EBM [94]. 33
Figure 17. Material conditions considered in the fatigue literature review. The black arrows represent a comparison made between two material conditions. 41
Figure 18. Schematic demonstrating different EBM build orientations in axial fatigue tests. 45
Figure 19. SN chart comparing build orientation of test bars with as-built surfaces and as-built material conditions. Red markers and trend lines represent horizontally oriented parts and blue markers and trend lines represent vertically oriented parts. 46
Figure 20. SEM micrograph of an EBM as-built surface. The red arrow indicates the build direction, white arrows the surface notches, and black arrow indicates loading direction in an axial fatigue test. Figure adapted from [139]. 47

Figure 21. Orientation of LOF defects in vertical and horizontal specimen with respect to different types of loading. 'Z' denotes the build direction. Figure adapted from [29]. 48
Figure 22. Fatigue behavior of as-built material/machined surface. 49
Figure 23. Optical (a.) and SEM (b.) micrographs showing EBM surface roughness [144]. 50
Figure 24. SN curve demonstrating machining effects on fatigue behavior..... 51
Figure 25. SN curve demonstrating fatigue behavior of HIPed and as-built parts with as-fabricated surfaces. 53
Figure 26. Fatigue Behavior of HIPed components with as-built and machined surfaces. 55
Figure 27. Compiled fatigue data of EBM fabricated Ti-6Al-4V in various states of post-processing including machining and HIP. 57
Figure 28. Endurance limits (cycles > 10^7) of material in various orientations and post-process conditions. Error bars on EBM categories represent a range of endurance limits found in literature if available. Error bars on the reference categories represent standard deviations of literature values. All tests used R ratio = 0.1..... 59
Figure 29. Endurance limits as a function of ultimate tensile strength for various alloys and EBM material conditions. Figure adapted from [152]..... 61
Figure 30. Plot of the fatigue ratio as function of ultimate tensile strengths of EBM manufactured parts and traditional aerospace alloys. Figure adapted from [152].... 63
Figure 31. Computer models of the build design (a.) and example 4-point bend test specimen (b.). The numbers (1 and 2) in a. represent parts with different wall thicknesses. Dimensions shown are given in inches..... 66
Figure 32. Test specimen orientation where 'H' indicates an example horizontally oriented specimen and 'V' an example vertically oriented specimen. Figure adapted from [154]..... 67
Figure 33. Arcam Q10 Machine used in this study. 70
Figure 34. EBM build prior to machining. 71
Figure 35. Geometry of tensile test samples. The sample thickness was 0.125" and the dimensions shown are in inches. Note that the geometry does not adhere to ASTM E8 standards. 75
Figure 36. Example set up of water jet abrasive machining of a test specimen (a.) and OMAX 2626 water/abrasive machining center. 76
Figure 37. Schematic of different surface preparations and conditions for 4-point bend fatigue testing..... 77
Figure 38. 4–Point bend test schematic and corresponding shear-moment diagrams. 79
Figure 39. Schematic of the 4-point bend test set up and important dimensions. 80
Figure 40. Optical micrographs of the microstructure sectioned from block 1 in 2 different orthographic planes; Z (a.) and XY (b.)..... 84
Figure 41. Vickers micro-hardness measurements as a function of distance from build plate, block volume, and orientation..... 85
Figure 42. Tensile test results presented as engineering stress/engineering strain curves.88

Figure 43. Schematic of the geometric set up and loading conditions for the ANSYS FEA Simulation. 93
Figure 44. Nodal solution stress contour plot of the Von Mises Stress of the solved model. 93
Figure 45. Average cycles to failure of EBM fabricated parts with as-built surfaces compared to specimen with machined and fine-ground surfaces. The applied stress was 585 – 590 MPa. 95
Figure 46. Images showing crack initiation and crack propagation behavior of specimen with an as-fabricated surface. 95
Figure 47. SEM micrograph (a.) and optical profile (b.) of an as-fabricated EBM Surface. 96
Figure 48. An image of an as-built hole. The red circle indicates the designed 1/32" (793.75 mm) diameter. The black arrow indicates the build direction. 97
Figure 49. Average cycles to failure comparing the effects of the as-built surface in the bore of the hole to machined holes. The applied stress was 570 - 600 MPa. 98
Figure 50. Fracture surface of a fatigued specimen with an as-fabricated hole highlighting the partially-sintered powder and rough surface throughout the bore of the hole. ... 99
Figure 51. Optical image of surface roughness overlaid on a schematic of the 4-point bend loading, red arrows indicate build direction and black arrows loading direction... 101
Figure 52. Bar graph showing the build orientation's influence on fatigue life of machined specimen. 102
Figure 53. Interrupted fatigue test crack monitoring, image and crack measurments taken at 10,000 cycles. 103
Figure 54. SEM fracture surface images of vertically orientated, machined, and polished samples showing LOF defects at surface crack iniation sites near an edge (a.) and interior site (b.). 104
Figure 55. Schematic of the vertical and horizontal 4-point bend fatigue test specimen. The lines represent individual build layers. 105
Figure 56. Measured crack length as function of fatigue cycles. 106
Figure 57. Crack growth rate (microns/cycle) calculated using Secant method and plotted against average crack length. 107
Figure 58. Crack initiating at a LOF defect intercepting the surface of a vertical specimen at 10,000 cycles. 108
Figure 59. Interrupted fatigue test crack monitoring of specimen 'Vertical 1' showing multiple cracks initiating at both holes at cycle 7,000. The red arrows indicate independent cracks. 109
Figure 60. Fatigue cycles to failure of parts with different wall thicknesses. 110
Figure 61. Schematic of machining process to obtain the 'reamed hole (a.) where black arrows indicate beam scans projected onto an as-built hole. Average cycles to failure of horizontally oriented parts machined from the center large block with either reamed or machined holes (b.). Parts tested at σ = 590 MPa. 112
Figure 62. XCT scan projected onto an X-Y plane showing porosity distribution in a sample with unidirectional hatching (indicated by the black arrow). Figure adapted from [116]. 113

Figure 63. SEM micrograph of a fracture surface of a sample with a reamed hole. Crack initiation site is outlined in red and green arrows indicate surface defects the reaming process did not remove. 115
Figure 64. Sharp cavity along the bore of the sample with reamed hole remnant of the surface roughness of the as-fabricated hole. 116
Figure 65. Fracture surface images of the specimen with machined hole (a. & b.). The green arrows indicate gas pores. 117
Figure 66. Fatigue resistance of EBM material (horizontal and machined) compared to conventional Ti-6Al-4V. 118
Figure 67. Example defects observed in EBM (a.) and conventional (b.) material. 119
Figure 68. SEM images of conventional (a.) and horizontal EBM specimen (b.). Defects are indicated by green arrows in the EBM specimen crack initiation sites by red boxes. 121
Figure 69. Schematic of an example variant of the Burgers Orientation Relationship adapted from [41]. 152
Figure 70. Schematic of the Secant Method for calculating fatigue crack growth rate. Adapted from [204]. 153

1. INTRODUCTION AND BACKGROUND

1.1. Ti-6Al-4V

Titanium alloys are used extensively in the aerospace and gas turbine industries. As examples, the F22 fighter and Boeing 787 are 42 (9,000 lbs.) [1] and 15 weight percent [2] Ti alloys, respectively. The most commonly used Ti alloy is Ti-6Al-4V (6 wt% Al, 4 wt% V) comprising approximately 50% of the titanium market [3], 80% of which is used in aerospace applications [4], for its combination of high strength to density ratio, superior corrosion resistance, toughness, and workability [5]. Ti-6Al-4V is often used where high strength and fatigue damage tolerance is needed like wing attachments, compressor casings, turbine blades, and helicopter rotor attachments [5, 6]. The costs associated with extracting and forming Ti-6Al-4V to its final shape limit its wide spread use. Ti is highly reactive with O and N in the atmosphere so melting under vacuum is required. In addition, its retained high strength at elevated temperatures, low thermal conductivity (7 W/m-K as opposed to Al's 237 W/m-K [6]), and high reactivity to elements in air make it difficult and costly to machine.

Ti-6Al-4V is a dual phase alloy as its equilibrium composition at room temperature is comprised of both the hexagonal close packed (HCP) α phase and body centered cubic (BCC) β phase. In traditionally wrought Ti-6Al-4V, the microstructure consists of 85% or greater α phase [4, 7] and greater than 90% for additive manufactured Ti-6Al-4V [8-10]. The phase composition depends on the thermal history and alloying elements. The

combination of HCP and BCC crystal structures provide Ti-6Al-4V with a good combination of strength and ductility.

Titanium's use in industry is generally limited by its costs and difficulties associated with manufacturing. Titanium is difficult to melt as it has a high melting temperature of about 1670°C [6] and reactive with air and traditional refractory elements. This makes casting of titanium difficult and expensive. Titanium's high strength is beneficial for end structural applications, but the materials' retained high strength at elevated temperatures makes machining processes difficult. Forging is difficult because the flow stresses of titanium are higher than Al and steels. Many aerospace components must be machined from stock material and as much as 50-90% of the stock material ends up as chips [3]. Aerospace components can have buy-to-fly ratios, the ratio of the stock material weight that is purchased to the weight of the finished part, as high as 27:1 [11] or higher. Scrap must be thoroughly cleaned, sorted, and purified before recycling of titanium chips can be realized. With the high process costs, difficulties machining and recycling, and desire to make more efficient and lighter parts, electron beam additive manufacturing can be an economical method of manufacturing Ti-6Al-4V components. The following sections briefly discuss the materials properties that make Ti-6Al-4V difficult to machine and how EBM can alleviate those difficulties.

In addition to difficulties with extraction and melting, Titanium alloys are difficult to machine when compared to steels and aluminum alloys further contributing to its high

costs. Titanium is difficult to machine because of a number of material properties including its high strength, low thermal conductivity, low elastic modulus, and high chemical reactivity with tooling materials. The high strength of Ti alloys make it an attractive material for loading bearing applications, but make machining difficult. Ti has a high specific strength and hardness that is maintained at elevated temperatures experienced during machining [12]. This characteristic leads to increased abrasion wear physically removing tool material at a higher rate than with other alloys. This is especially pertinent with increased oxygen content. An increase in 800 ppm of Oxygen was shown to harden the primary α phase significantly reducing its machinability [13]. With an increase in strength, an increase in energy is needed to remove material leading to a higher amount of heat generated at the tool/work piece interface [12]. Temperature is the most critical parameter involved in tool wear and material damage. Temperatures can rise above 900°C when dry machining titanium [14] and can be as high as 600°C with cutting fluid [15]. At temperatures of 550°C, Ti begins to react with tool materials [16] leading to rapid tool degradation. Titanium's poor thermal conductivity, ranging from 5.5 W/m-K at 0°C to 25 W/m-K at 800°C (steels vary from 30-60 W/m-K and aluminums 170-240 W/m-K) [12], reduces the amount of heat dissipated leading to increased tool wear and microstructural damage. Common tool coatings such as TiN, TiC, Al_2O_3, ZrC, and HfC, all contain elements that are highly reactive with Titanium at elevated temperatures. The chemical reactions form a metallic bond on the tool and then break away bringing some tool material with it. This adhesion mechanism causes crater wear of the tool [13]. It is recommended to use uncoated carbide tools (WC-Co) to machine titanium [13]. Titanium alloys low elastic

modulus, about 50% of steels and Ni base alloys [6], can lead to deflection, chatter, and tolerance issues [12].

Improvements in machining titanium alloys are needed to not only increase the practicability of Ti alloys but the safety of the finished products. Machining titanium is not only expensive and slow due to rapid tool wear and required low rate of material removal, but surface defects can be introduced and impact fatigue strength. A hardened zone with recrystallized alpha grains inquired during a drilling process of an engine fan hub where temperatures reached 1200°C of a Ti-6Al-4V initiated a fatigue crack that caused catastrophic engine failure in a Pratt & Whitney JT8D-200 [17]. Special tools like coolant fed drills and CBN coatings improve machinability and tool life, but are expensive. In water jet abrasive cutting, the work piece is submerged in water keeping temperatures low but is limited in its machining capabilities.

Electron Beam Melting (EBM) additive manufacturing presents the opportunity to drastically reduce machining for certain Ti-6Al-4V parts allowing for savings on tooling, manufacturing costs, reducing the buy-to-fly ratio and the possibility of introducing surface damage inquired during machining. The inert environment of the build chamber in EBM eliminates nitride, oxide, and hydride formation. AM has been shown to be economical for low to medium build volumes of parts with high complexities [18], but build volume, limited resolution, and rough surface finish bounds EBM use, especially for fatigue critical parts. Despite some waste chips, the material removal can be significantly reduced by

initially fabricating the part by EBM and then finish with machining for surface finish and reaching final dimensions. EBM also has the potential to significantly reduce machining time leading to cost savings. As an example, the machining time of a complex shrouded blisk (Fig. 1) was reduced nearly 55% when an EBM blank was machined to final dimensions compared to a wrought blank [19].

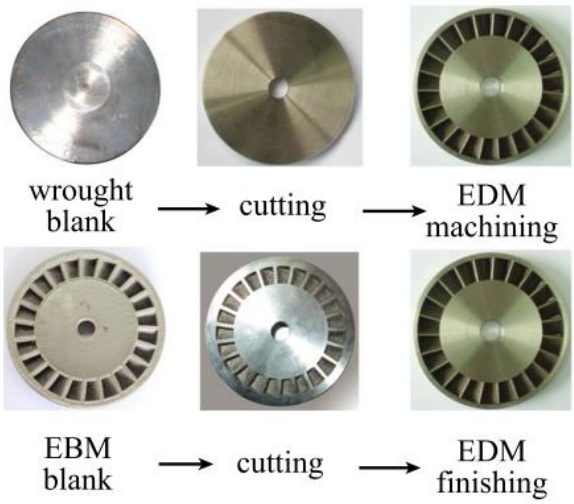

Figure 1. Comparison of different manufacturing processes used to produce a complex turbine blisk [19].

Today, additive manufacturing is limited by low build volumes, slow deposition rates, high machine costs (an Arcam machine can cost between $600,000 to $1.3 million), powder feed stock costs, and maintenance [20]. In addition, consistency in the builds and mechanical property variation limits the widespread use of AM parts. Reduction of material waste, tooling costs, machining defects, and environmental issues through less machining of complex parts, time savings in the initial prototype phase, and reduction of energy consumption by use of lighter parts that can carry the same loads all contribute to

justification of the use of AM against traditional manufacturing methods. While the costs savings may validate the initial investment in an Arcam machine for select parts, the mechanical properties and process/microstructure relationships must be better understood for EBM fabricated parts to be used in industry.

1.2. Electron Beam Melting Additive Manufacturing

Electron Beam Melting is a powder bed fusion additive manufacturing process that uses a high powered electron beam directed file to selectively melt metal powder to build a fully dense part layer-by-layer. The process was developed by Arcam AB and the first production model, the S12, became available in 2002 and later launched the A2 in 2007 designed specifically for aerospace parts [21]. With EBM, the user can upload a Computer Aided Design (CAD) file to the Arcam EBM machine and each layer is melted according to the geometry specified in the CAD file. The process allows for the design of customized components that are not limited by traditional manufacturing methods. For this, there is tremendous interest in the EBM technology in the aerospace, automotive, and biomedical industries for not only prototyping and tooling purposes, but for field service parts.

The EBM process has a number of unique characteristics that set it apart from other metal AM methods. Firstly, the build chamber is under vacuum (base pressure = $1e^{-5}$ mbar, partial pressure of He backfill = $2e^{-3}$ mbar) to provide an inert and pure environment for better chemical control of the build. Secondly, the stainless steel build platform is preheated prior to first layer deposition and each subsequent powder layer is preheated and maintained at an elevated temperature. The elevated build temperature reduces the cooling rate and acts

as an in-situ anneal, reducing residual stresses induced by the rapid solidification and martensitic microstructural features commonly observed in laser-based additive manufactured Ti-6Al-4V parts. The EBM process provides a favorable build environment and upon completion, the un-sintered powder is collected and recycled for future builds effectively eliminating any scrap metal and significantly reducing buy-to-fly ratios. In addition, the part can be created with internal channels, overhangs, and complex geometries with a minimum feature size of 100 – 200 μm [20].

Electrons in the EBM process are generated by a tungsten filament at an acceleration voltage of 60 kV. The electrons, traveling at nearly half the speed of light, pass by a number of magnetic coils that shape, focus, and then deflect the beam around the build plate. There are no moving mechanical parts to direct the electron beam leading to fast scan speeds (up to 1000 m/s) and high deposition rates (60 cm^3/hour) [22]. At the start of the build, powder is initially raked onto a preheated stainless steel build plate. The powder layer is then preheated by a defocused, fast scanning beam. Following the powder preheat, the outermost boundaries of the part are melted using a focused beam during the contour melt stage and then the interior of the part is melted using a hatch in-fill scan pattern, the beam scan direction rotating 90° every layer. After a layer is completed, the build plate drops in the negative Z direction and another layer, 50 - 100 μm, is then raked onto the build envelope and the process is repeated. A schematic of an EBM machine is provided in Fig. 2.

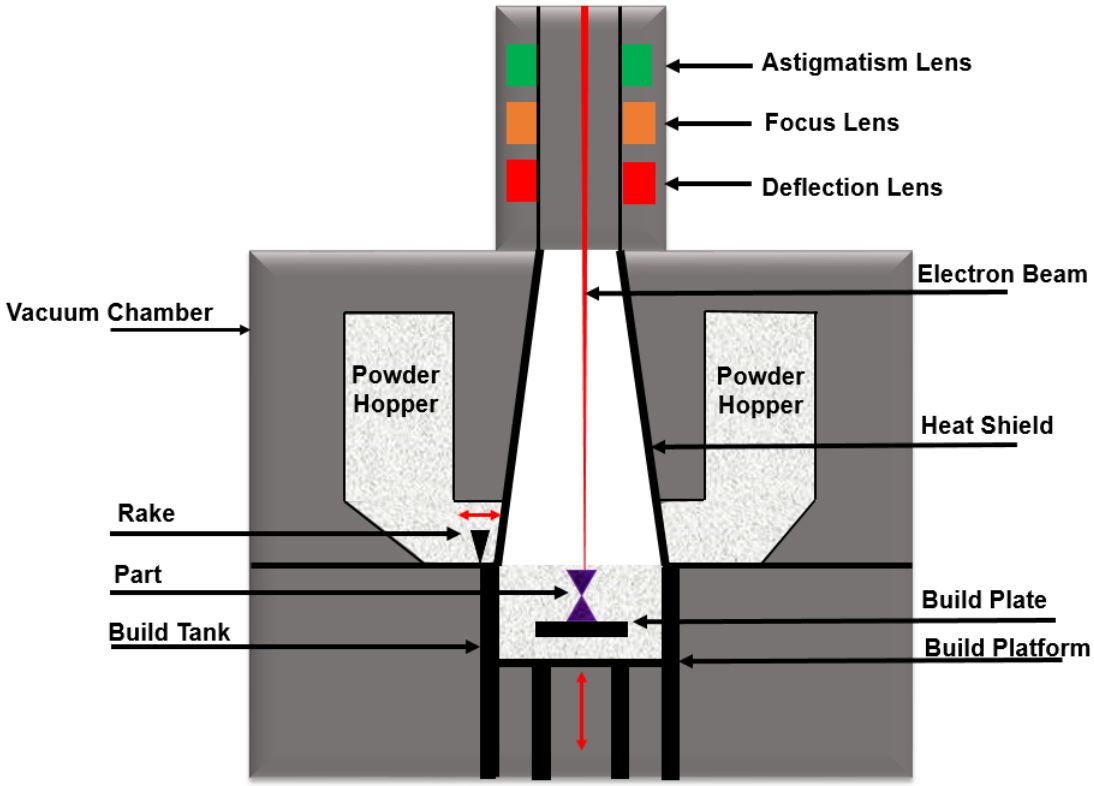

Figure 2. Schematic of the EBM machine.

Industrial aerospace manufacturers must balance the safety and costs of components. The EBM process holds potential to increase safety and decrease the cost to manufacture complex parts. Machining and melt defects that can compromise safety are reduced and buy-to-fly ratios approaching 1 are not unrealistic when fully realizing EBM's capabilities. In addition, parts can be optimized for weight savings while bearing the same loads. The EBM process is especially attractive for Ti alloys that are expensive to produce, difficult to machine, and chemically reactive. Before additive manufacturing of flight critical components (including rotating and fracture prone parts) can be realized, certifications and qualifications are needed. A major component of the certification and qualification process is understanding how process conditions, part design, build path, and post-process impact the mechanical properties [23], most important being the fatigue behavior.

1.3. Fatigue

Fatigue failures occur after a component is subjected to oscillatory loading at levels lower than that which would normally cause failure after one application. There two types of fatigue; low-cycle fatigue (LCF) and high-cycle fatigue (HCF). HCF (cycles to failure ~ 10^4 - 10^8) is characterized by high frequency cyclic loading below the yield strength of the material. LCF (cycles to failure < 10^4) occurs at higher stress levels where plastic strain is induced every cycle [24]. Fatigue afflicts many components, materials, and processes as it is estimated that 90% of all mechanical failures are caused by fatigue [25]. A variety of engineering fields are concerned with fatigue as it afflicts roads, bridges, automobiles, trains, power generation turbines, nuclear reactors, naval ships and submarines, and aerospace vehicles. Many of these components experience both HCF and LCF during

service operation. For example, although HCF has been identified as the primary mode of failure for gas turbine engines [26], an engine experiences low cycle fatigue loading during take-off, cruise, and landing cycles [27]. Thus, it is important to study both types of failures. In general, HCF behavior of a material is more sensitive to defects and crack initiation then LCF, which is crack propagation dominated [28]. However, LCF of Ti-6Al-4V has been shown to be sensitive to defects and crack initiation as well [29, 30]. This report will primarily focus on the HCF behavior of Ti-6Al-4V as it is commonly used in aerospace applications that are HCF limited, such as turbine blades and structural components.

An increased use of Ti alloys, specifically Ti-6Al-4V, has been observed in recent years in an effort to make more efficient and safe airplanes, as indicated in Fig. 3 [31]. Because of difficulties machining and processing the alloy, additive manufacturing is a promising area that could reduce the costs associated with titanium alloys. As discussed, Electron Beam Melting is an AM fabrication method of particular interest. However, certification issues hinder widespread use and a deep understanding of the process and its connection to the fatigue behavior is needed before EBM can be a viable method for fabrication of parts for fatigue applications [23, 32, 33].

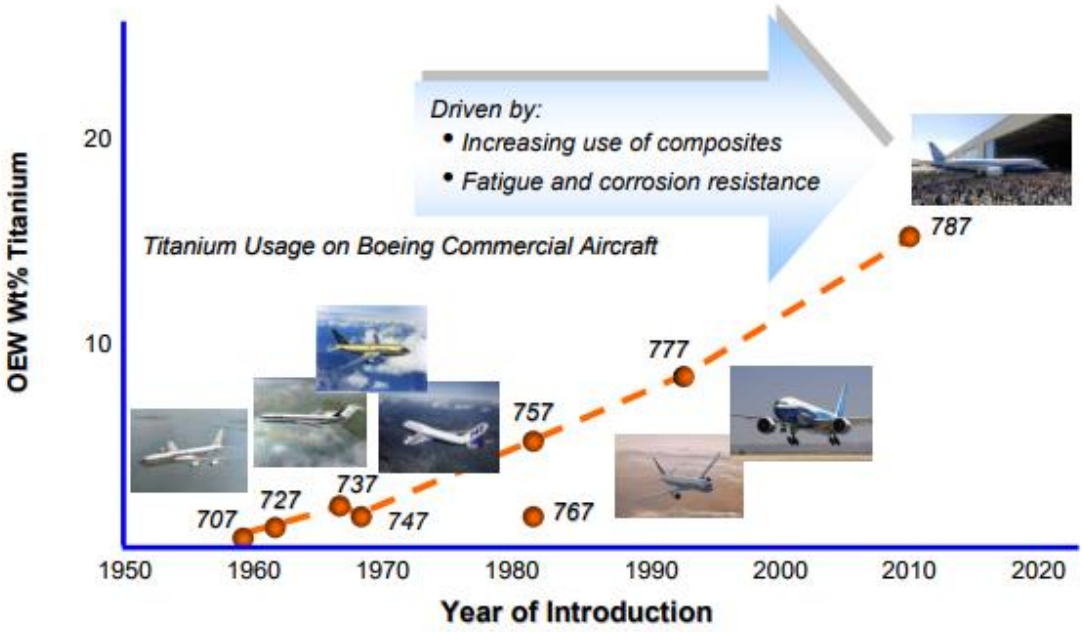

Figure 3. Figure demonstrating increasing use of Ti alloys in Boeing's fleet. Operating empty weight percent of Titanium has steadily increased over time [31].

1.4. Analysis Techniques, Motivation, and Purpose

This thesis investigates the resulting microstructure, mechanical properties, and fatigue behavior after the process parameters were altered on an EBM build of Ti-6Al-4V. A comprehensive literature review on the fatigue properties of EBM fabricated Ti-6Al-4V precedes a discussion of the experimental material characterization and 4-point bend fatigue tests. Design recommendations and best practice methods are also discussed. For fatigue behavior, 4-point bend fatigue testing on an MTS 810 Servo-hydraulic test machine is used. Build geometry (part size), orientation, scan path, and surface finish are compared within the fatigue tests. A finite element analysis (FEA) was performed to obtain the stress concentration factor (SCF) of the 4-point bend test bar geometry. Crack initiation sites and crack growth rates are identified using microscopy techniques. Microstructure analysis is conducted by use of Vickers Hardness microindentation, tensile testing, scanning electron microscopy (SEM), and optical microscopy (OM). Microstructural properties as a function of build height (distance from build plate) and part size are characterized and quantified.

The purpose of this study is to link characteristics of the EBM process to the fatigue behavior and microstructure of end parts in order to obtain a better understanding of how different build designs, build paths, and post-processing affect the mechanical properties of EBM-fabricated Ti-6Al-4V. The 4-point bend tests offer a unique loading perspective that addresses a concern in literature that there is a lack of fatigue data in different loading conditions needed for certification. Although a route to certification will not be directly

proposed, it will serve as a reference for better design strategies of EBM fatigue-critical components and assist in the qualification and certification processes.

2. LITERATURE REVIEW

Titanium is often regarded as “the aerospace metal” because of its wide spread use in the industry. The most popular titanium alloy is Ti-6Al-4V as its mechanical and material properties make it an attractive material for damage-tolerant structural components. Fatigue is one of the most common methods of failure in the aerospace industry and extensive research has been conducted on the fatigue behavior of Ti-6Al-4V. Electron beam melting is an attractive metal AM process for Ti-6Al-4V, but the fatigue properties are not well understood and limits its use. The following sections discuss the fundamentals and microstructure of traditionally manufactured Ti-6Al-4V, the mechanical properties of EBM manufactured Ti-6Al-4V, and important electron beam melting process parameters that affect the microstructure and corresponding fatigue properties.

2.1. Ti-6Al-4V Microstructure

2.1.1. Crystal Structure and Phases

Ti-6Al-4V is a dual phase alloy composed of both the hexagonal close-packed (HCP) α phase and body-centered cubic (BCC) β phase at room temperature. The alloy undergoes an allotropic phase transformation at the β transus temperature, which can vary from 973°C – 1,014°C [34] depending on the amount of α stabilizing and β stabilizing elements (pure titanium’s β transus temperature is 882°C [6]). Al is an α stabilizer, raising the temperature at which the α phase is stable, and V is a β stabilizer, lowering the temperature at which the β phase is stable. Because the BCC β phase is more deformable containing 48 slip systems compared to the HCP α phase’s 12 (HCP metals have very few slip systems and

are often brittle) [35], the mechanical properties, specifically the fatigue crack initiation, are largely dependent on the deformation behavior and texture of the α phase. The HCP crystal structure is inherently anisotropic where its orientation with respect to the load direction has significant effects on its deformability. The elastic modulus of the α phase has been shown to decrease from about 145 GPa to 100 GPa as the angle between the stress and c-axis varies from 0° (perpendicular to basal plane) to 90° (parallel to basal plane) [36]. This anisotropy in the HCP crystal structure results in different mechanical properties in different orientations with respect to the loading axis [37].

2.1.2. Phase Transformations

The cooling rate and alloying element content determine the β → α phase transformation dynamics of titanium alloys. Important features and transformation temperatures are provided in Fig. 4, a pseudo-phase diagram.

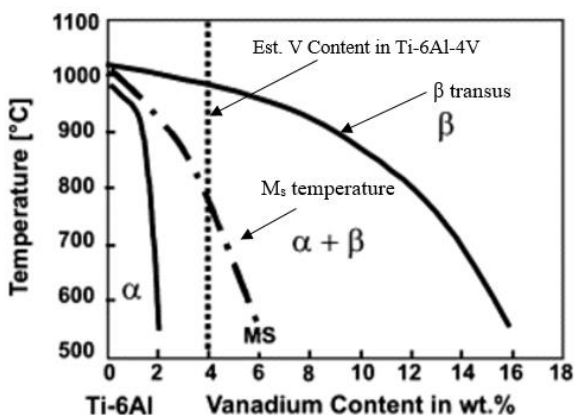

Figure 4. Pseudo-phase diagram of Ti-6Al-4V showing the β transus, α + β phase fields, martensitic start temperature as a function of V content. Figure adapted from [38].

In Ti-6Al-4V, the transformation can occur martensitically if the cooling rate is high enough or by nucleation and growth. The α phase is oriented to the β phase by the Burgers Orientation Relationship [39, 40] such that

$$(0001)_\alpha \parallel (110)_\beta$$

$$11\bar{2}0\alpha \parallel 1\bar{1}1_\beta$$

Thera are 12 distinct α variants that can be inherited from a single parent β grain [41]. A martensitic diffusionless transformation describes the cooperative movement of many atoms in a regimented manner such that the atoms do not move more than one interatomic spacing throughout the entire transformation process [40]. The diffusionless martensitic β → α′ transformation can be observed at cooling rates greater than 20 C°/s and a fully martensitic structure is observed at cooling rates above 410°C [42]. The transformation results in a very hard but brittle microstructure characterized by individual α′ plates. The increased strength is a result of the fine plates and increased dislocation density brought on by the rapid phase transformation. Despite having an HCP structure, α′ is supersaturated in β stabilizing elements, a result of the diffusionless transformation, meaning the α′ metastable phase and β phases have the same chemistry. It is important to note that annealing in the α + β phase field decomposes the martensite structure by precipitating β phase at plate boundaries or internal dislocations or twins and resulting in a Widmanstätten morphology. Following precipitation, growth of the α and β phases is controlled by atomic diffusion where V segregates into the β phase and Al into the α phase. The decomposition process is dependent on annealing time and temperature and full decomposition can occur in an hour at 700°C [43].

Martensitic transformations occur between a range of temperatures, the martensite start temperature (M_s) and martensite finish temperature (M_f). The M_s is the temperature at which the martensitic phase transformation begins provided the cooling rate is high enough and the M_f denotes the temperature at which the transformation is complete. The M_s of Ti-6Al-4V varies, but is estimated to be between 800°C and 830°C [2, 38]. The M_f temperature is reported to be below room temperature for Ti-6Al-4V [44, 45]. Thus, even with rapid quenching, there is an amount of retained β phase as not all β is converted to α′ [45]. Despite the ability to block dislocation motion, ductility is greatly reduced as strain incompatibly develops between the α′/β interfaces leading to brittle faceting and fracture [46].

Slow cooling rates in titanium alloys, like Ti-6Al-4V, bring about a different phase transformation mechanism than the rapid martensitic transformation. Where the martensitic β → α' transformation is diffusionless, at slow cooling rates the transformation is controlled by nucleation and diffusion. The transformation begins as the α phase nucleates along the β grain boundaries creating a continuous layer of the α phase, referred to as GBα [47]. GBα replaces the β grain boundaries and delineates prior β grain boundaries. The growth of the continuous α layer is dependent on the diffusion of V and Al. Thus, increasing the cooling rate lowers the diffusion rate of alloying elements and the GBα layer decreases in thickness [43]. GBα is detrimental to fatigue properties as early crack initiation is observed along the continuous layer [48]. Further cooling results in α plates nucleating and growing into the β grains. A group of α plates, called lamellae, that

all share the same Burger Orientation relationship grow into bulk of the β grain until meeting other colonies with different orientations. Each group is called a colony and the plates are separated by retained β, which is enriched in V but depleted of Al because of diffusion.

2.1.3. Traditionally Manufactured Microstructures

The microstructures of Ti-6Al-4V are largely dependent on thermal history. The lamellar or colony microstructure is obtained by cooling from recrystallization temperatures above the β transus. Also called the "beta annealed" microstructure, the cooling rate determines the microstructural feature size and morphology. At the slowest cooling rates, a fully lamellar microstructure (Fig. 5a.) is observed where there α laths nucleate and grow from GBα or β grain boundaries. At higher cooling rates but less than 20°C/s [42], the Widmanstätten (also called basket weave) morphology is observed and defined by smaller colonies and fewer α laths within each colony compared to the fully lamellar microstructure. As the cooling rate increases, the α lath and colony sizes decrease to a point where those that nucleated at β grains cannot fill the entire grain and new α colonies nucleate and grow normal to existing α plates creating a microstructure with a basket weave like appearance similar to the Ti-Al-Nb alloy shown in Fig. 5b. The α lath and colony size, determined by the cooling rate, affect the mechanical properties and fatigue performance [6].

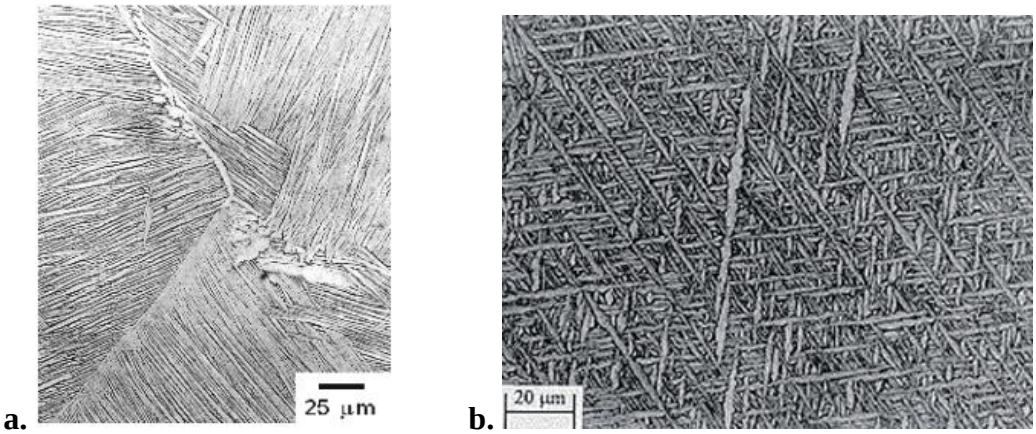

Figure 5. Optical Micrographs of Lamellar Ti-6Al-4V (a.) [49] and Widmanstätten or basket weave Ti-6Al-5Nb (b.) [50]. In both images, the α phase is the lighter grains and the β phase is darker.

At elevated cooling rates, the martensite transformation occurs and a very hard but brittle microstructure marked by high dislocation density and fine plate structure is observed (Fig. 6). Martensite shows high hardness and yield stress, but inferior percent elongation and fatigue damage-tolerance when compared to other Ti-6Al-4V microstructures [51]. However, Ti-6Al-4V microstructures with a mixture of α and α′ were shown to have superior mechanical properties (both ductility and strength) because a single HCP phase exists, reducing the strain incompatibility between the α′ and retained β phases known to cause early cracking while simultaneously reducing the effective slip length [46].

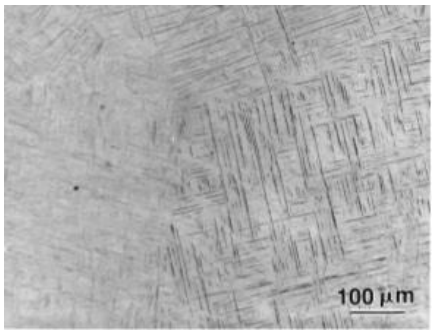

Figure 6. An optical micrograph of a fully martensitic α′ structure obtained by cooling at 525°C/s [42].

Another common microstructure used in industry is the bimodal or duplex microstructure. Characterized by its lamellar matrix broken up by equiaxed α grains (Fig. 7.), the bimodal microstructure differs from the lamellar microstructure in that both deformation and final recrystallization of the microstructure occurs in the α + β phase field (below the β transus temperature). The plastic deformation distorts a lamellar starting microstructure and introduces dislocations that allow for recrystallization and formation of the equiaxed α phase, known as primary α or α_p. In general, the bimodal microstructure has superior tensile

strength [52] and fatigue properties [52, 53] than the lamellar or basket weave morphologies although there is some disagreement in literature because of variation in α lath sizes and α_p grain sizes.

The mechanical properties of the three mentioned microstructures vary by microstructural feature size. The 0.2% proof stress and elongation to failure for lamellar, bimodal, and martensite microstructures with different microstructural feature sizes are provided in Table 1.

Table 1. Mechanical Properties of Conventionally Processed Ti-6Al-4V

Microstructure	Features	$\sigma_{0.2\%}$ (MPa)	ε_F	Reference
Fine Lamellar	α lath size = 0.5 μm	1040	0.20	[5]
Lamellar	α lath size = 1 μm	980	0.25	[5]
Coarse Lamellar	α lath size = 10 μm	935	0.15	[5]
Bimodal	α grain size = 6 μm, 40% α_p	1110	0.55	[5]
Bimodal	α grain size = 25 μm, 40%α_p	1075	0.45	[5]
Martensite	α′ (~100 Volume %)	1007	0.023	[44]

The mechanical properties provided in Table 1 show that the morphology and microstructural feature size, specifically α lath and grain size, affect mechanical properties. A decrease in proof stress and ductility in both the lamellar and bimodal microstructures as grain size decreases is a result of the decrease in effective slip length. The martensite

has the highest proof stress, a result of the fine α′ pates, but lowest ductility. The increased strength is a result of the fine α′ plate size and the decreased ductility can be attributed to a change in fracture behavior [41].

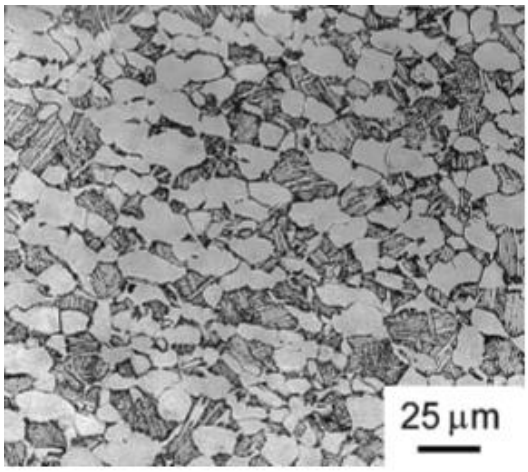

Figure 7. An optical micrograph of the bimodal (duplex) microstructure of Ti-6Al-4V [37].

2.2. Fatigue Mechanisms and Properties of Ti-6Al-4V

Ti-6Al-4V's superior corrosion resistance and specific strength make the alloy an attractive material for use in aerospace structures, which are often under fatigue loading during service. The microstructural features, texture, and thermal processing history determine the fatigue properties. Important microstructural features include prior β grain size, α colony size, α lath size, and α_p grain size (in bimodal microstructures) [5]. Each morphology is better suited for a different application (i.e. crack initiation versus crack propagation resistance). As previously mentioned, the bimodal microstructure typically has a higher fatigue damage-tolerance than the lamellar microstructure [53, 54], although the fatigue

strengths, stress at which a sample can withstand 10^7 cycles, for a collection of bimodal and lamellar morphologies for fully reversed loading are 537.4 +/- 136.1 MPa and 609.3 +/- 102.8 MPa, respectively [55]. Because HCF life is largely dependent on the cycles to initiate a crack, the finer microstructure in the bimodal morphology increases the fatigue crack initiation and small crack growth resistance [56]. The lamellar microstructure provides increased crack path tortuosity, deflection, bifurcation, and crack closure effects decreasing the crack propagation rate [48, 52, 53]. The ideal lath width is 2-5 microns for best crack propagation resistance and toughness in lamellar microstructures [57]. A schematic of the different crack paths for the lamellar microstructure (β annealed) than a bimodal microstructure (α-β annealed) is provided in Fig. 8.

a. 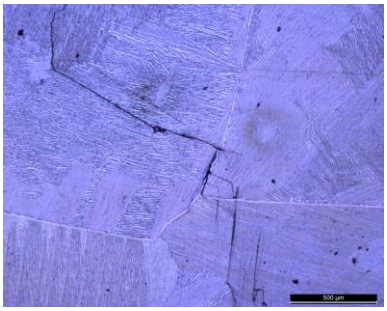

b. 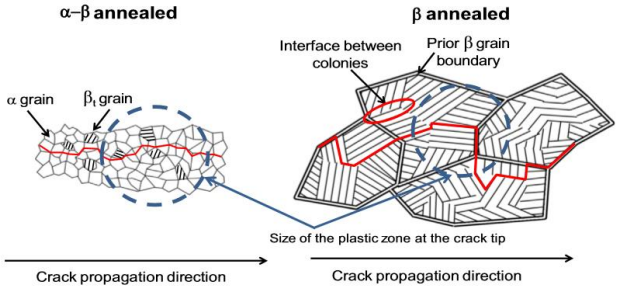

Figure 8. An optical micrograph demonstrating a coarse lamellar microstructure's crack path tortuosity (a) and a schematic of the differing crack paths between α-β annealed and β annealed microstructures (b) [37].

An important distinguishing characteristic between the bimodal and lamellar microstructures with regards to fatigue properties are the crack initiation sites. Cracks initiate via cross colony slip band fracture within an α colony [53] or at α/β phase boundaries [41] lamellar microstructures. In bimodal microstructures, cracks commonly

initiate within the α_p [54, 56] but have been observed initiating within the $\alpha + \beta$ phase regions as well [58].

The texture, or crystallographic anisotropy, of the microstructure has a significant impact on the fatigue life of Ti-6Al-4V as it can enhance fatigue crack initiation if groups of grains are oriented for easy slip within a local stress field [59]. The effects of texture and grain size are shown in Fig 9. Strong texture effects can diminish any positives gained through refinement of α laths [34] as the effectiveness of a high angle boundary to deter crack growth is dependent on the orientation of the neighboring grains. If a single large grain or group of similarly oriented grains are oriented for easy slip, also known as a macrozone [60], cracks will form easily, the local stress concentration will increase, and early failure will occur (Fig 9b.). On the contrary, if many small grains have random orientation (Fig 9c.), the grains will block crack propagation and more effectively tolerate fatigue damage.

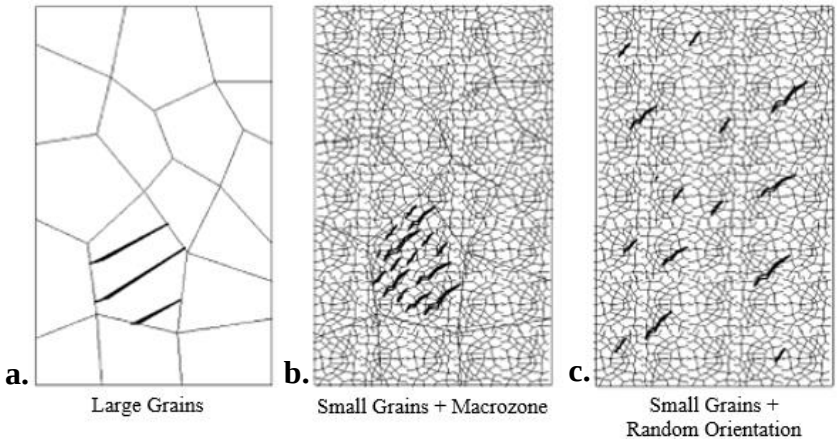

Figure 9a-c. Crack formation and the role of grain boundaries and macrozones [60].

In literature, fatigue cracks have been shown to preferentially initiate on prismatic [56, 61] and basal [56, 61-63] planes because the critical resolved shear stress for basal and prismatic slip are relatively equal. However, the most damaging and earliest of cracks initiate on the basal planes [56].

The origin of a fatal crack forming on the basal plane is thought to require a combination of a high Schmid factor, similar to a classic slip mechanism, and elevated elastic stiffness of the HCP phase when loaded perpendicular to the basal plane which induces a high tensile stress normal to the basal plane [56]. As shown in Figure 10, the HCP crystal is inherently anisotropic. A greater stiffness, *E*, is observed when loading is applied perpendicular to the basal plane than applied parallel.

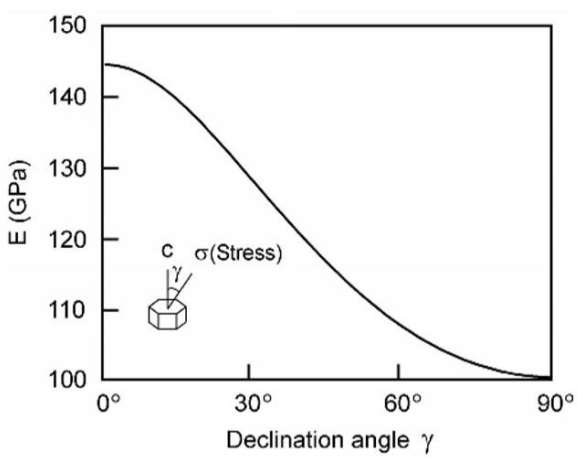

Figure 10. Young Modulus (stiffness) of α Ti as a function of loading angle [6].

EBSD results revealed that fatal fatigue cracks initiate easily when loading is perpendicular to basal planes, the high stiffness orientation [56, 64].

The anisotropy in stiffness is a result of the preferred slip direction in the HCP α phase [65]. HCP crystals have 3 slip planes; prismatic, basal, and pyramidal but only 1 preferred slip direction, the $\langle 11\bar{2}0 \rangle$. When the loading angle, γ, is 90°, the loading direction is parallel to the preferred slip direction and the lowest stiffness is observed. As γ approaches 0°, the loading direction is perpendicular to the loading direction and the maximum *E* is obtained.

2.3. Electron Beam Melting

Electron beam melting is a metal additive manufacturing method which uses a high powered electron beam guided by a Computer Aided Design (CAD) file to selectively melt metal powder into a fully dense part. The process, originally developed by Arcam AB, works similarly to a scanning electron microscope and is capable of fabricating parts with fine features and internal geometries which would be very difficult if not impossible by traditional manufacturing methods like machining, forging, or casting. Some current uses of EBM manufactured parts in industry include dental and medical implants [66-68], aerospace brackets [69, 70], robotics [20], and turbine airfoils [71, 72]. With some post process machining or heat treatments, the mechanical properties of these EBM fabricated parts are sufficient for their current uses. However, a significant portion of the research on EBM additive manufacturing of Ti-6Al-4V is devoted to the fatigue behavior. The following sections will summarize the microstructural evolution, mechanical properties, and fatigue behavior of Ti-6Al-4V fabricated by EBM.

2.3.1. EBM Microstructural Evolution and Mechanical Properties

The electron beam melting thermal history and process map is provided in Figure 11. The center of the high-powered electron beam generates temperatures of up to 2310°C - 2370°C [73], well above Ti-6Al-4V's melt temperature of 1660°C [74]. A rapid solidification ensues at estimated cooling rates above 10^3 – 10^5 K/s [75], sufficient for the diffusionless $\beta \rightarrow \alpha'$ transformation. The solidified part then undergoes an in-situ anneal for the remaining build as the build temperature is maintained at 700°C - 730°C [9, 76] allowing for diffusion controlled martensite decomposition by β precipitation at α′ plate boundaries. Following the build completion, a high purity He purge assists with cooling to room temperature.

The EBM process submits the material to a unique thermal history and resulting microstructure. A typical microstructure of EBM melted Ti-6Al-4V is provided in Fig. 12. For complete melting and good layer-to-layer adhesion, the melt pool must penetrate multiple build layers. This results in epitaxial growth of the β phase where the most recently solidified layer inherits the orientation of the previous layer. Wavy columnar prior β grains, extending multiple build layers (>50 μm) and delineated by α_{GB}, lead to a textured microstructure and anisotropy in the mechanical properties. A mixture of fine colony and Widmanstätten morphologies, a result of α′ decomposition, are observed within the prior β grains [10, 77]. In contrast to the Z planes, equiaxed β grains form on the XY planes (or scanned surfaces) indicating that the prior β grains are rod-like in shape [78].

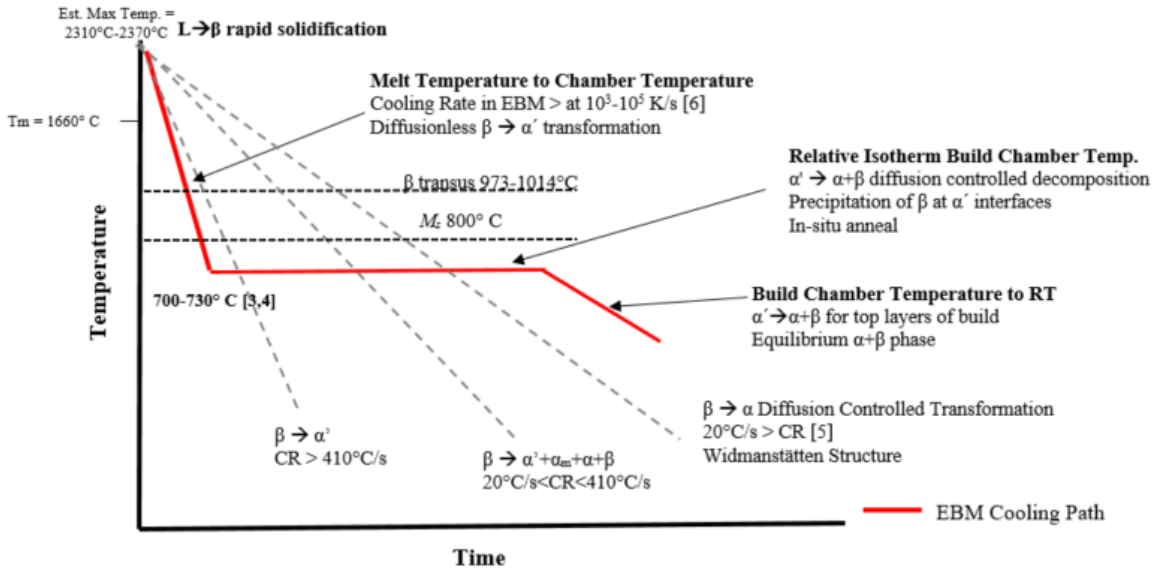

Figure 11. Electron beam melting cooling curve and thermal history of Ti-6Al-4V. Figure adapted from [42] and [79] .

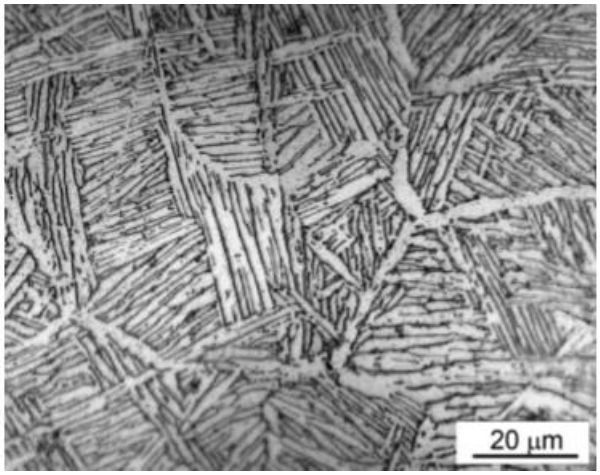

a.

b.

Figure 12. Optical micrographs of EBM manufactured Ti-6Al-4V where (a) is an image of the X-Y plane and (b) is an image of the z/build direction [80].

The initial build layers often show a number of equiaxed prior β grains with random orientation because of the high cooling rate near the stainless steel build plate heat sink [75]. A transition from equiaxed to columnar grains (Fig. 13) then occurs as epitaxial growth ensues along the most favorable orientation for dendritic growth in cubic metals, the ⟨100⟩ [40, 81]. An in-depth review of the tensile strength of AM Ti-6Al-4V [82] and initial review suggests that the horizontally-oriented parts (the build direction perpendicular to the loading direction) have a higher tensile and ultimate strength than vertically oriented samples [80, 83, 84]. However, some studies conclude the opposite [85] and others show no orientation dependence [83, 86]. The surface condition of the test specimen may affect the tensile strength and ductility more than the build orientation, which are not provided in [82].

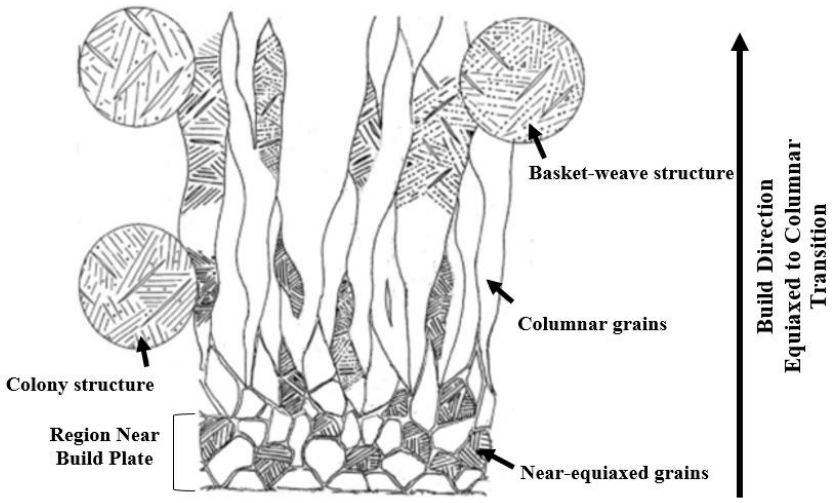

Figure 13. Schematic of the equiaxed to columnar transition and α morphologies observed in the EBM-fabricated Ti-6Al-4V. Figure adapted from reference [10].

2.3.2. Electron Beam Melting Defects

Two common defects found in EBM components are spherical gas pores and irregularly shaped lack-of-fusion (LOF) defects (Fig. 14). The spherical pores, 10 μm - 12 μm in average diameter [87, 88], are distributed throughout the build and thought to be left over from the gas atomization process used to initially manufacture the powder [20, 89]. The LOF defects are irregular shaped voids oriented parallel to the build direction result from incomplete melting of powder due to non-optimized build parameters [90] . Both types of defects have significant effects on the mechanical properties and fatigue life of Ti-6Al-4V parts fabricated by EBM.

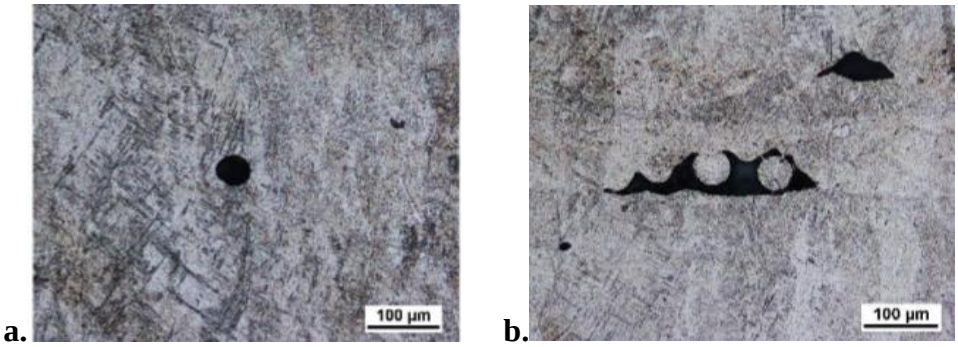

Figure 14. Optical micrographs of gas porosity (a.) and a lack-of-fusion defect (b.) [91] .

Melt balling and layer delamination (Figs. 15a. and 15b.) are process deficiencies associated with EBM additive manufacturing and both lead to complete build failure. Melt balling occurs when insufficient energy density is transmitted to the powder and the surface tension of the liquid metal exceeds the wetting ability of the previously solidified layer. Layer delamination arises when the residual stresses induced by the high-temperature gradients formed during melting exceed the binding strength between the top and

previously solidified layer [92]. Layer delamination cannot be repaired by post-processing and the build must be aborted or the part will be defective. This is in contrast to LOF defects or pores, which are localized to the interior of the part and can be mitigated by post-process heat treatments [20].

a. b.

Figure 15. EBM process deficiencies melt ball formation (a) [20] and layer delamination (b) [93].

2.3.3. Selected EBM Parameters that Effect Microstructure and Mechanical Properties

Literature has shown that the microstructure of EBM fabricated parts is dependent on the process parameters and build geometry. This presents potential problems certifying and using EBM parts in aerospace applications as the same part can have different mechanical properties depending on the process parameters used to build the part. It has been reported that over 100 process parameters could affect the fatigue life [32]. The following sections of this report document and discuss the effects of various process parameters on microstructure and mechanical properties.

2.3.3.1. Powder Chemistry and Recycling

An estimated 95-98% of powder raked onto the build bed is not sintered during the build process [94]. Thus, a powder reclamation system, outlined in Fig. 16, is used to blast the partially sintered powder off the finished build and retrieve the un-sintered powder to be recycled.

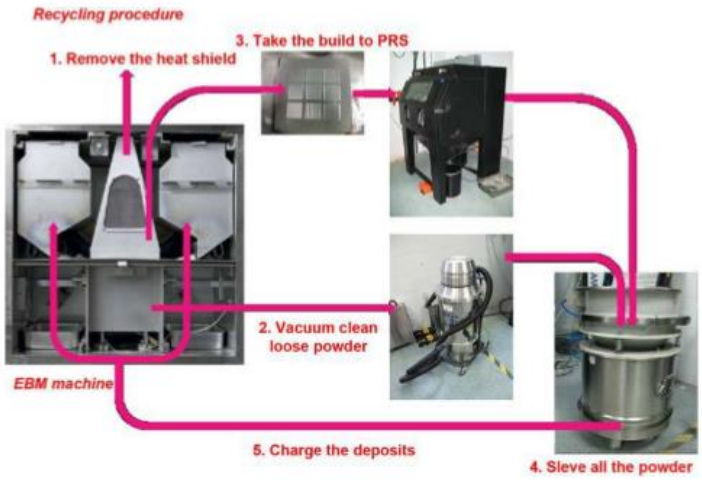

Figure 16. Powder Reclamation system and recycling procedure of powder in EBM [94].

Studies have shown powders become less spherical, pick up other elements, and experience Al evaporation during recycling, but mainly oxygen pickup limits the amount of build cycles the powder can be reused [94-96]. Reuse cycles ranging from 15 builds [94] to 21 builds [96] were acceptable before the oxygen content exceeded the ASTM Standard F2924-14 [97] of 0.20 wt.%. oxygen, the main source of which is thought to be residual humidity in the build chamber [95]. Oxygen content in Ti-6Al-4V has a significant impact on fatigue life as increasing oxygen decreases ductility [98] and accelerates crack

propagation rates [64]. Mixing recycled powder with fresh powder is recommended to avoid the use of powder with out-of-specification oxygen content.

2.3.3.2. Part Thickness

The EBM process melts a 2D area to build a part layer by layer. Increasing the area and thus the part thickness, increases the area to be melted and energy input [99]. The greater energy input decreases the cooling rate and increases the overall average temperatures prolonging the in situ annealing process coarsening the microstructure of thicker parts [88]. As the wall thickness thins to below 1 mm, α′ martensite is observed while parts with walls greater than 5 mm in thickness only show α/β microstructures [77, 100]. The mixed α/α′ microstructure, fine laths, and elevated hardness measurements indicate lower aging temperatures, lower thermal input, and higher cooling rates in thinner sections compared to thicker sections [88].

2.3.3.3. Orientation

Depending on the plane of observation, the microstructure of EBM-fabricated components can display different microstructures, most notably equiaxed or columnar prior β grains. The anisotropic microstructural features can lead to differing yield strength (YS), ultimate tensile strength (UTS), elongation to failure [82], and fatigue strength (particularly in the as-built or raw condition with no post-process machining or heat treatment) [101] depending on the loading direction with respect to the build direction. Vertically oriented parts (built such that the load direction is perpendicular to the load direction) show marginally better YS and UTS compared to horizontally oriented parts (built such that the load direction is perpendicular to the build direction) [84] although the trend is not always

observed. Hrabe et al. [102] indicated that although the YS and UTS did not differ drastically, the percent elongation at failure in vertically oriented parts was 30% lower than horizontally oriented parts. The LOF defects, oriented perpendicular to the build direction, could also reduce strength and ductility [103]. Regardless of orientation, EBM-fabricated Ti-6Al-4V consistently show comparable or better UTS and YS to wrought or conventionally manufactured Ti-6Al-4V [104-106] due to the fine microstructure obtained by the rapid cool and in situ anneal.

2.3.3.4. Distance from Build Plate and Build Plate Location

The geometric setup, specifically the distance from the stainless steel build plate, of the build can also affect the microstructure and corresponding mechanical properties although there is some disagreement in literature on the effects. Microstructural coarsening has been reported with increasing distance from the stainless steel plate [8, 10, 107]. The fine microstructural features near the build plate are thought to be a result of the stainless steel plate acting as a heat sink for the bottom layers. This was observed in build heights as low as 30 mm [10] and as high as 372 mm [107]. As the build progresses, the vacuum and powder insulate the build decreasing the cooling rate and resulting in a coarser microstructure. On the contrary, a finer microstructure has been reported near the top of the build [9, 88, 91]. Because the layers in the bottom of the build are deposited first, they experience a longer time at elevated temperatures resulting in a longer annealing time and grain coarsening ensues [91]. These seemingly contradictory observations reported in literature indicate that other factors, like geometric supports and part size, could influence the effects of build height on microstructure.

The location of the part on the X-Y plane can also impact the mechanical properties. Sochalski-Kolbus et al. hypothesized that the exterior of the build (near the edges of the build plate) would be cooler than the interior because the beam would need to deflect more to reach the exterior parts [108]. However, parts built and tested by Hrabe et al. only showed a slight difference (2% or less) in ultimate tensile strength (UTS) and yield strength (YS) for interior versus exterior parts [90]. Galarraga et al. attributed superior YS, UTS, and elongation in samples built in front-corner compared to centrally-located samples (built in the middle of the build plate) to increased porosity [91]. Since there was little difference in microstructural features between exterior and interior parts, the increased amount of porosity is likely due to other build parameters.

2.3.3.5. Line Offset

Line offset is the distance between two in-fill lines of which the default value is 0.1 mm. At the default settings, there is sufficient overlap of the hatch lines to ensure complete melting. Increasing the line offset value reduces the overlap of the hatch lines trapping powder beneath the surface, increasing the amount of porosity in the finished part. This effect is amplified after the line offset is in excess of 0.18 mm [109]. A defocused beam (high focus offset value) could be used to increase the overlap, but melt pool penetration issues become more prevalent with a defocused beam and the porosity formation mechanism changes from insufficient melt pool overlap to insufficient melt penetration. In a study conducted by Mohammad et al., a line offset of 0.17 - 0.18 mm with a focus offset of 5 mA provides favorable conditions for a fast build without significant pore formation [110].

2.3.3.6. Focus Offset

The beam diameter is most directly controlled by the focus offset, which controls the focal point of the beam from its zero position [111]. The focus offset is designated by the current flowing through the electromagnetic lens, and a higher focus offset value denotes a less focused beam. It affects the beam diameter and relative energy intensity and alters the microstructure in a number of ways. Increasing the focus offset results in a larger beam diameter but decreases the energy density and beam penetration depth, leaving the build susceptible to porosity. A variation in the focus offset of +/- 10 mA changes the beam diameter by 0.05 mm [111], and values above 16 mA were found to increase porosity in the samples [109]. In general, a lower focus offset value will yield denser parts [109, 112], but this trend comes at the cost of longer build times with a smaller beam, as more scans are required to cover a given area.

Focus offset was also found to impact surface roughness [99, 109, 112]. While the authors demonstrated that it is possible to reduce the severity of the surface roughness by modifying the focus offset, even an optimized focus offset cannot eliminate it. For fatigue applications, it may be more beneficial to optimize the focus offset to reduce porosity and machine the part for the best surface finish.

2.3.3.7. Contouring

The line offset value of hatch lines has little influence on surface roughness since they are internal to the structure, but the contouring stage along the edges of the part can have a significant impact on roughness based on the contour spacing, speed, number of spots, spot

time, spot overlap and beam current [113, 114]. Similar to the focus offset, it is possible to optimize the contouring strategy for the reduction of surface roughness, but at the cost of dimensional accuracy for only a minor improvement in roughness [114]. Other factors, such as build time, fabrication cost, and dimensional accuracy, should be considered when altering contouring settings.

2.3.3.8. Beam Scan Speed and Length

Proprietary Arcam algorithms known as the "speed function" control the beam current and scan speed to maintain a constant melt pool size. In general, however, increasing the speed function increases the scan speed assuming that all other variables remain constant [115]. Altering the scan speed has significant effects on the resulting microstructure and density of the part. Decreasing the scan speed increases the overall energy input into the part, yielding greater melt pool penetration, a larger melt pool area, and more opportunities for complete melting and a reduction in porosity [87]. By contrast, increasing the scan speed limits the energy input and refines both the α-lath thickness and prior β grain size [78]. Although finer microstructures are observed, it is widely reported in the literature that increasing the scan speed results in a smaller melt pool, less overlap, and increases porosity [78, 87, 116].

A number of authors have reported that altering the electron beam scan length can change the resulting microstructure and mechanical properties [90, 117, 118]. To maintain a constant melt pool, Arcam employs a number of build algorithms that control the electron beam parameters. One such algorithm alters the beam current as a function of scan length.

Although two parts may have the same final geometries, altering the scan lengths during the build changes the beam current used to melt each individual layer. Altering the scan length was reported to vary the yield strength, ultimate tensile strength, and density [118]. In general, the beam current increases with scan length, but a maximum current limit is set by the Arcam machine. Large scan lengths lead to insufficient energy input, poor melting, and increased number of defects [90, 117]. Although increasing the scan length was observed to refine the microstructure [118], scan lengths less than 100 mm are recommended for sufficient melting and avoidance of increased interlayer defects [117].

2.3.3.9. Line Energy and Process Maps

Process Maps identify a range of values that process parameters can be to produce sound parts. They show parameter combinations of beam power or current and scan speed classifying parts as ‘dense’, ‘porous’, or ‘swell’ and provide guidelines on how the EBM process should be set to obtain quality parts. Authors report the process maps as volume energy (J/mm^3) [119, 120], line energy (J/m) [121], or beam current (m/A) [89, 122] as a function of scan speed. An in depth analysis is provided by the respective authors, but in general the results show that the scan speed and energy input must be balanced for successful builds and quality parts. Insufficient energy input by either too low of beam current, power, or too rapid scan speed leads to porosity issues. However, greater energy input than what is needed not only can lead to part swell but also affect the mechanical strength and chemistry of the final build [120].

2.4. Fatigue Behavior of EBM Fabricated Ti-6Al-4V

Although EBM fabricated Ti-6Al-4V meets ASTM standards for wrought and biomedical applications (ASTM F136 [123] & ASTM 348 [124]) for tensile properties, the fatigue strength often falls short. To realize the potential of EBM fabrication and build fatigue-critical components, the fatigue behavior must be well understood. Process conditions, specifically the build orientation [83, 84, 86, 102, 125-127], and post-process heat treatments [8, 76, 106, 122, 127-130] and machining [84, 129-131] have been shown to influence the fatigue behavior of Ti-6Al-4V parts fabricated by EBM. To study the fatigue behavior of EBM-fabricated components, uniaxial fatigue test data was compiled from numerous sources in open literature and then observations and conclusions were made based on trends spanning multiple reports. S-N curves, plots of the stress versus the number of cycles to failure, and runout strengths are associated with high-cycle fatigue (HCF) and are reported and discussed in this literature review because they are indicative of the useful fatigue life, as opposed to crack-growth rates, which are useful for establishing inspection and service intervals [34]. Fatigue data of four different material conditions was collected and compared including parts with no post-processing (as-built/as-built condition) to parts that are machined and hot-isostatic-pressed (HIP). The four different material conditions evaluated in this comprehensive literature review are shown schematically in Fig 17.

The first material condition is the “as-built/as-built” condition representing parts that received no machining nor post process HIP. HIP is a manufacturing post-process that uses an inert gas at elevated temperatures and pressures to

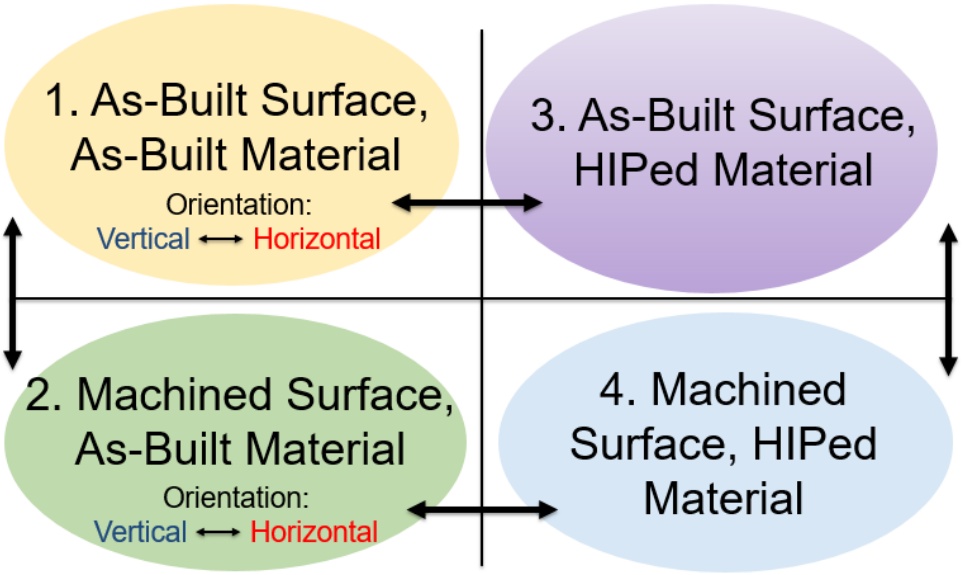

Figure 17. Material conditions considered in the fatigue literature review. The black arrows represent a comparison made between two material conditions.

effectively eliminate porosity [132, 133]. It is important to note that annealed or stress-relieved parts that did not undergo a HIP process are considered “as-built” material for the S-N curve data analysis because stress relief and annealing heat treatments have no effect on porosity (note that stress relieved and annealed parts have similar fatigue lives to the as-built material [76, 90]). This isolates the effects of surface roughness and porosity-closure by HIP on fatigue life. In general, EBM provides an in-situ annealing process that is effective at removing any significant residual stresses. Residual stresses in as-built parts are estimated to be only 5 - 10% UTS [98].

The second material condition is the “as-built material with machined surface”. These specimens have been machined following the EBM process but did not undergo any HIP treatments. Test specimens that were polished following machining are included in this material condition as are heat treated. The build orientations in the as-built/as-built and as-built/machined material conditions are also compared and discussed.

The third category includes specimens that were HIPed but were not machined. The HIP treatments utilized in various studies are outlined in Table 7. of the appendix and all included HIP treatments conducted were below the β-transus temperature. The last material condition represents specimens that were both machined and HIPed. The build orientation of the HIPed specimens in these final two categories is not considered due to the insufficient data available in literature. The orientation, heat treatments, surface conditions, and Arcam machine model for each test are documented in Table 7 of the appendix. Each

set of the normalized data has been assigned a unique marker and trend line based on surface and material condition, also described in Table 7 of the appendix.

Fatigue data for materials in each condition was collected from different sources in the open literature and compared. Thus, the test conditions in each study were not consistent. In order to directly compare fatigue data from various sources, a concept of effective maximum applied stress (σ_{eff}) introduced by Li et al. [32] has been used to normalize the data. Equation 1 describes σ_{eff} as a function of the maximum applied stress (σ_{max}) and R, the ratio between the minimum and the maximum stresses experienced during a cycle.

$$\boldsymbol{\sigma_{eff} = \sigma_{max}\left(\frac{1-R}{2}\right)^{0.28}} \qquad (1)$$

Following normalization using Equation 1, the data was plotted against the original cycles to failure value reported by the authors.

The data collected from literature spans 12 different studies with different testing conditions, including R ratio. Using the σ_{eff} model attempts to normalize the data with respect to R ratio. Normalizing the stress levels is critical because the R ratio can affect fatigue life. At high stress ratios above 0.7, a transition from traditional fatigue-crack-growth to ductile void nucleation and growth fracture is observed in Ti-6Al-4V [134]. The R ratios considered in this review are 0.1, 0.5, -0.2, and -1.

While the σ_{eff} model normalizes the data based off R ratios, the model however, does not consider the frequency of the tests. At low R ratios, increasing load frequency can improve

fatigue life [134]. Fatigue-fracture probability [135], crack initiation [136, 137] and crack propagation [138] have been shown to decrease with increasing load frequencies in commercially pure titanium. Possible reasons for this increased fatigue life at elevated frequencies include less plastic deformation or plastic strain accumulated per cycle [137] and fewer active slip systems in the body-centered-cubic β phase at high frequencies [134]. The increase in fatigue life was observed over 2-3 orders of magnitude differences of frequency, and the majority of data in this review is limited to a relatively narrow frequency range of 20-120 Hz, thus, frequency is not considered to be a significant factor.

The terminology used to describe material conditions, orientations, and sample preparations is subject to variation across the literature, but will be interpreted within this literature review as follows. With regards to build orientation, 'horizontal' parts were built such that the applied load direction is perpendicular to the original EBM build direction and will be represented by red markers and trend lines on the SN curves when appropriate. The 'vertical' parts were built such that the load direction was parallel to the build direction and represented by blue markers and trend lines. Figure 18 provides a schematic of the different build orientations compared in this literature review.

With the material conditions defined, σ_{eff} concept clarified, and build orientations distinguished, it is possible to analyze the fatigue data collected from open literature. The uniaxial fatigue data is presented in order of increasing post-processing methods common to EBM-manufactured Ti-6Al-4V parts, progressing from the most basic parts in the as-

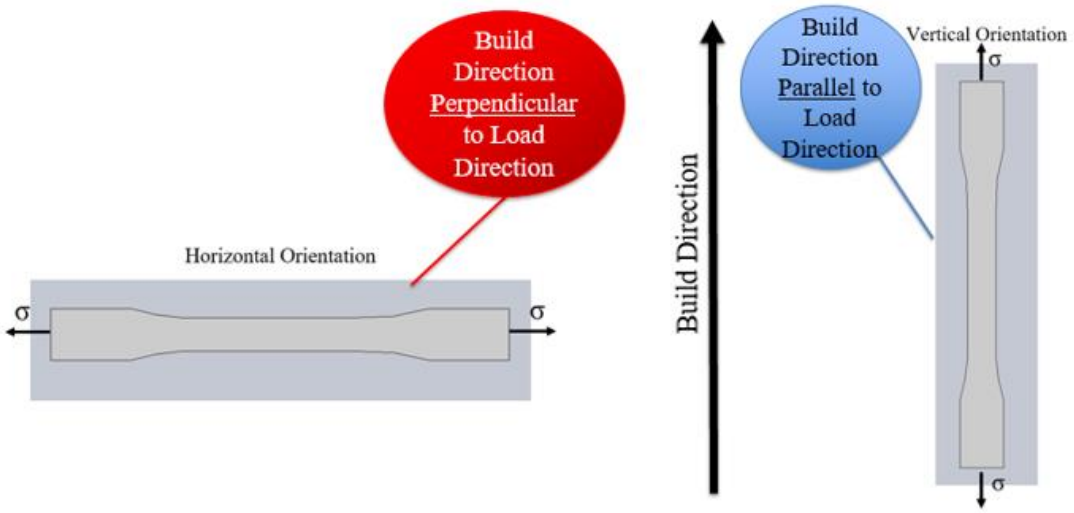

Figure 18. Schematic demonstrating different EBM build orientations in axial fatigue tests.

built/as-built condition to parts that received post-process machining and hot-isostatic-pressing.

2.4.1. Orientation Effects – As-Built Surface with As-Built Material

Build orientation effects on parts in the as-built/as-built condition can be observed in Fig. 19. Because the test parts fatigue and mechanical properties can vary from build to build, the orientation variable must be isolated.

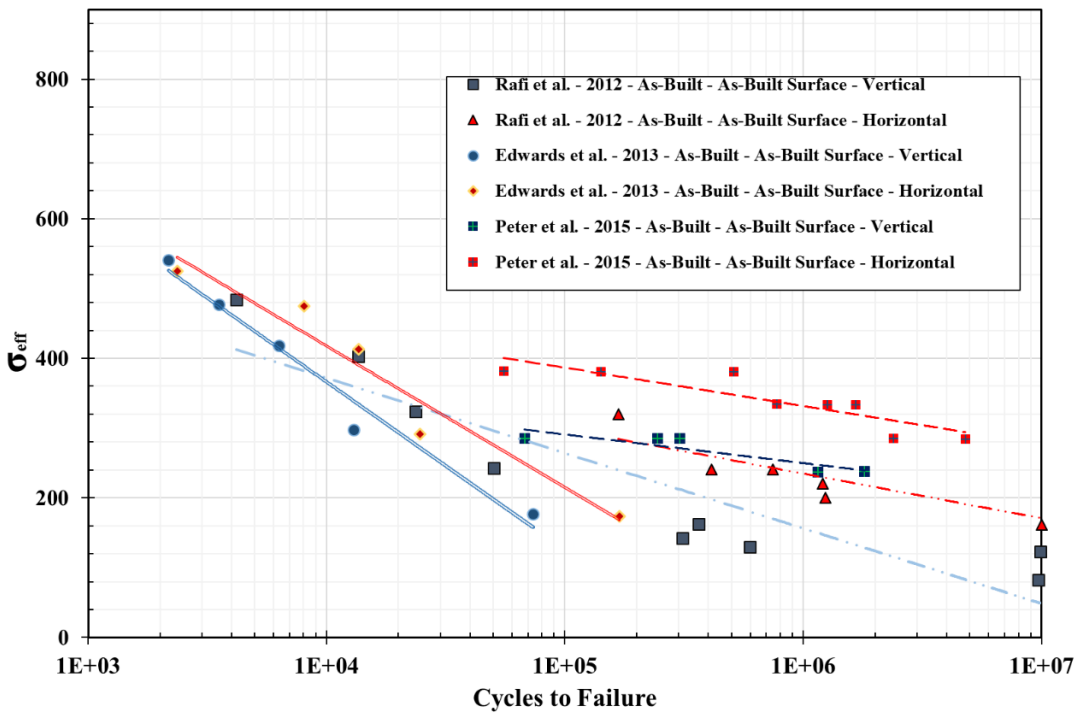

Figure 19. SN chart comparing build orientation of test bars with as-built surfaces and as-built material conditions. Red markers and trend lines represent horizontally oriented parts and blue markers and trend lines represent vertically oriented parts.

In Fig. 19, test parts from same the study are represented by like-lines and markers only differing in red (horizontal) or blue (vertical) base colors. Observing Fig. 19, it is clear that the horizontally orientated tests denoted by red markers and lines have superior fatigue life than their vertically oriented counterparts (blue trend lines and markers).

In the as-built/as-built condition, the horizontally oriented parts have superior fatigue life as a result of rough surface and lack-of-fusion defects inherited from the EBM process itself. Because EBM parts are built layer-by-layer, surface notches with sharp radii are created by melt pool overflow. In vertically oriented parts, the notches (Fig. 20) are oriented perpendicular to the loading direction in axial fatigue tests, acting as stress concentrators and leading to early crack initiation and failure.

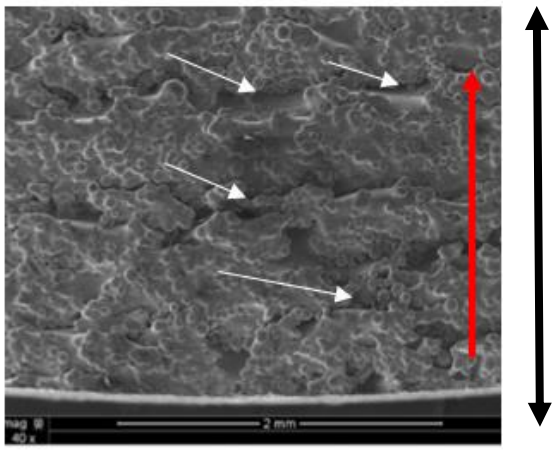

Figure 20. SEM micrograph of an EBM as-built surface. The red arrow indicates the build direction, white arrows the surface notches, and black arrow indicates loading direction in an axial fatigue test. Figure adapted from [139].

In addition to the early crack initiation sites on the surface, the interior lack-of-fusion defects could contribute to the fatigue strength orientation dependence. In vertically oriented parts, the length of the lack-of-fusion defects runs parallel to the load direction decreasing the load-bearing area and increasing the local stress [103]. In horizontally oriented parts, the long dimension of the lack-of-fusion defects is oriented parallel to the loading direction in an axial fatigue test. Therefore, the load-bearing area is not reduced as significantly, as indicated by Fig. 21.

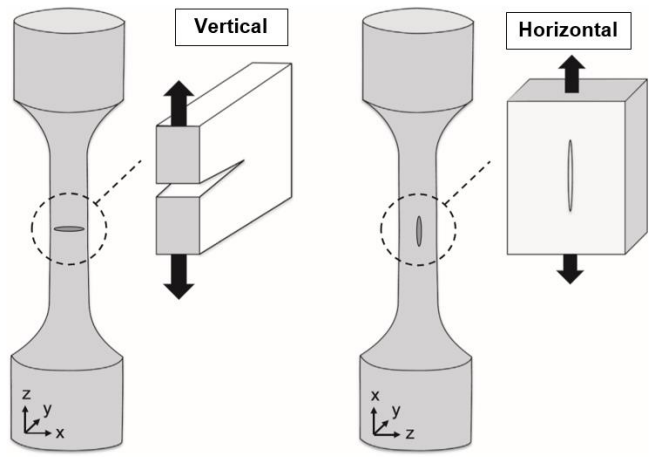

Figure 21. Orientation of LOF defects in vertical and horizontal specimen with respect to different types of loading. 'Z' denotes the build direction. Figure adapted from [29].

2.4.2. Orientation Effects – Machined Surface with As-Built Material

The rough surface finish contributes to the orientation-dependent fatigue behavior in as-built/as-built EBM parts. However, parts are often machined when possible to eliminate the rough surface finish. This section presents and discusses the fatigue behavior of as-built/machined parts in different build orientations. As with the as-built/as-built condition,

one must compare like-builds denoted by similar markers and trend lines. Although slight differences may appear in specific studies, the orientation dependence on fatigue resistance of the as-built material is not as apparent after machining (Fig 22). The red lines do not consistently have higher fatigue life, compared to the blue, as previously observed in the as-built/as-built condition.

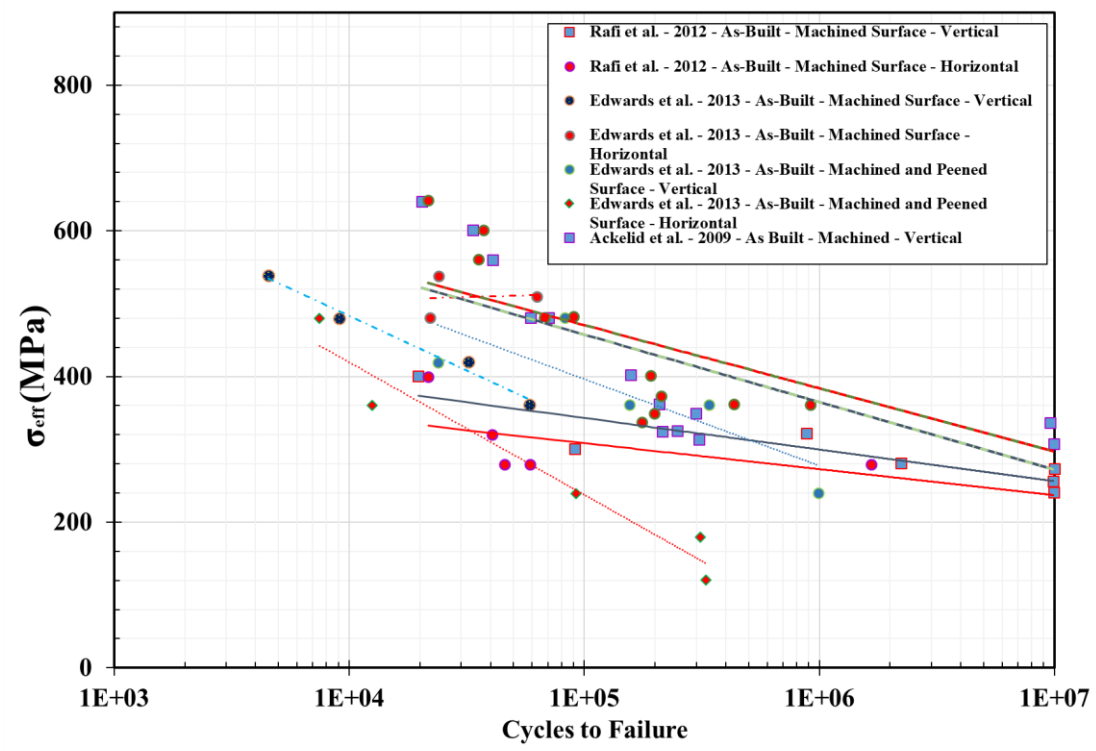

Figure 22. Fatigue behavior of as-built material/machined surface.

There are a number of possible reasons why no clear orientation dependence occurs after EBM samples are machined; machining depth of cut and process optimization. If machining does not sufficiently remove enough material or exposes near sub-surface pores, the remaining defects can still affect fatigue life [85]. It is estimated that 650 μm of the surface material must be removed to completely eliminate the surface roughness effects

[105]. In addition, if melting parameters are optimized, fewer lack-of-fusion defects will be observed in the bulk of the part reducing the gap between horizontally and vertically oriented parts.

2.4.3. Machining Effects - Machined Surface with As-Built Material

The fatigue life of materials is generally known to be dependent on surface quality [140, 141]. Although machining can cause near-surface microstructural damage [142], smooth surfaces produced from fine finishing passes and polishing to increase fatigue life in comparison to rough machining [140]. Because an estimated 85%-99% of the fatigue life in the high cycle regime is consumed during the nucleation and small growth of a crack [34, 143], the rough surface of as-built EBM parts (Fig. 23) increases the local stress concentration and leads to early fatigue failure by providing an early crack initiation site.

a. 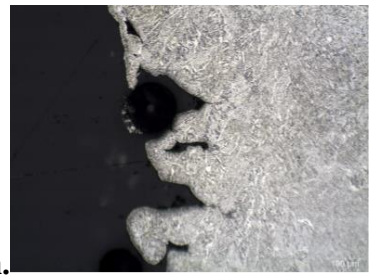 **b.** 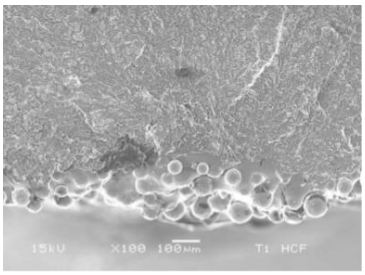

Figure 23. Optical (a.) and SEM (b.) micrographs showing EBM surface roughness [144].

It is thought that the elimination of the rough surface by machining will increase the fatigue life of EBM–fabricated parts. The machined EBM parts generally show a greater fatigue life than the parts with the as-built surfaces, but have inferior fatigue life to the conventionally manufactured Ti-6Al-V (eg. Fig. 24). The lower fatigue life of the

machined EBM parts in comparison to the conventional materials is most likely attributed to the porosity and voids. Inspection of Fig. 24 indicates that machining EBM-manufactured Ti-6Al-4V increases the fatigue life primarily due to a reduction in surface roughness.

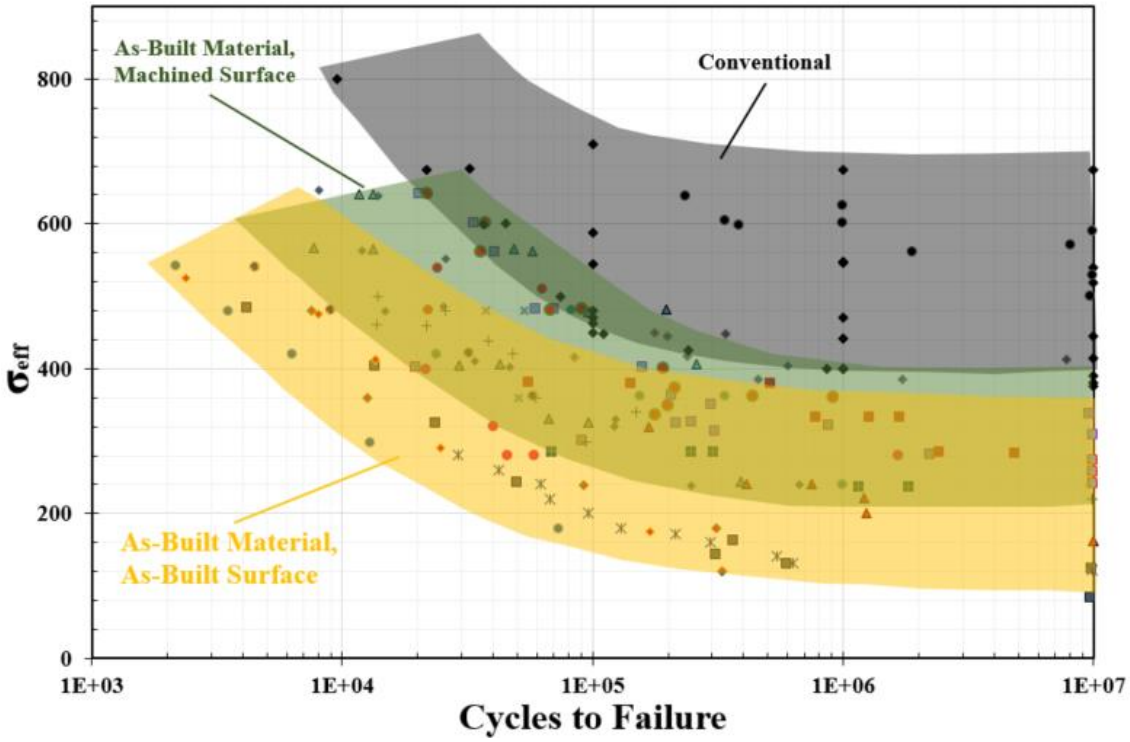

Figure 24. SN curve demonstrating machining effects on fatigue behavior.

The notch-like defects on the rough surface of an as-built specimen provide crack-initiation sites [85, 131, 139, 144, 145]. In contrast, crack-initiation sites following machining (with as-built material) are generally near sub-surface pores [76, 85, 129]. The near sub-surface pores and defects are common crack-initiation sites in un-notched fatigue samples [146]. In addition to eliminating notches for early crack initiation, machining can also increase

the fatigue strength of the machined part by inducing compressive residual stresses at the surface [58].

Figure 24 indicates that there is a clear benefit in machining fatigue critical parts. However, a primary benefit of AM in general is the high degree of geometric design freedom and the ability to build internal features where machining is not possible. A potential process for reducing surface-level defects and porosity on complex geometries is chemical etching. Chemical etching improved the yield strength of Ti-6Al-4V manufactured by EBM 4.7% to 1,018.3 MPa compared to machined samples of 970.6 MPa [105] and improve the fatigue life of porous Ti-6Al-4V structures manufactured by selective laser melting [147]. Chemical etching is believed to increase strength because the etchant blunts surface cracks and defects in addition to removing bulk material. By contrast, machining only removes bulk material and could leave sharp cracks or defects or damage the microstructure on the surface of the machined part.

2.4.4. HIP Effects

Hot isostatic pressing (HIP) is a process that uses high temperature and pressure of an inert gas to effectively close porosity [132]. The fatigue life of HIPed components is compared to those with as-built material in Fig. 25, both conditions having as-built surfaces. By comparing the HIPed data to the as-built data, it is clear the HIP process does not universally improve the fatigue life of EBM Ti-6Al-4V provided the parts have as-built surfaces. Similar observations were made by Kahlin et al. [130, 148]. Although HIP is very effective at closing porosity, it does not eliminate the rough surface crack-initiation

sites in both the as-built and HIPed material conditions. In addition, the HIP process has been shown to coarsen the microstructure nearly doubling the α lath size and more than doubling the β phase content [76] and can lower the UTS and YS [8, 128]. The combination of the microstructural coarsening resulting from HIP and the rough surface inherited from the EBM process may obscure any benefit gained by closing the porosity with regards to the fatigue life.

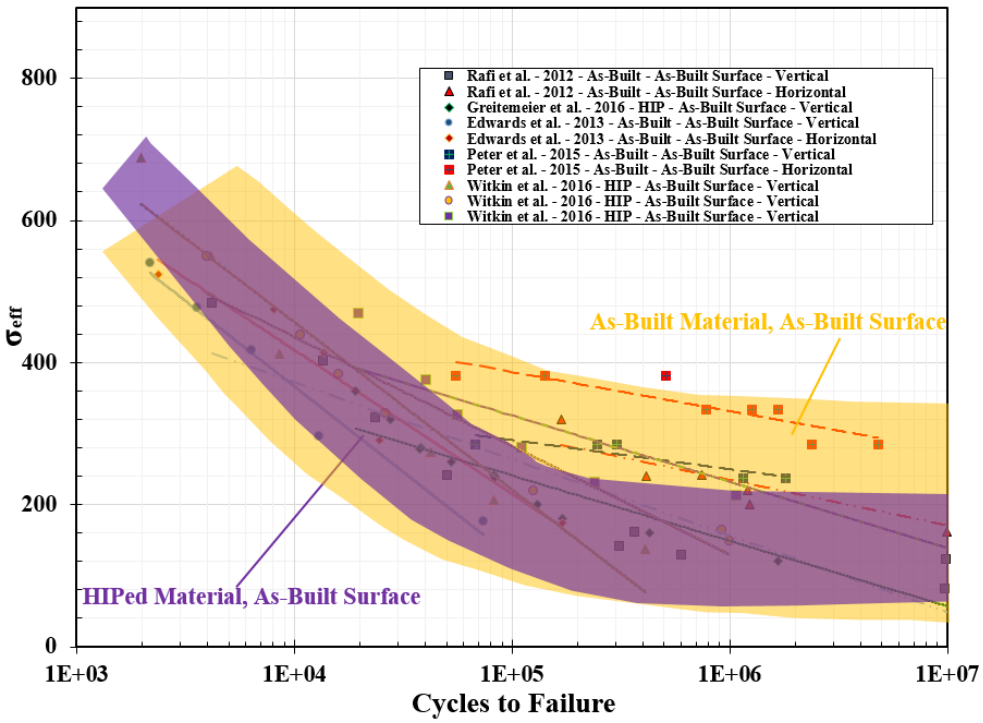

Figure 25. SN curve demonstrating fatigue behavior of HIPed and as-built parts with as-fabricated surfaces.

Although the average fatigue life appears to be lower (the purple area lying within the yellow), it is evident that HIP reduces the scatter in the fatigue data. Scatter in the as-built/as-built components can appear if the porosity defect size is larger or more detrimental

than the surface roughness changing the crack initiation site from surface to internal. HIP ensures that the pores are effectively closed and that the fatigue crack will initiate only from surface roughness effects. The reduced scatter and more predictable fatigue behavior allows for less conservative factors of safety while designing components with very complex geometries where machining or chemical etching may not be possible.

When HIPed samples are also machined, the combination is very effective at improving the fatigue life, as indicated in Fig. 26, giving fatigue strengths at levels comparable to superior to traditionally manufactured Ti-6Al-4V. The EBM Ti-6Al-4V parts that are HIPed and machined often have better fatigue performance than the conventionally-manufactured Ti-6Al-4V. A possible reason for this increase in strength is the EBM parts, despite the HIP process, could have a finer grain structure than the reference material because of the rapid cooling rate associated with the EBM process.

Following the HIP and machining post-processes, the fatigue-crack-initiation site for a machined part has been reported to shift from sub-surface defects to an interior sites [76] which could include microstructural heterogeneities like α/β phase boundaries oriented for slip transfer [58, 129] or cross colony slip-band fracture [76] similar to the traditionally-manufactured lamellar Ti-6Al-4V.

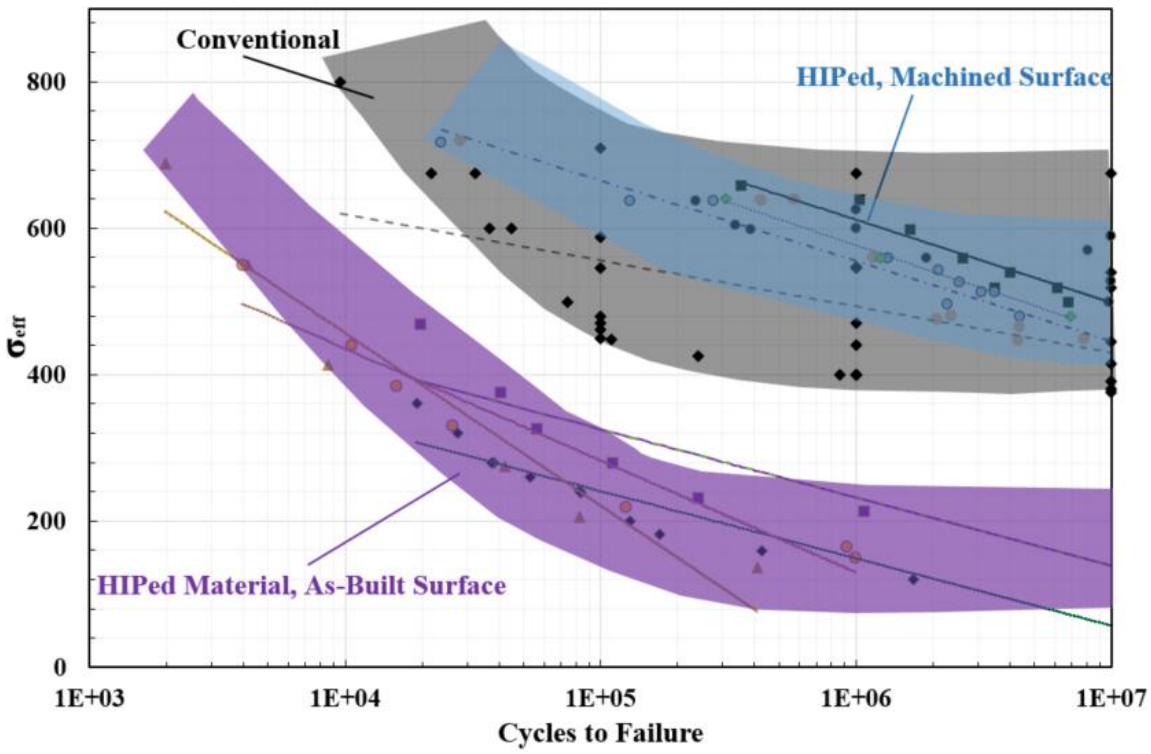

Figure 26. Fatigue Behavior of HIPed components with as-built and machined surfaces.

There is currently insufficient data in the open literature to determine if build orientation still affects the fatigue life following HIP. Ackelid et al. showed no orientation dependence of HIPed and machined components [83] but machining effectively eliminates build-orientation effects, as shown previously. Arcam recommends HIP parameters of 920°C and 100 MPa for 2 hours for Ti-6Al-4V, which is below the β transus temperature of Ti-6Al-4V (973°C - 1,014°C [34]). No β recrystallization would occur during heat treatment below the β transus so the mechanical anisotropy could still exist at after HIP. Therefore, it is possible the fatigue life of HIPed parts with as-built surfaces and machined surfaces may be dependent on build orientation provided that the parts are HIPed according to Arcam's recommendations.

2.4.5. EBM Fatigue Properties – Summary

It is clear that the combination of HIP and machining is superior to all other EBM-manufactured parts as well as the conventional reference material. Although the as-built materials with a machined surface approach the fatigue resistance of the reference material, internal porosity limits performance. Both material conditions with rough surfaces have comparable fatigue resistances, which are much lower than the machined and conventional materials. Figure 28 also shows that there is less scatter in the data for HIPed parts, both machined and with as-built surfaces. Yadollahi and Shamsaei concluded that the scatter in the HCF data of AM parts can be attributed to the presence of voids as the HCF life is affected by the void shape, location, and size [28]. Therefore, the scatter in the fatigue data of the HIPed material is reduced because of the porosity closure and elimination of voids, a result of the HIP process.

Comparison of the available fatigue data in Fig. 27 indicates that the dominant factors in determining the fatigue behavior of EBM components (in order of most detrimental) are: 1. Surface roughness, 2. Internal defects and porosity, and 3. Microstructure. The most significant increase in the fatigue-damage tolerance is observed when the surface roughness and internal defects are both eliminated, followed by eliminating the surface roughness alone.

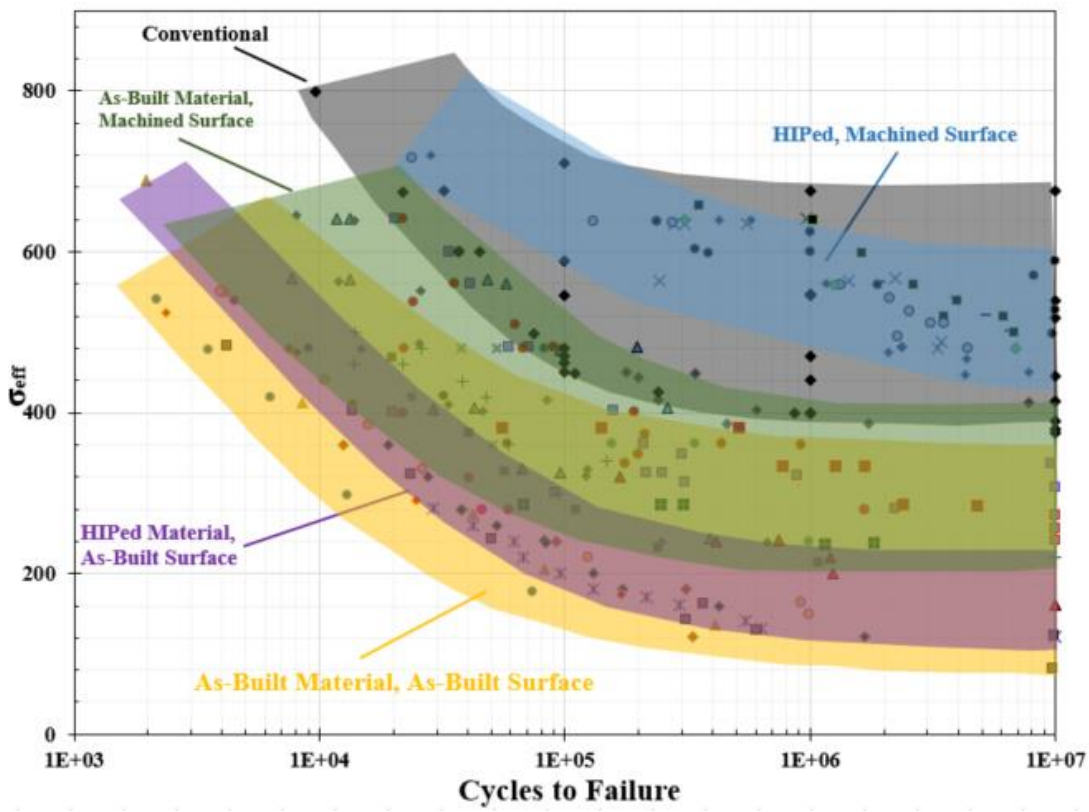

Figure 27. Compiled fatigue data of EBM fabricated Ti-6Al-4V in various states of post-processing including machining and HIP.

2.4.6. Fatigue Endurance Limits

The endurance limit, also known as the fatigue strength or fatigue limit, is defined as the stress below which failure does not occur [25]. Because conventional Ti-6Al-4V does not have a distinct endurance limit [149, 150], the endurance limit for Ti-6Al-4V in this review is reported as the stress level that will survive 10^7 cycles or more. The corresponding endurance limits of the EBM-manufactured Ti-6Al-4V in each of the conditions discussed previously are shown in Fig. 28. Note that the amount of the endurance run-out data is limited as there are only 1 to 5 reported endurance limit values for each of the EBM for material conditions considered.

The fatigue-endurance limit generally increases as the number of post processing steps increase for EBM parts as indicated in Fig 28. Heat-treated samples generally have a -lower endurance limit than their same-surface condition counterparts. Therefore, annealing or stress-relief heat treatments of the EBM fatigue-limited parts should be avoided because the in-situ anneal eliminates residual stresses, and post-process heat treatments only serve to coarsen the microstructure.

The endurance limit for the HIPed and as-built specimen is also lower than the as-built material condition with an as-built surface. Despite the lower endurance limit, the HIP process allows for better design by effectively eliminating porosity and homogenizing the microstructure.

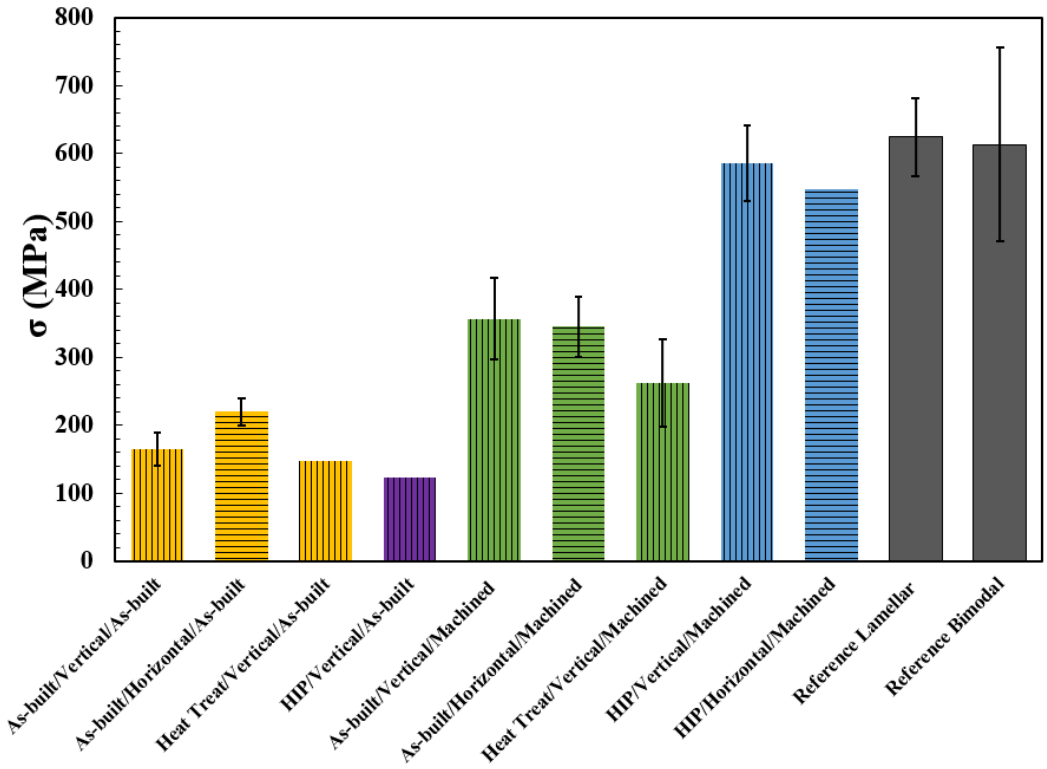

Figure 28. Endurance limits (cycles > 10^7) of material in various orientations and post-process conditions. Error bars on EBM categories represent a range of endurance limits found in literature if available. Error bars on the reference categories represent standard deviations of literature values. All tests used R ratio = 0.1.

Machining improves the fatigue-endurance limit of vertically oriented parts by nearly 150% with an increase in the average endurance limit from 165 MPa to 400 MPa. A significant increase, endurance limits increase nearly 60% from an average of 220 MPa to 345 MPa, is observed when horizontally-oriented parts are machined, but it is not as drastic as when the vertically-oriented parts are machined post-EBM. Following machining, the vertically-oriented parts have a higher average endurance limit, compared to the heat treated and horizontally oriented parts, but only 65% of the endurance limit of the conventionally-manufactured Ti-6Al-4V. Heat treated and horizontally machined samples have roughly 42% and 55% of the endurance limit of the conventionally-manufactured Ti-6Al-4V, respectively.

The HIPed and machined parts have comparable fatigue-endurance limits to the conventional reference material, regardless of orientation. A significant difference in the fatigue-endurance limit of the HIP/Vertical/As-Built parts, compared to HIP/Vertical/Machined parts is of particular interest. By machining the HIPed specimen, an increase in the average endurance limit of 370% is observed. Although the endurance-limit values were reported by different authors ([129] for HIP/Vertical/As-Built, [76, 83, 90, 129, 151] for Vertical/HIP/Machined), and various machines from different years, the HIP processes were similar. Adding a HIP cycle to a machined and vertically-oriented specimen increases the average fatigue endurance limit by 46% when compared to a vertically-oriented machined specimen.

2.5. Comparison to Other Common Aerospace Alloys

A strong correlation exists between the ultimate tensile strength of a material and the fatigue behavior, where the endurance limit increases linearly with UTS and is often approximately half the ultimate tensile strength for most metallic materials [146]. Figure 29 plots the endurance limit versus the UTS of EBM materials in comparison to other common aerospace alloys. The reference data was provided by Hemphill et al. [152] unless otherwise noted. The reference alloys follow a relatively-linear trend of increasing endurance limit with increasing ultimate tensile strength.

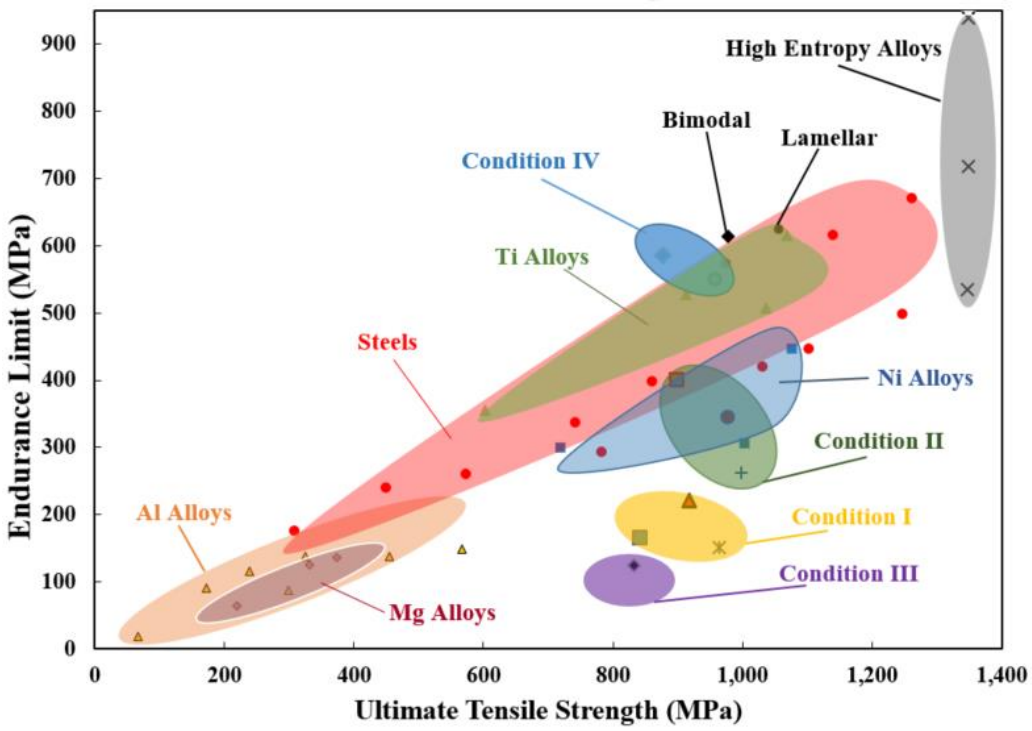

Figure 29. Endurance limits as a function of ultimate tensile strength for various alloys and EBM material conditions. Figure adapted from [152].

The surface and test conditions for the reference data in Fig. 29 are unspecified. Hence, a direct comparison to an un-machined EBM test specimen is unfair. The figure is provided to show that the endurance limit of the Ti-6Al-4V manufactured by EBM can be heavily influenced by extrinsic factors, such as the porosity and surface roughness, which are inherent to the EBM process. The as-built/HIPed and the as-built/as-built parts have a high ultimate tensile strength but the endurance limit is comparable to Al and Mg alloys. In contrast, the machined/as-built parts are comparable to Ni alloys and steels and approach the linear trend region of traditional alloys. The machined and HIPed parts are comparable to reference Ti alloys and within the linear trend region. Overall, the UTS of EBM-manufactured parts remains relatively constant regardless of post processing, but the fatigue endurance limit increases with machining and HIP.

The ratio of the endurance limit to the ultimate tensile strength, known as the fatigue ratio, normalizes the fatigue strength to the characteristic strength of the material allowing for more accurate cross-comparison of the fatigue behavior of different materials. Figure 30 is derived from Fig. 29 and shows the plot of the fatigue ratio versus the ultimate tensile strengths of the EBM manufactured parts and reference aerospace alloys.

The as-built/HIPed and as-built/as-built material have lower fatigue ratios than Al and Mg alloys despite having a greater ultimate tensile strength. In the raw condition, post-HIP alone, or post-machining alone, the Ti-6Al-4V manufactured by EBM underperforms

compared to reference material capabilities. However, in the machined and HIPed condition, the material can exceed the fatigue performance of reference Ti alloys and steels.

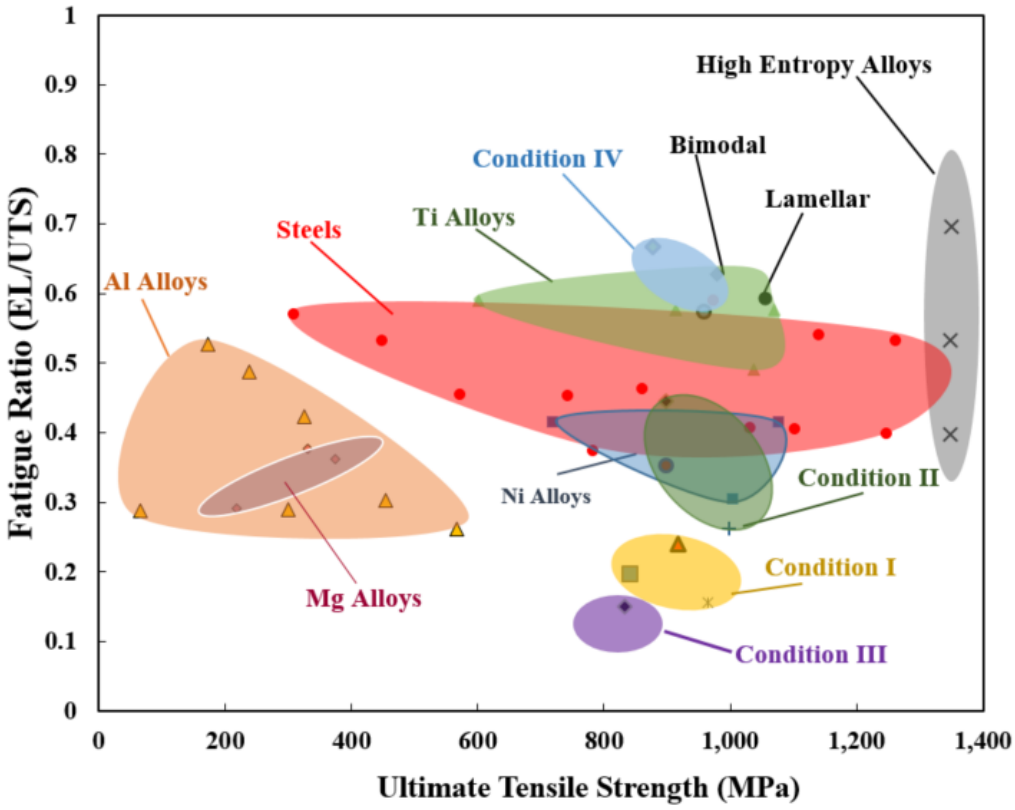

Figure 30. Plot of the fatigue ratio as function of ultimate tensile strengths of EBM manufactured parts and traditional aerospace alloys. Figure adapted from [152].

2.6. Literature Review Conclusions

Published literature data on the fatigue behavior of the EBM-processed Ti-6Al-4V has been reviewed and compared to traditionally-manufactured bimodal and lamellar parts. Although the data is somewhat limited, relevant observations and conclusions can be made. Anisotropic fatigue resistance is observed in the as-built/as-built condition as horizontally-

oriented parts appear to have a greater fatigue resistance. The vertically-oriented parts are more susceptible to the rough surface finish inherited by the melt pool solidification and partially-sintered powder inclusions. Machining may serve as a method to mitigate the orientation effects. HIPed and machined EBM parts have comparable, and sometimes superior, fatigue resistance relative to traditional bimodal, lamellar, and wrought microstructures. This could be observed because a finer grain structure can be obtained through the rapid quench and in-situ anneal in EBM (and retained after HIP) compared to some traditionally manufactured microstructures. HIP alone has been shown to be ineffective at increasing the fatigue life, but reduces scatter in the fatigue data providing a more predictable material by homogenizing the microstructure, eliminating the porosity, and maximizing the load bearing area. Annealing or stress-relief heat treatments are not required post EBM-fabrication because residual stresses are essentially relieved in-situ. Surface roughness, porosity-related defects, and microstructure are the most significant factors driving fatigue-damage tolerance of EBM parts. Although the tensile strength of EBM-fabricated Ti-6Al-4V is superior to other common aerospace alloys, without post-process machining and HIP the fatigue performance is limited. It is therefore necessary to HIP and machined the parts post-fabrication to fully utilize the superior mechanical properties and fatigue behavior.

EBM additive manufacturing can provide benefits over traditional manufacturing methods like forging or casting because of the high degree of geometric design freedom and the capability to alter process settings to control the resulting microstructure. Further research

making direct connections between the melt strategies, process parameters, and post-processing steps on fatigue behavior is required to utilize all the advantages of using EBM as a feasible and reliable technique for manufacturing flight-critical components. Most studies in the literature study axial fatigue data, which may not be representative of service fatigue performance. It was identified in the literature that there is a lack of fatigue data that is more representative of service parts than axial fatigue test data with only simple dog-bone shaped samples with no internal features. The literature has identified the need to study fatigue in different loading conditions [32]. A study was conducted on EBM fabricated Ti-6Al-4V using 4-point bending, but only with simple rectangular bars [125]. Another study conducted fatigue tests on EBM bracket-type parts (similar to one found in aerospace applications) [85], but discussed the need for a special test fixture, fasteners, and machining which limited the amount of replicates and increased the costs and complexity of the experiments. Thus, this project uses a loading scheme to study the flexural fatigue strength of rectangular samples with internal geometries representative of internal cooling channels or fastener holes in service parts using a simple 4-point bend test set up.

3. MATERIALS AND METHODS

3.1 Build Design and EBM Variables of Interest

3.1.1. Build Design

The build for this study was designed such that the parameters of interest could be varied and tested while maximizing the amount of test specimen that could be machined from a single build. This was to avoid any inter-build variations, or variations that occur across multiple builds such as differing powder chemistries [153]. CAD models of both the initial build and an example test bar are provided in Figure 31.

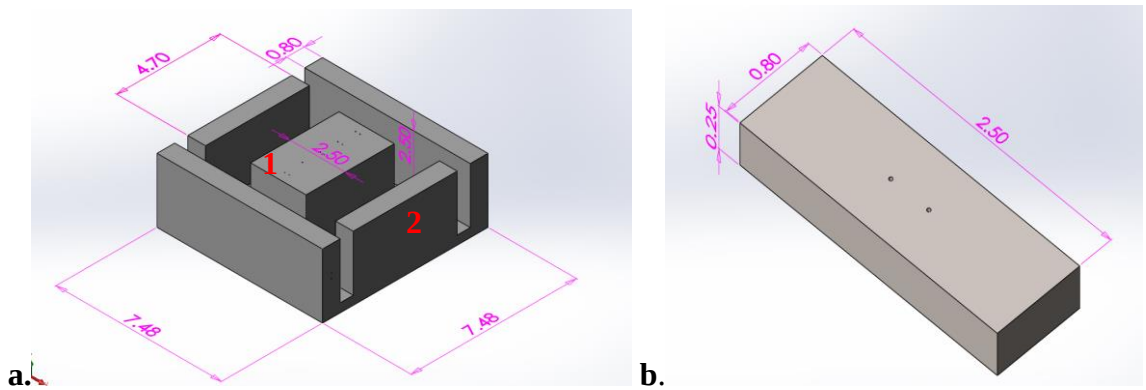

a. **b.**

Figure 31. Computer models of the build design (a.) and example 4-point bend test specimen (b.). The numbers (1 and 2) in a. represent parts with different wall thicknesses. Dimensions shown are given in inches.

The build was designed to test different variables: build orientation, local surface finish, beam path, and part thickness. The EBM material will also be compared to traditionally manufactured Ti-6Al-4V specimen. An estimated total of 145 test specimen can be machined and tested from a single build, but due to machining and testing limitations, not all will be tested. An excess of test specimen provided enough material to test all variables

for fatigue performance while accounting for machining loss, microstructural analysis, and tensile testing.

3.1.2. Build Orientation

In EBM additive manufacturing, it has been observed that the microstructure differs depending on the plane of observation. Thus, a fatigue crack will have to propagate through different microstructures depending on the orientation of the test specimen. Figure 32 displays the orientation of test specimen with respect to microstructure where 'H' denotes horizontally oriented and 'V' denotes vertically oriented specimen. Horizontally oriented parts show a relatively equiaxed microstructure on the crack propagation plane while a crack will have to cross the columnar prior β grains in vertically oriented specimen.

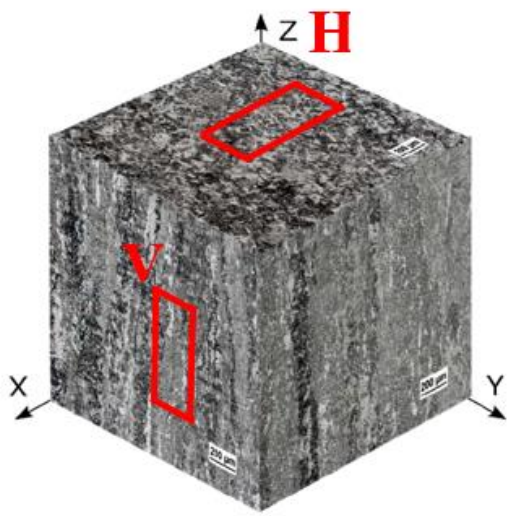

Figure 32. Test specimen orientation where 'H' indicates an example horizontally oriented specimen and 'V' an example vertically oriented specimen. Figure adapted from [154].

3.1.3. Local Surface Finish

The local surface finish, which has a profound effect on fatigue life, is investigated. The sides of the 4-point bend test specimen will either be machined and fine-ground or left in the as-built condition. In addition, the stress concentrating holes will either be incorporated into the EBM build itself (referred to as 'as-built holes') or machined to final dimension. Machining will consist of either a traditional drilling operation through bulk material (referred to as 'machined holes') or a reaming operation to ream a partially built hole from the EBM process to the final dimension (referred to as 'reamed holes'). These two different machining operations establish the scan path test variable.

3.1.4. Scan Path

The test specimen with the 'as-built' or 'reamed' holes will undergo a different scan path than the 'machined holes' specimen. Incorporating the hole into the original EBM build altered the scan path by breaking up the electron beam scan. By changing the scan path, the porosity distribution near the hole is expected to differ among the specimen and influence the fatigue life.

3.1.5. Part Geometry and Wall Thickness

As previously stated, the part size or wall thickness of EBM fabricated parts has been observed to influence the microstructure where thinner walled specimens have a finer microstructure than thicker walled specimen. Test specimen were machined from original blocks with different volumes and wall sizes. Referring to Fig. 31a., the center block (denoted block 1) has a greater wall thickness than the exterior block (block 2). The two

blocks are expected to experience different energy inputs, thermal histories, and therefore have different microstructures. It should be noted that the blocks have different locations within the build plate's X-Y plane. Literature has shown only minor (< 3%) difference in mechanical strength [86] and no appreciable differences in microstructure [91] for parts built with different locations on the X-Y plane.

3.1.6. Materials

Ti-6Al-4V powder used in this study had a chemical composition given in Table 3.1 and adhered to ASTM Standard F294-14 [155]. The particle size distribution was measured using laser diffraction on a Horiba LA950 analyzer. The powder used in this study had a mean particle diameter of 82.0 μm with a standard deviation of 21.7 μm. For baseline comparison purposes, test bars were machined from a grade 5 Ti-6Al-4V rectangular bar. The conventional Ti-6Al-4V material was supplied by RTI and the chemistry adhered to ASTM F-136 [123] and was expected to be in the mill annealed or bimodal condition.

3.1.7. EBM Build Parameters

An Arcam Q10 machine, shown in Fig. 33, located at the Manufacturing Demonstration Facility at Oak Ridge National Laboratory was used to fabricate the blocks for this study. The build parameters and conditions are outlined in Table 2. The machine used control version 5.0.104.6584 and the total build time was 29 hours, 44 minutes, and 22 seconds with an average build time per layer layer of 0.76 minutes. A figure of the final build before machining is provided in Fig. 34.

Table 2. Chemical Composition of Ti-6Al-4V Powder

Aluminum	6.530	5.50-6.75
Vanadium	4.050	3.50-4.50
Iron	0.190	<0.30
Oxygen	0.107	<0.20
Carbon	0.020	<0.08
Nitrogen	0.017	<0.05
Hydrogen	0.0031	<0.015
Yttrium	<0.0005	<0.005
Other	0.025	<0.10
Titanium	Balance	Balance

*ASTM Standard F2924 – 14

Figure 33. Arcam Q10 Machine used in this study.

Table 3. Summary of the EBM Build Process Conditions and Parameters

Build Plate Temperature (°C)	Beam Speed (mm/s)	Energy Dump Speed (mm/s)	Average Beam Current (milliAmps)	Average Beam Power (Watts)	Layer Thickness (mm)	Chamber Pressure (mbar)	Focus Offset (milli Amps)
560-562	45.40	45.473	28	250.9	0.05	0.004	32

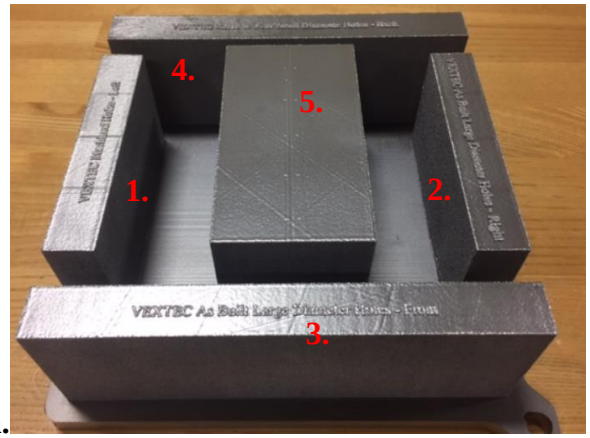

a.

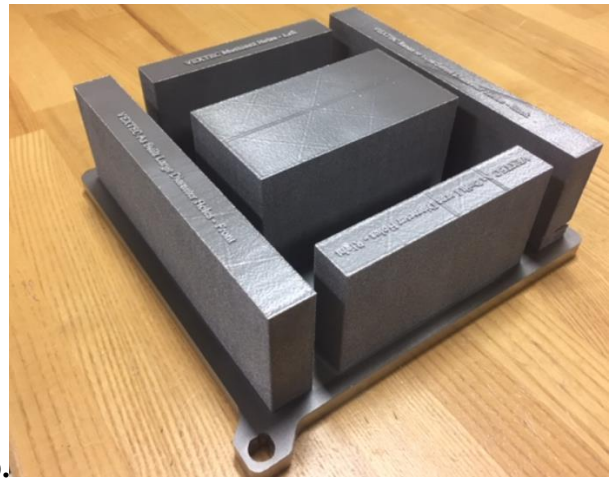

b.

Figure 34. EBM build prior to machining.

3.1.8. Experimental Matrix - Four Point Bend Fatigue Tests

The different material conditions compared in the 4-point bend fatigue tests are summarized in Table 4. The material conditions were set up to test all four EBM build variables and then compare the EBM processed samples to conventional Ti-6Al-4V processed by traditional methods.

Table 4. Experimental Test Matrix – 4 Point Bent Fatigue Testing

Material	**Orientation**	**Original Block Size**	**Beam/Scan Path (Reamed or Machined Holes)**	**Side Surface Finish**
EBM	Vertical	Small/Exterior	Machined	As-Built
EBM	Vertical	Small/Exterior	As-Built	As-Built
EBM	Vertical	Small/Exterior	Machined	Fine-Ground
EBM	Horizontal	Large/Interior	Reamed	Fine-Ground
EBM	Horizontal	Large/Interior	Machined	Fine-Ground
EBM	Horizontal	Small/Exterior	Machined	Fine-Ground
EBM	Horizontal	Large/Interior	As-Built	Fine-Ground
Conventional	-	-	Machined	Fine-Ground

3.2. Procedure

3.2.1. Microstructure Characterization

For metallographic analysis, the samples were hot mounted in conductive bakelite, mechanically ground using SiC papers and final polished using a 0.04 μm Colloidal Silica suspension on a Struers MD-Nap polishing pad. To reveal the microstructure, the samples were immersion etched using a Krolls Reagent etchant of 100 mL water, 6 mL HNO3, and 3 mL HF. The α lath thickness was measured using the method outlined by Vander Voort [156]. The method consists of calculating the mean random spacing, σ_r, by dividing the

number of α laths that intersect a test line, M, by the length of a circle with a known radius, R, to obtain, $N_L = 2\pi R/M$. Taking the reciprocal of N_L yields σ_r. The mean true spacing, σ_t, is calculated by dividing σ_r by 2. Circles of known diameter were superimposed on two different images at 1000x magnification using ImageJ software in an unbiased manner and a total of 6 measurements were taken.

The microstructural features were imaged and characterized using a Leica DM4000 optical microscope. Fracture surfaces and crack initiation sites were imaged using a Zeiss EVO MA15 scanning electron microscope (SEM) operated at 20.0 keV at multiple magnifications and a Keyence VHX 5000 digital light microscope.

3.2.2. Vickers Microhardness Measurements

Vickers microhardness indentations were taken to observe and quantify the effects of block size, distance from build plate, and orientation on microstructure, specifically lamellar thickness. Samples from the interior large block and exterior small block were sectioned approximately 0.24” (6 mm) from the top of the build, midway from the bottom build plate (approximately 1.5” (38 mm) from the build plate in the large block and 1” (25.4 mm) in exterior block), and 0.24” (6 mm) from the bottom of the build nearest the stainless steel build plate. For each given area, samples were cut such that two different microstructural orientations could be measured. They are denoted ‘XY’ where the plane observed is parallel to the build plate and ‘Z’ where the indented plane is perpendicular to the build plate. The microhardness measurements were performed on a Wilson VH1202 Vickers Hardness Tester at a load of 500 gf applied for a 15 second dwell time. Nine measurements

were taken on the sample in a 3x3 grid pattern spanning the sample. The process was repeated for 2 samples of traditionally manufactured Ti-6Al-4V for comparison.

3.2.3. Tensile Tests

Tensile tests were performed on vertically and horizontally oriented samples to obtain the strength of the material and to investigate any anisotropy in the tensile strength or ductility resulting from build orientation. Samples were machined on an OMAX 2626 Water Abrasive Machining Center and mechanically ground on 80 grit SiC papers to obtain a flat surface and grind away any burrs left from machining to the geometry provided in Fig. 35. Horizontal samples were machined from block 4 and vertical samples machined from block 1 (referring to Fig. 34). The tensile tests were performed on an MTS Criterion Model 45 at a crosshead speed of 0.00472 in/min (0.12 mm/min). It is important to note that due to size limitations, the sample geometry and strain rate are not to ASTM E8 Standards.

3.2.4. Finite Element Computations and Statistical Analysis

A Finite Element Analysis (FEA) and statistical analysis were performed in this study using commercial software ANSYS Academic APDL 18.1 and Minitab 18. A simple 2D plane stress structural analysis was performed in ANSYS to find the stress concentration factor of the machined 1/32” hole under tensile loading. One-way ANOVA tests were performed on fatigue tests to determine the statistical significance of relevant observations.

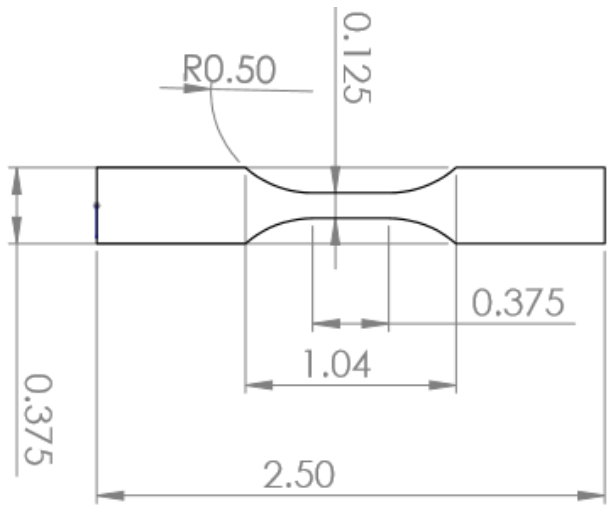

Figure 35. Geometry of tensile test samples. The sample thickness was 0.125” and the dimensions shown are in inches. Note that the geometry does not adhere to ASTM E8 standards.

3.2.5. Four Point Bend Fatigue Test Specimen Preparation and Test Set Up

The specimens for fatigue testing were machined from the larger blocks in the original build to final dimensions by a number of different machining processes. Specimen from the center block (Block 5 in Fig. 34) was first wire electrical discharge machined (EDM) into smaller sections and then water jet abrasive cut on an OMAX 2626 machine using garnet abrasive, as shown in Figure 36a. and 36b.

a. **b.**

Figure 36. Example set up of water jet abrasive machining of a test specimen (a.) and OMAX 2626 water/abrasive machining center.

The samples were then milled to final dimensions of 0.25” x 0.8” x 2.5” (6.35 mm x 20.32 mm x 63.5 mm), have two 1/32” (0.79375 mm) holes, either drilled or incorporated into the original EBM build, placed off center with 0.2” (5.08 mm) hole spacing. Samples machined from the exterior blocks (Block 2 in Figure 3.1) were machined in the same manner but without the wire EDM rough cuts. The holes were drilled using a TiAlN coated drill bit with lubricant. In order to maximize the amount of specimen that could be fabricated from a single build and isolate the variables of interest, a degree of machining was required. The surface in tension was built such that it would need machining regardless

of orientation. To eliminate variables from machining settings such as RPM, depth of cut, and feed rate, the surfaces were polished following machining. After machining, the test specimen face under tensile loading was mechanically ground using SiC papers with water as lubricant and then polished to a 3 μm finish using a diamond suspension to eliminate any surface defects. After each polishing step, the sample was rotated 90° and the final step was always performed such that the polishing wheel rotation was parallel to the greatest length of the test specimen.

The sides surfaces of the test specimen were either left in the as-built condition with a rough surface or were machined and fine ground. Due to difficulties holding onto the samples during the final polishing step, the side surfaces were not polished to a 3 μm finish. However, the final fine-grinding step was still above the 1200 grit (i.e. used a finer grit) paper needed to reduce surface imperfections as suggested by Hemphill [152]. Fig. 37 shows a schematic of the different side-surface conditions for the 4-point bend fatigue test. No samples were machined from areas of blocks that either bordered the stainless steel build plate or top layers of the build.

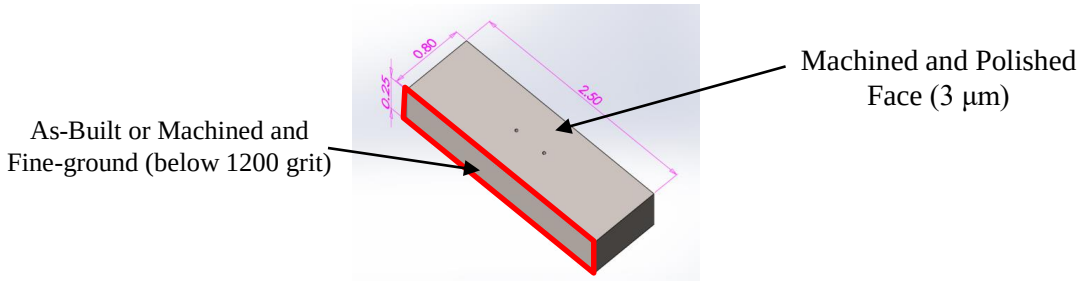

Figure 37. Schematic of different surface preparations and conditions for 4-point bend fatigue testing.

The 4-point bend test was used in this study for a number of reasons. Currently, there is a lack of open literature that report the fatigue performance of EBM-fabricated Ti-6Al-4V subjected to different loading conditions other than axial fatigue. In addition, because AM allows for the manufacture of internal features and near-net shaped parts, the test bar geometry was established to study how structures, such as internal cooling channels or fastener holes, that were additively manufactured by EBM behave during fatigue loading. This experimental design makes the test bars in this study more representative of actual service parts as opposed to round bar or dog-bone specimen in axial fatigue tests.

The second is that the 4 points of contact provide a uniform bending moment between the inner pins for uniform tensile stress across the surface, a 4-point bend test schematic and Shear - Moment (V/M) diagrams are provided in Figure 38.

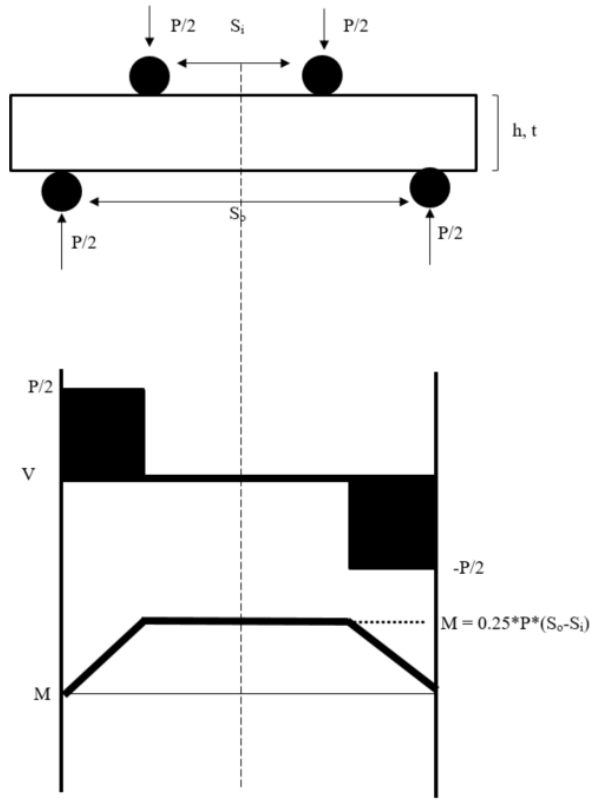

Figure 38. 4–Point bend test schematic and corresponding shear-moment diagrams.

The test set up also allows for simple sample preparation, mounting, and dismounting for interrupted fatigue tests. It is often referred to as a 'self-aligning' test [157]. In addition, the flat surface of the rectangular test specimen is convenient for studying fatigue damage. A schematic of the loading conditions and dimensions is provided in Fig. 39.

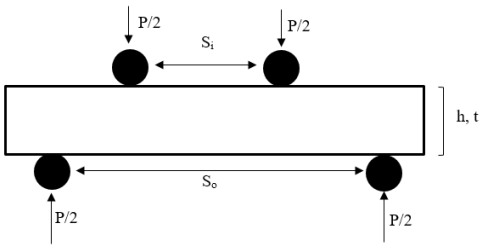

Dimension	Value
w	0.8" (20.32 mm)
h	0.25" (6.35 mm)
S_i	0.394" (10 mm)
S_o	1.575" (40 mm)

Figure 39. Schematic of the 4-point bend test set up and important dimensions.

There are two important ratios when considering the 4-point bend test for uniform stress distribution across the surface of the sample when loaded. The first is the ratio between the inner pin spacing to thickness (S_i/h) for which the ideal value is between 1.2 and 1.5 for constant surface stress distribution [157]. The second is the outer pin spacing to inner pin spacing (S_o/S_i) for which the ideal value is between 4 and 5 [157]. In this study the S_i/h and S_o/S_i ratio values are 1.575 and 4, respectively. The S_i/h ratio differs slightly from the provided ideal value. However, over the 1.2-1.5 range, the surface stress distribution was calculated to vary by 1%. The small amount of difference between the set value and ideal value range is therefore considered negligible and it is more advantageous to the test to have a ratio over the identified values than under. The thickness, h, was set at 0.25" (6.35 mm) because it was identified that samples around this thickness consistently initiated a fatal crack in the middle of specimen between the two inner pins while thinner specimen

tended to fail near the pins [157]. The tensile stress across the surface in a 4-point bend test is defined in Equation 3

$$\sigma_{tensile} = \frac{3 * P * (S_o - S_i)}{2 * w * h^2} \qquad (3)$$

which is derived from the beam theory of engineering mechanics. In Equation 3, the variables are the same as those defined in Fig. 39 and P is the applied load. The stress across the surface of the test specimen, $\sigma_{tensile}$, is derived in the following by taking a cut about the center axis of the test specimen (or beam).

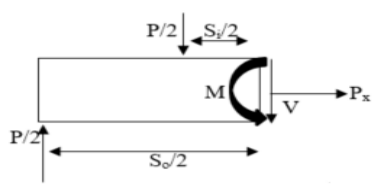

Free Body Diagram - Cut about the center axis of beam/test specimen

$$\sum F_x = 0 = P_x$$

$$\sum F_y = 0$$

$$\frac{P}{2} - \frac{P}{2} + V = 0$$

$$V = 0$$

$$\sum M = 0$$

$$\frac{P}{2} * \frac{S_o}{2} - \frac{P}{2} * \frac{S_i}{2} - M_c = 0$$

$$\frac{P}{4} * (S_o - S_i) - M_c = 0$$

$$M_c = \frac{P}{4} * (S_o - S_i)$$

$$\sigma_{tensile} = \frac{-M_{max} * y}{\bar{I}}$$

$$\sigma_{tensile} = \frac{-\left(\frac{P}{4} * (S_o - S_i)\right) * -\frac{t}{2}}{\frac{b * h^3}{12}}$$

$$\boxed{\boldsymbol{\sigma_{tensile} = \frac{3 * P * (S_o - S_i)}{2 * b * h^2}}}$$

The fatigue tests were performed with an R ratio ($\sigma_{min}/\sigma_{max}$) of 0.1 at a load frequency of 5 Hz on a load-controlled MTS 810 servo-hydraulic test machine. A low frequency of 5 Hz was chosen because the test specimens are not rigidly fixed to the test rig. Higher frequencies could cause the specimens to move and damage the machine. The R ratio and load frequency have an effect on the fatigue cycles to failure [25, 134, 158]. A low R ratio of 0.1 was chosen to minimize the crack growth rate of long cracks, which has been shown to increase with increasing positive R ratio (provided a constant ΔK, note that ΔK_{th} decreases with increasing R) [159, 160]. However, the opposite has been observed in literature for short cracks [161]. The literature provides multiple definitions of short and long cracks [162], but in general a long crack is typically defined as at least several millimeters long [163]. The greater the test frequency (the more stress cycles per second), the greater the fatigue strength [134, 158].

Selected tests were stopped at various cycle intervals and fatigue crack growth measurements were taken using a Keyence VHX 5000 digital light microscope. Two horizontal and vertical specimen were chosen for the interrupted fatigue tests in order to compare crack initiation, propagation, and growth rates between the two orientations. If multiple cracks initiated from the same hole, they were treated as independent cracks and measurements were taken from the larger crack that was first to initiate. The measurements were stopped when the crack reached the edge of the specimen or if the specimen failed. If the latter occurred, the crack was given a length of one half the sample width and plotted against the cycles to failure. The method is similar to that outlined by de Matos [164].

4. RESULTS AND DISCUSSION

4.1 Microstructure

The Ti-6Al-4V fabricated during the EBM process in this study exhibited a continuous structure with Widmanstätten or basket weave and colony morphologies of the α platelets. Figure 40 shows optical images of the microstructure in two orthographic planes, Z (perpendicular to the build plate) and XY (parallel to the build plate). Columnar prior β grains delineated by α_{GB} phase extending multiple build layers in the build direction were observed. In the XY planes (those parallel to the build plate), the prior β grain morphology was more equiaxed, thus the grains are thought to have a rod like shape. This type of microstructure has been widely reported in the literature for EBM-fabrication of Ti-6Al-4V obtained by rapid quench from melt and then in-situ anneal [101, 117, 165, 166]. No martensite was observed in the microstructure, but lack of fusion defects and gas pores were found. Average α lath width was measured to be 2.93 +/- 0.83 μm. Lath widths of 0.66 – 4 μm [91, 104, 126] have been reported in the literature. A wide range of lath sizes are possible due to different build heights [104] , wall thickness [167], and EBM annealing time [91]. The average lamellae width observed in this study is on the upper end of those reported in literature because of the relatively large block sizes the samples were sectioned from.

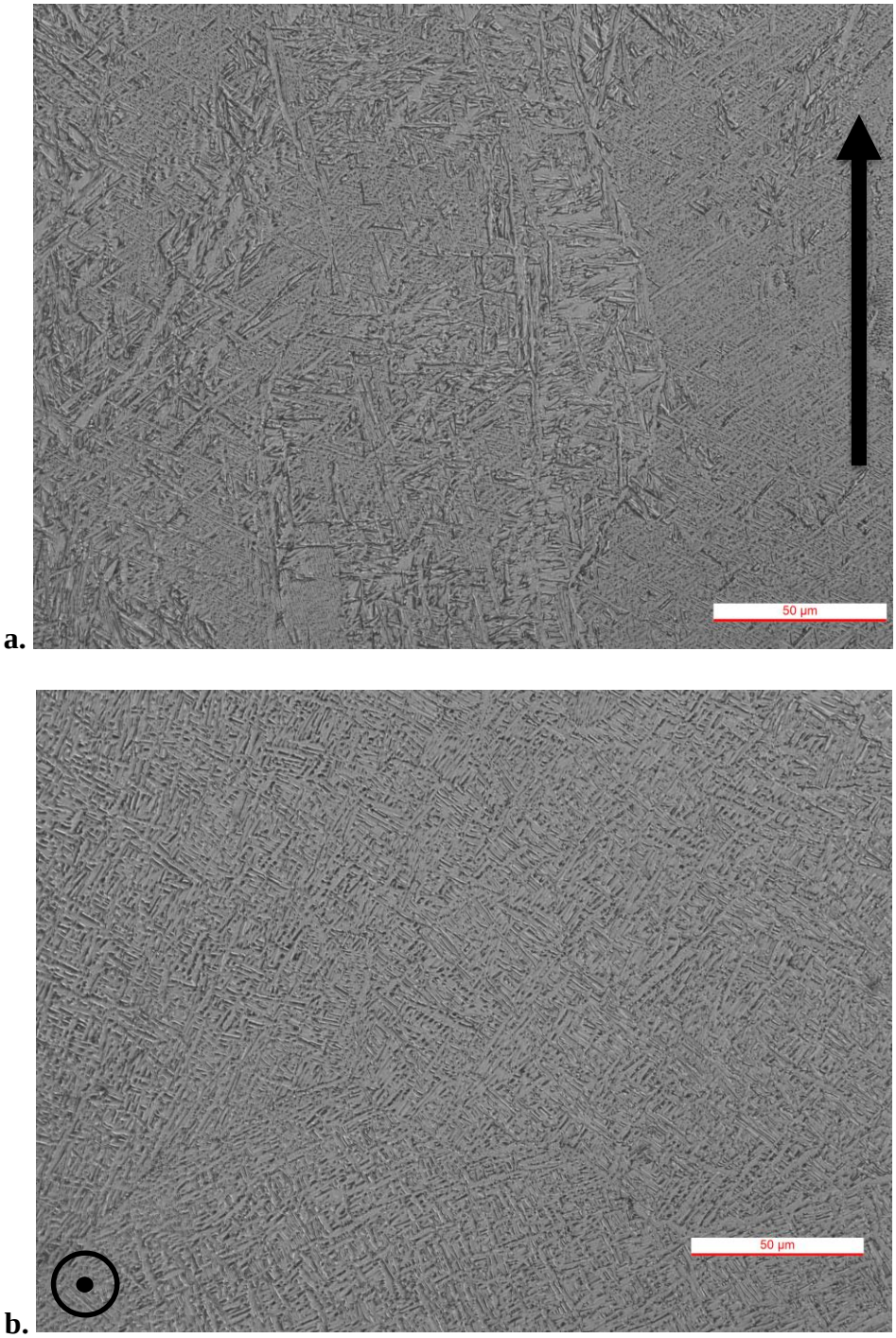

Figure 40. Optical micrographs of the microstructure sectioned from block 1 in 2 different orthographic planes; Z (a.) and XY (b.).

4.2 Vickers Hardness Indentations

The results of the Vickers micro-hardness indentations are presented in Figure 41. The Vickers hardness in the EBM material ranged from 304 to 388 HVN but on average was consistent over build volume, distance from build plate, and orientation.

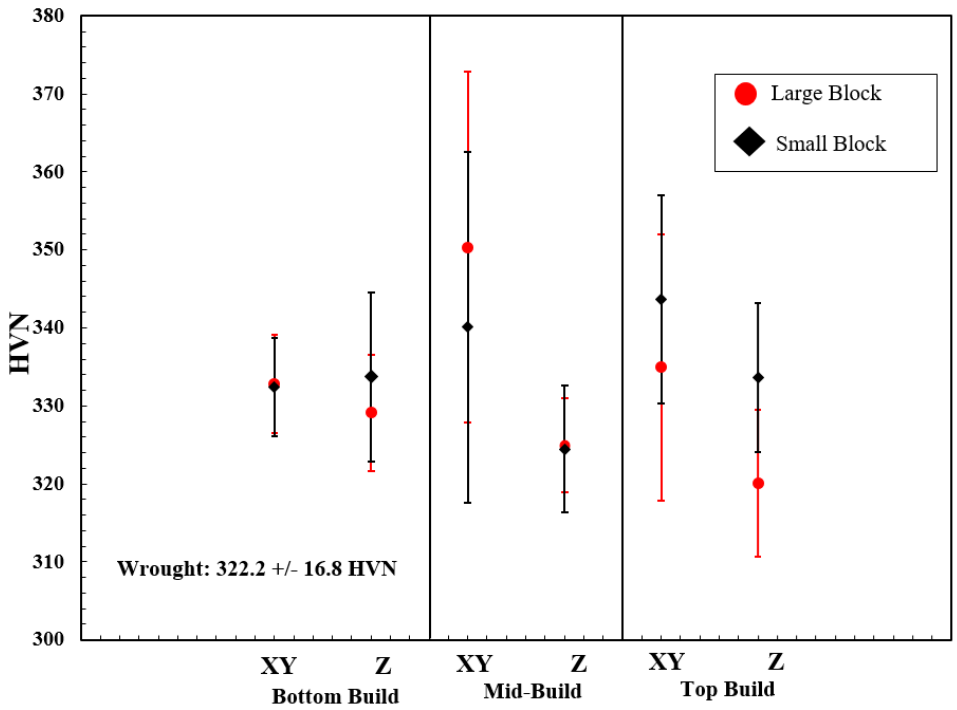

Figure 41. Vickers micro-hardness measurements as a function of distance from build plate, block volume, and orientation.

The average HV of the smaller block and larger block were 332 +/- 6.5 and 334.0 +/- 5.6, respectively. The conventional had a lower average micro-hardness when compared to the EBM material (322. 3 +/- 16.8), but did not differ significantly. The hardness values of the EBM material are similar to those reported in literature as a sample with a wall thickness of 20 mm was reported to have an average Vickers hardness of 330 [77].

The hardness of a material is defined by its resistance to permanent deformation [168] and microstructural features, EBM process conditions, and thermal history affect the Vickers hardness of Ti-6Al-4V [102, 104, 169, 170]. The Vickers micro-hardness follows the Hall-Petch Relationship, given in Equation 2, where the hardness is inversely proportional to the square root of grain size [170, 171].

$$\boldsymbol{VHN} \propto \frac{\mathbf{1}}{\sqrt{\boldsymbol{d}}} \tag{2}$$

Based off the Vickers hardness measurements and assuming the Hall-Petch Relation, it appears that the lamellar spacing in this build is independent of build orientation, distance from build plate, and orientation and is homogenous throughout the build. This is in contrast to other authors who observed microstructural coarsening near the tops of builds because the first layers were closer to the heat sink stainless steel build plate [8, 10, 107, 172]. Others observed grain refinement near the tops of the builds because the top of the build had lower annealing time [9, 88, 91]. No trend was observed in this study indicating that the refinement or coarsening as a function of build height is dependent on other factors like the support structures, geometric height, and surface area in contact with the stainless steel build plate. No material that was directly touching the build plate was tested in this report.

The wall thickness affects the cooling rate and microstructure of EBM parts. It is documented in literature that thin sections of EBM fabricated Ti-6Al-4V contain both the α′ phase and a fine α+β from lower energy input during the build process and increased cooling rate [77, 100, 173]. Thicker sections that receive more energy input only contain

the α+β phase with no α′. The blocks fabricated in this study have a greater wall thickness than those reported by Wang [173] needed for complete decomposition of martensite so no martensite is expected to be present in the microstructure.

Although no martensite is expected and the average hardness values are relatively consistent throughout the build, the scatter in the data can be attributed to the texture and orientation of the α phase as the hardness of the α phase varies with orientation [23, 174]. The HCP α phase has a limited number of slip systems so the energy required for slip to occur varies with orientation with respect to the loading direction [175]. Slip occurs on the closest packed planes and planes with the highest packing density are governed by the *c/a* lattice parameter ratio. For α Ti, the *c/a* ratio is less than the ideal value of 1.633 [23]. The prismatic planes ($\{10\overline{1}0\}$ and $\{11\overline{2}0\}$) have a higher packing density than the basal plane ($\{0001\}$) [35] so slip occurs preferentially on prismatic planes [175-177] or pyramidal depending on alloying elements [178]. Basal planes are the least preferential for slip. If the α grains are oriented such that their basal planes are perpendicular to the loading direction, the hardness measurements will be significantly higher than those of other grain orientations [65, 175, 179].

The blocks fabricated in this study were all about 2.5” tall, had significant contact with the build plate with no supports, and had wall thicknesses much greater than 5 mm. It appears that although the parts were short with significant contact with the build plate, the large volume was sufficient for complete α′ decomposition and the lamellar spacing is relatively

consistent throughout the build although some different orientations of the α grains can lead to some scatter in the HVN data.

4.3 Tensile Tests

The tensile test experimental results, provided in the engineering stress vs. engineering strain curves in Fig. 42 and average values in Table 5, produced 0.2% Offset Yield Strength (YS) and Ultimate tensile strength (UTS) values comparable to those found in the literature [82].

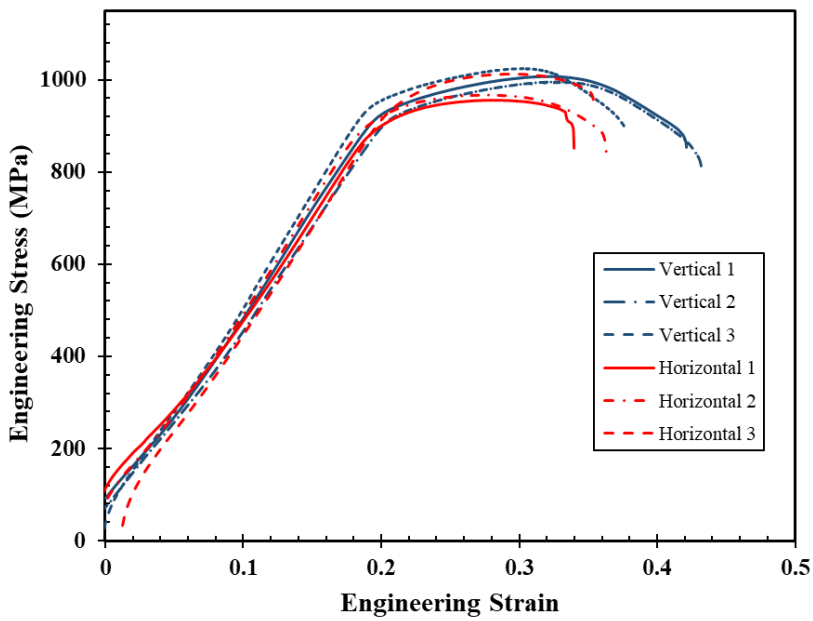

Figure 42. Tensile test results presented as engineering stress/engineering strain curves.

Table 5. Average Tensile Properties

	YS (0.2% Offset) (MPa)	UTS (MPa)	% Elongation
Vertical	938.37 +/- 16.5	1009 +/- 14.1	41.6 +/- 1.8
Horizontal	932.77 +/- 20.3	978.6 +/- 30.1	35.0 +/- 1.5

Although the horizontal oriented specimen had lower average YS and UTS, the values were within a standard deviation of the vertical specimen. The elongation to failure observed in this study is much greater than values reported in the literature. Because the elongation at failure of Ti-6Al-4V is strain rate sensitive [180, 181], a decrease in tensile strain rate increases the elongation at failure. Due to machine limitations, the crosshead speed of the tests was roughly 15% lower than what is specified by ASTM E8 for this geometry and could have increased the tensile ductility. As a material is loaded at a slower rate, there is a higher probability for small amounts of local plastic deformation to occur. The strain rate sensitivity has also been reported to be related to thermal activation of dislocations where the ability of thermal activation to assist dislocation motion is limited at high strain rates [182].

In opposition to the strain rate, because Ti-6Al-4V has positive strain rate sensitivity, the tensile strength normally decreases with decreasing strain rate [3]. However, the YS and UTS both exceed many values reported in the literature. It is possible the water-jet abrasive cutting could have induced residual compressive stresses at the surface eliminating any strain rate effects on tensile strength.

Although the YS and UTS do not appear to be affected by orientation, the average ductility for the vertically oriented specimen is greater than the horizontally oriented specimen. In metal additive manufacturing in general, the surface roughness [105], defects [183], and microstructural anisotropy [184] can affect the ductility of Ti-6Al-4V. A number of authors

found similar trends where the strengths were similar regardless of build orientation but the ductility was superior in the vertical orientation compared to the horizontal orientation of EBM-fabricated [94, 185, 186] and direct energy deposition fabricated [187] Ti-6Al-4V. However, the opposite, where the ductility of horizontal samples was superior to vertical, has also been reported but may have been effected by porosity and out of specification oxygen content [102]. It has also been observed that horizontally-oriented specimen had superior tensile properties compared to vertically-oriented because of the orientation of LOF defects reducing the load bearing area and increasing the local stress concentration [103]. Because the vertically-oriented specimen in this study show superior strength, defects are not expected to have influenced tensile strength or ductility. Furthermore, the machining process eliminated any surface roughness. It is expected that the difference in ductility can be attributed to the microstructural anisotropy. In the vertical orientation, the prior β grains in the samples are parallel to the loading axis. According to Zhai, during deformation of vertical specimen a larger amount of grains contribute to necking and the samples can withstand more deformation without fracture resulting in higher ductility [186]. In the horizontal specimen, the prior β grains are perpendicular to the loading axis. This orientation makes intergranular fracture more favorable as fracture occurs along the weaker continuous α layer leading to a reduction in the ductility [188].

Among the variables investigated in this study through tensile testing (orientation) and Vickers hardness (block thickness, orientation, distance from build plate), the mechanical properties were consistent. It should be noted, however, that other authors have identified

inconsistencies of microstructure and mechanical properties within large blocks [189] and build plate location [86, 91]. It was found that a single large block contained inhomogeneous microstructure as both α′ and α+β phases were observed and the tensile strength varied throughout the build [189]. The variation in tensile strength was attributed to an increased amount of porosity in edge samples compared to interior samples machined from the block.

The tensile tests and Vickers hardness were conducted, in part, to show microstructural and mechanical property homogeneity throughout the build and allow for the assumption that the parts used for the 4-point bend tests were microstructurally similar. Based off the results, orientation, distance from build plate, and wall thickness does not appear to affect the strength of the parts. However, the ductility of 4-point bend test specimen could vary as a function of build orientation. The location on the build plate the samples were machined from was not considered and therefore could introduce an unknown variable.

4.4 ANSYS Structural Simulation and Stress Concentration Factor

A finite element structural simulation was performed to obtain the stress concentration factor (SCF) of the hole in the test specimen. ANSYS Academic 18.1 APDL was used in the analysis. A 2-D model of the test specimen was created in ANSYS. The dimensions of the 2-D model were 0.8”x1.575” (20.32 mm x 40 mm) with the 1/32” (0.79375 mm) holes off center with 0.2” (5.08 mm). The Young’s Modulus was 1.6027 E7 MPa (an average of the values provided by Lewandowski et al. [82]) and the Poisson’s’ Ratio set at 0.342, the value provided by ASM [190]. The model represents the test specimen between the two

outer pins and assumes uniform tensile stress. Because the model is 2-D, plane stress with arbitrary thickness was assumed sufficient for the analysis. The elements used were SOLID8 QUAD 183 because they can tolerate irregular shapes without loss of accuracy [191]. Although the model could be simplified for symmetry, it is simple enough for a full analysis without excessive computation time. The ANSYS simulation parameters are given in Table 6.

Table 6. ANSYS FE Analysis Parameters

Analysis Type	Static Structural
Material Type	Linear-Elastic Isotropic
Element Type	Solid 8 Quad 183
Size	Fine (Mesh size = 1)
Number of Elements	2921
Element Behavior	Plane Stress

A schematic of the geometry and loading conditions in addition to the Nodal Solution for Von Mises' stress is provided in Fig. 43 and Fig. 44, respectively. The SCF, K_t, is defined by the highest value of actual stress near a discontinuity over the nominal stress, $\sigma_{Applied}$ in Fig. 43, and defined by Equation 3:

$$K_t = \frac{Highest\ Value\ of\ Stress, \sigma_{max}}{Nominal\ Stress, \sigma_{Applied}} \qquad (3)$$

$\sigma_{Applied}$ was calculated using Eq. 1 with an applied load of 2400 lbf and the dimensions shown in Fig. 43 to obtain a nominal stress of 170,078.256 psi. The von Mises Stress (von Mises, or Distortion Energy Theory, is considered because it is the best yield criterion theory for ductile materials [192]) at the hole calculated by ANSYS is 463,702 psi to obtain

a SCF of 2.726. The theoretical SCF was estimated to be 2.8 using the chart obtained in [193]. The calculated SCF was within 2% of the theoretical solution, thus the model is considered accurate and the SCF can be used.

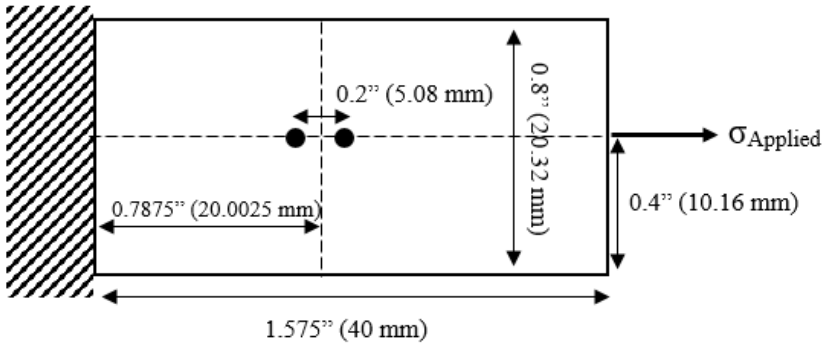

Figure 43. Schematic of the geometric set up and loading conditions for the ANSYS FEA Simulation.

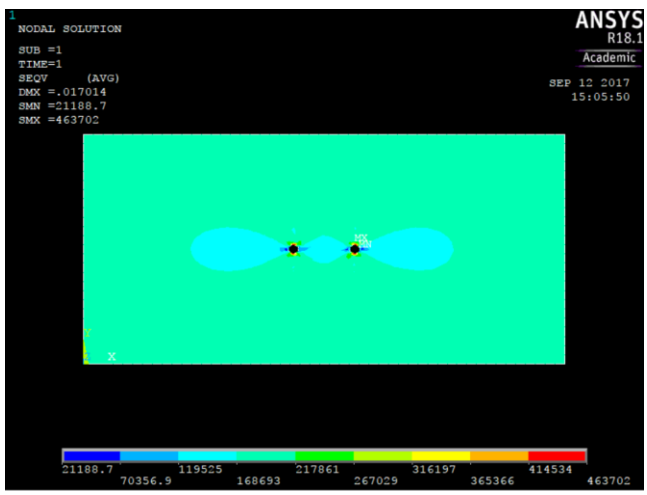

Figure 44. Nodal solution stress contour plot of the Von Mises Stress of the solved model.

The average stress concentration of an as-built EBM surface was calculated to be 3.28 [194] with a severe stress concentration factor of 9.1 at surface crack initiation sites [139] (calculated using the elastic stress concentration factor for an elliptical notch [195]) . Thus,

for parts with an as-built surface in this study, a fatigue crack can be expected to initiate at the surface due to notches left over from the layer-by-layer fabrication method, melt pool overlap, and partially sintered powders. The following section will examine the fatigue properties of EBM fabricated Ti-6Al-4V.

4.5. 4-Point Bend Fatigue Results

4.5.1. Surface Roughness Effects

4.5.1.1. As-Built Outside Surfaces

The rough as-built surface of EBM fabricated parts provides a higher stress concentration than the manufactured holes as previously shown by the ANSYS simulation and literature review [139, 194]. Thus, the fatigue life of specimen with as-fabricated surfaces is expected to lower than those with machined surfaces. Comparing the cycles to failure of specimens with as-built surfaces to those with the machined and fine-ground surfaces confirms this, as shown in Fig. 45. The cycles to failure are significantly reduced when the as-built surface is present.

Initial visual inspection of specimen with as-built surfaces after fatigue failure indicates that the crack that caused failure initiated at the surface and not at the machined hole. The engineered holes in the specimen with the as-built surface are largely intact while the other specimen with a machined surface has a fractured hole (Fig. 46a.). SEM fractography confirms that fatigue cracks in the vertically oriented specimen with rough as-fabricated surfaces initiate at the surface and not the fabricated hole (Fig. 46b.).

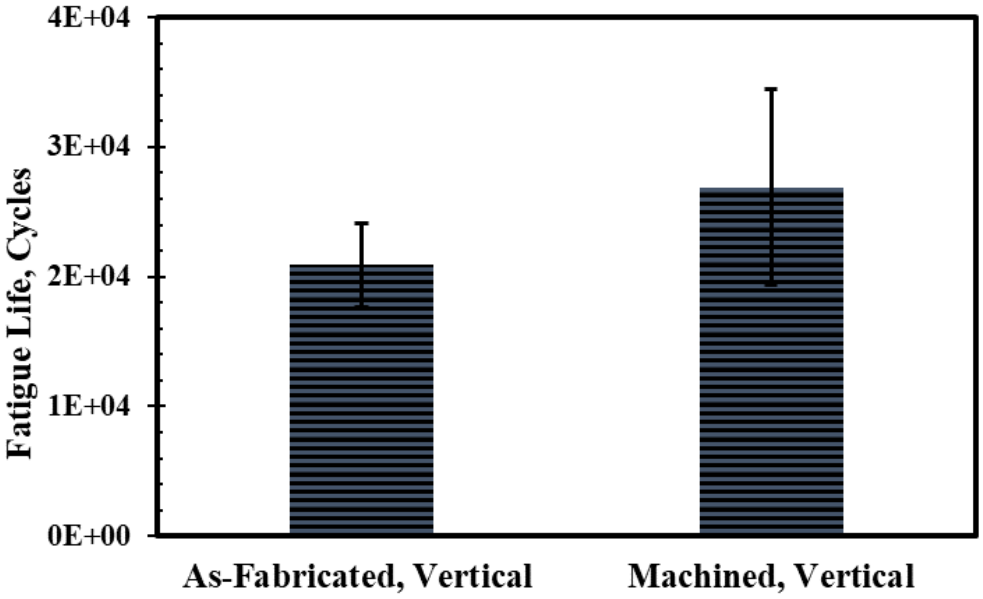

Figure 45. Average cycles to failure of EBM fabricated parts with as-built surfaces compared to specimen with machined and fine-ground surfaces. The applied stress was 585 – 590 MPa.

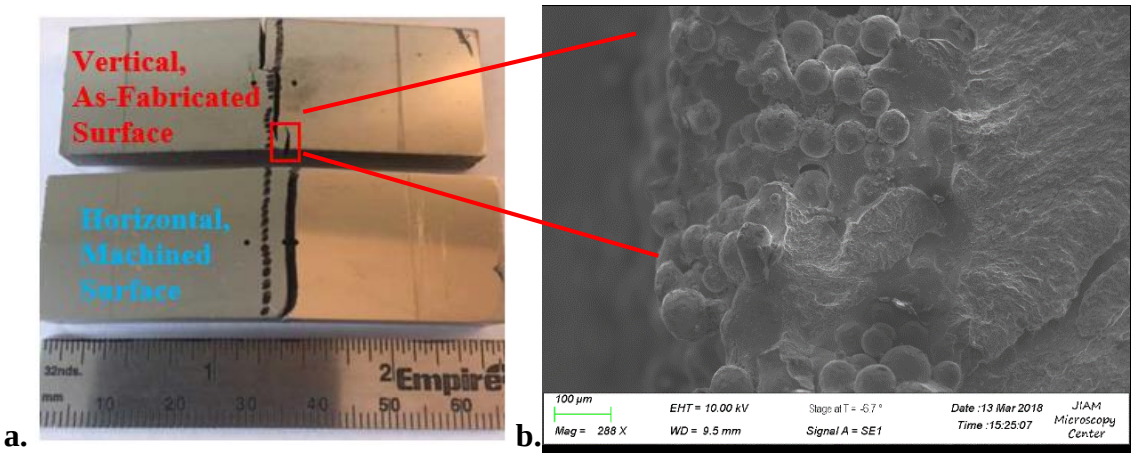

Figure 46. Images showing crack initiation and crack propagation behavior of specimen with an as-fabricated surface.

The superior fatigue strength of samples with machined and fine-ground side surfaces can be attributed to the elimination of the notches with sharp radii and partially sintered powders that act as stress concentrators and early crack initiation sites. The rough surface provides clear crack initiation sites greatly reducing the fatigue life. A SEM micrograph and an optical image of a surface profile of the rough surface are shown in Figure 47.

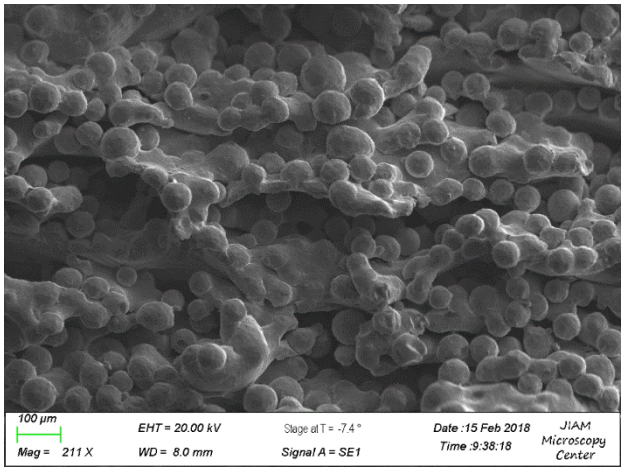

a.

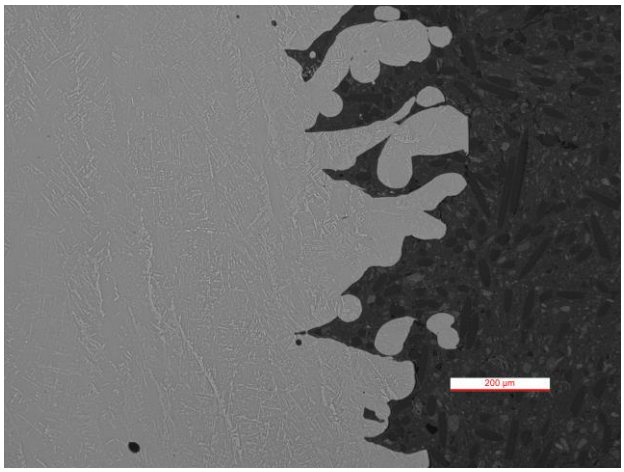

b.

Figure 47. SEM micrograph (a.) and optical profile (b.) of an as-fabricated EBM Surface.

4.5.1.2. As-Built Holes

An advantage of manufacturing with additive is the ability to create internal features for structural support, such as honeycomb structures, or cooling channels to create lightweight functional parts that would not be possible by traditional methods [196]. Additive manufacturing also presents the opportunity to reduce machining costs, time, and material [197]. It is thus important to study the effects of incorporating new geometric features, such as fastener holes or internal cooling channels, into the original build designs. Fastener holes act as stress concentrators and affect the fatigue life. Machining marks [198], surface roughness in the bore [199, 200], and less-round fastener holes [199] have been shown to decrease the fatigue life. An as-built hole, shown in Fig. 48, shows that melt pool overflow reduced the designed diameter and resulted in a less-round hole. Because the size and shape of a hole can affect the fatigue life, the surface integrity of the as-built hole can be a source of scatter in the data.

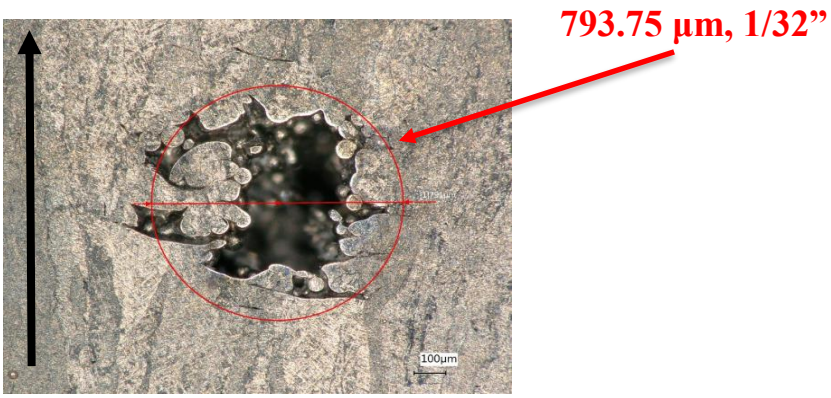

Figure 48. An image of an as-built hole. The red circle indicates the designed 1/32” (793.75 mm) diameter. The black arrow indicates the build direction.

A chart presenting cycles to failure of vertically and horizontally oriented parts comparing hole integrity is provided in Fig. 49.

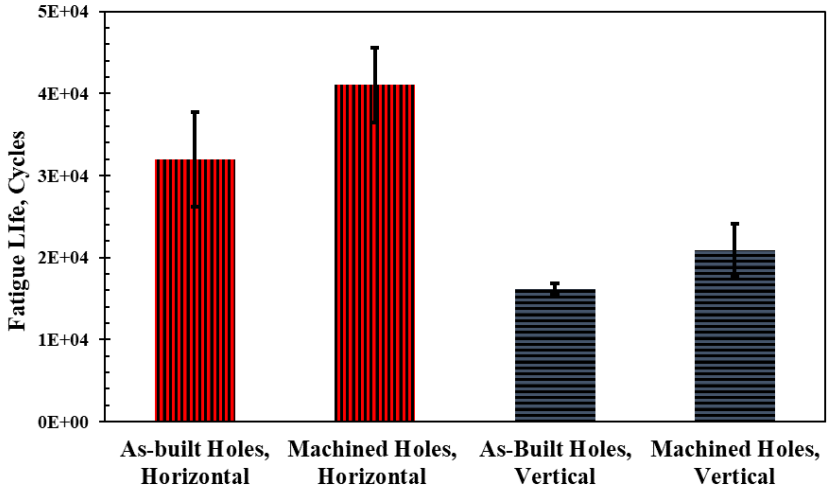

Figure 49. Average cycles to failure comparing the effects of the as-built surface in the bore of the hole to machined holes. The applied stress was 570 - 600 MPa.

The results confirm that the integrity of the hole has an influence on fatigue resistance where the rough as-built surface within the bore of the hole left by the EBM process decreases fatigue life. Fracture surface images of a specimen with an as-fabricated hole is shown in Fig. 50. Powders and partially melted zones can be observed throughout the bore of the hole.

It is important to note that the sample surfaces of the vertical and horizontal test specimen outlined in Fig. 49 differed. The horizontal had machined surfaces while the vertical specimen had as-fabricated surfaces. Despite the differing surface conditions, the results still support the expected results.

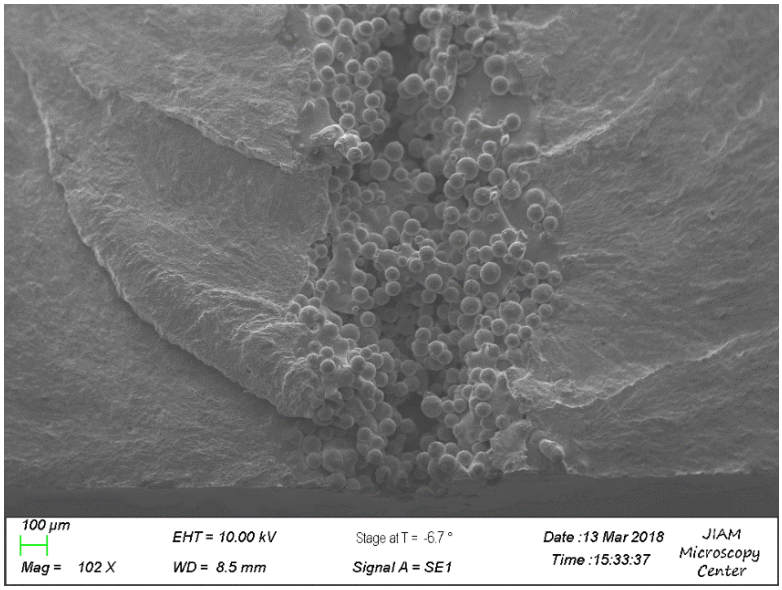

a.

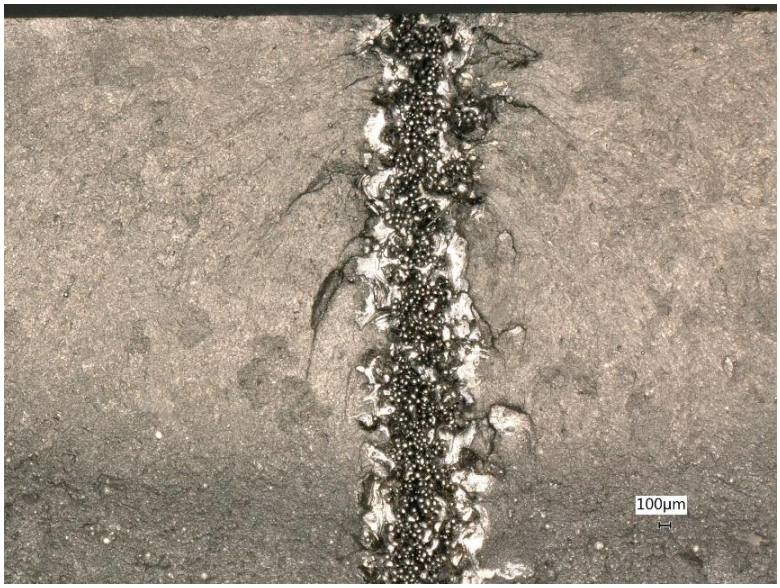

b.

Figure 50. Fracture surface of a fatigued specimen with an as-fabricated hole highlighting the partially-sintered powder and rough surface throughout the bore of the hole.

In general, as the surface roughness increases, the fatigue life decreases [139]. The experimental results in this report reflect this claim. It should be noted, however, that the difference in the fatigue life of the samples with as-fabricated surfaces, in the bore of the hole and outside edge, compared with machined surfaces is lower than expected. There are a number of reasons for this discrepancy. First, an experimental process error was made setting the stress levels the samples were tested. The applied load was kept constant but differences in sample geometry led to different stress levels. Although the samples with as-fabricated surfaces were fatigued at a lower average stress than the machined, those with as-fabricated surfaces still failed in fewer cycles. Thus, despite the set-up error, the results can still be presented and running further tests was considered unnecessary. In general, it is difficult to apply equal stresses to samples with as-fabricated surfaces because an estimated 150 μm layer is mechanically inefficient and does not support any load on the edges [117] and the as-fabricated surface is considered heterogeneous and non-reproducible [201].

4.5.1.3. Build Orientation and Surface Roughness – Combined Effects

It was observed and discussed in the literature review that the surface roughness and build orientation effects on the fatigue behavior were related. The surface roughness was more detrimental to fatigue in vertically oriented (build direction parallel to loading) parts then horizontally (build direction perpendicular to loading). This was also observed in this study. Initially, test samples were machined and approximately 0.015” - 0.020” (381 μm – 508 μm) of material was removed from the outside surfaces to make the 0.8” (20.32 mm)

specified width. Initial testing led the vertically oriented sample to fail 31,918 cycles sooner than the horizontal (vertical = 24,710 cycles to failure, horizontal = 56,628 cycles to failure). Although the surface was machined and ground, the machining depth was not sufficient to eliminate all surface roughness effects. The melt pool overflow could be observed as cracks were observed on the outside surface running parallel to the build plate (Fig. 51).

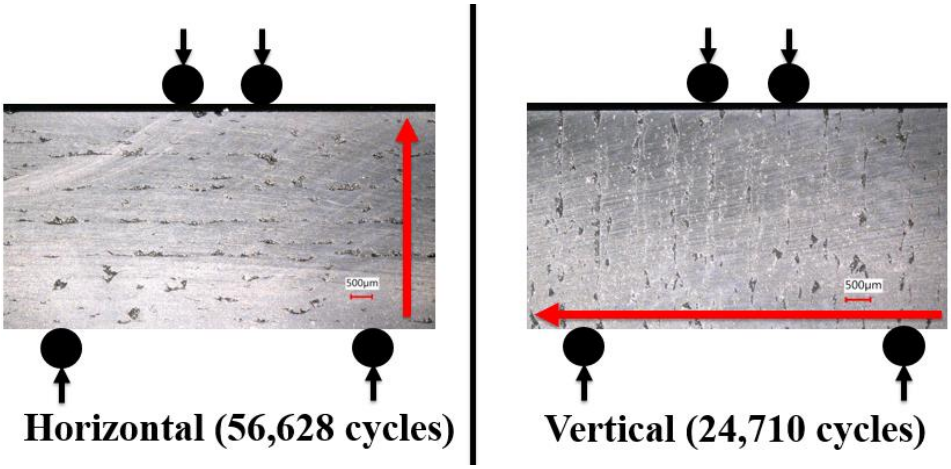

Figure 51. Optical image of surface roughness overlaid on a schematic of the 4-point bend loading, red arrows indicate build direction and black arrows loading direction.

Despite both samples having similar surface defects, the defects in the vertically-built specimen are oriented such that they are much more detrimental to fatigue than in the horizontal orientation. The 4-point bend loading essentially opens existing surface cracks in the vertical specimen. Although surface cracks were present in the horizontal samples, they do not appear to be as detrimental to fatigue.

The surface roughness appeared to dominate the fatigue behavior at the specified 0.8" sample width so the samples were machined further below the 0.0256" (650 μm) material removal threshold specified to eliminate the surface roughness [105]. Specimen geometry has been shown to impact fatigue life [202] so both horizontal and vertical samples were machined below the original 0.8" width to keep the geometries consistent. At least 725 μm (0.0285") of material was removed from both outside surfaces to eliminate all visible defects.

4.5.2. Effects of Build Orientation

4.5.2.1. Cycles to Failure

Based of observations from data collected from the literature, the axial fatigue strength of EBM-fabricated Ti-6Al-4V appears to be independent of the build orientation after machining. However, the 4-point bend fatigue tests revealed a statistically significant difference ($F = 14.39$, p-value = 0.007 when $\alpha = 0.05$) in fatigue life resulting from build orientation (Fig. 52).

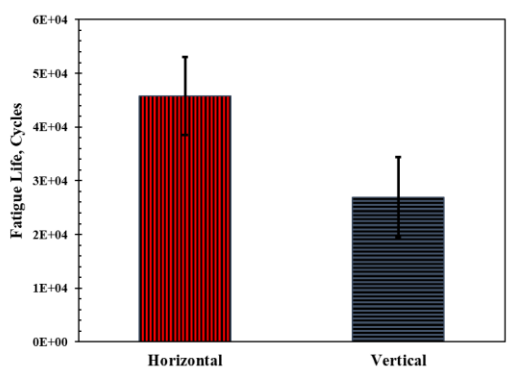

Figure 52. Bar graph showing the build orientation's influence on fatigue life of machined specimen.

Although the samples were machined and polished, the horizontal specimen had a statistically higher fatigue life than the vertical specimen at the 95% confidence interval. It is expected that the difference in fatigue life is attributed to multiple crack initiation sites that were observed in the vertical oriented specimen. Digital microscopy revealed multiple cracks initiating on the surface of the vertical samples before any initiated at the machined hole (Fig. 53).

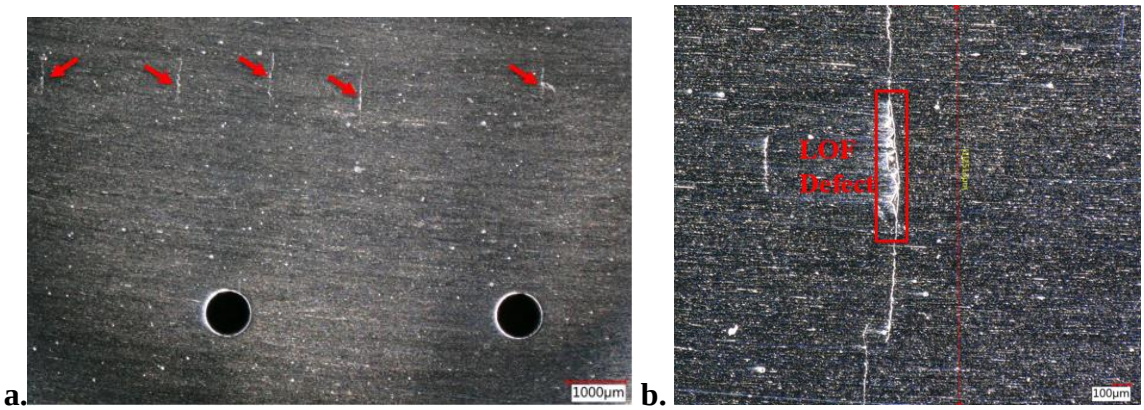

Figure 53. Interrupted fatigue test crack monitoring, image and crack measurments taken at 10,000 cycles.

During the interretpted fatigue tests, cracks in vertical specimen were observed in the polished sample surface in cycle counts as low as 7,000 cycles into the test. SEM fractography confirmed the multiple surface initation sites as LOF defects (Fig. 54). Although some of the LOF defects intercepted the surface (eg Fig. 54a.), many of the defects were located near the surface but did not intercept. Although the defects were not directly on the surface, the increased stress concentration resulted in early crack initiation.

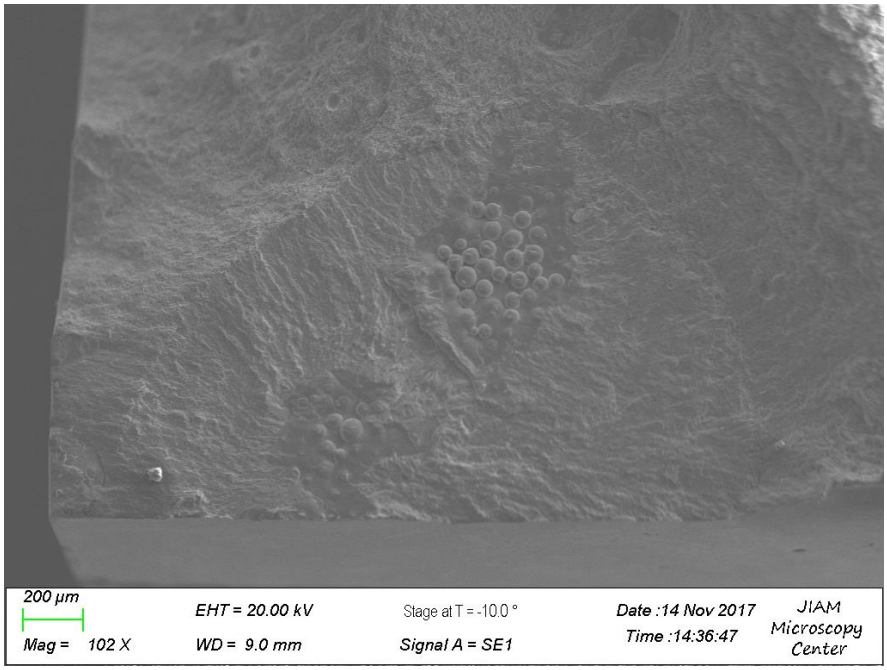

a.

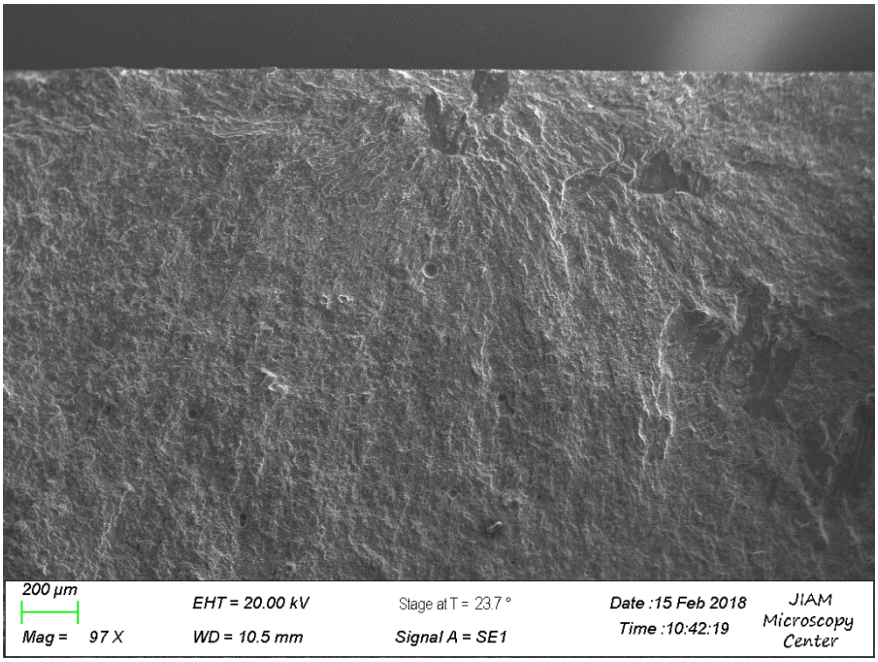

b.

Figure 54. SEM fracture surface images of vertically orientated, machined, and polished samples showing LOF defects at surface crack iniation sites near an edge (a.) and interior site (b.).

In contrast to vertical specimen, the horizontally-orientated 4-point bend fatigue specimens showed only crack initiation sites at the machined 1/32” (0.79375 mm) hole and no surface cracks. LOF defects are results of non-optimal scan parameters and found in between layers [203]. The layers in the vertical orientation are arranged such that the inter-layer LOF defects can intersect or are near the surface and provide a crack initiation site and lead to layer delamination-like failures. This is shown schematically in Fig. 55.

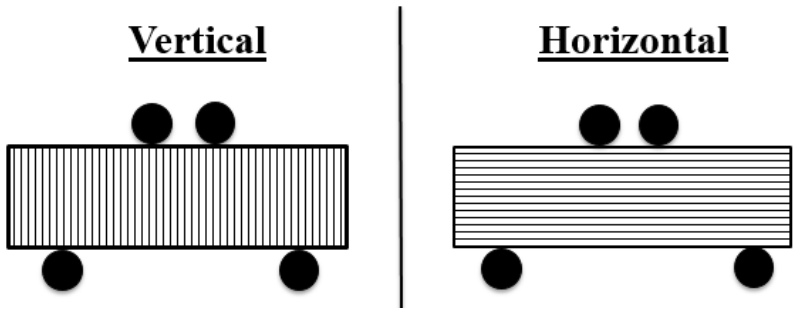

Figure 55. Schematic of the vertical and horizontal 4-point bend fatigue test specimen. The lines represent individual build layers.

During 4-point bend loading, the lack of fusion interlayer defects in vertical samples act as cracks that are being opened during loading. With horizontal samples, a single and polished layer experiences the maximum tensile stress and the LOF defects are contained within the bulk of the sample having little impact on the fatigue life.

As previously indicated, post-process HIP and machining are effective at increasing the fatigue life of EBM-fabricated Ti-6Al-4V as porosity is effectively closed by HIP and rough surface eliminated by machining. It is not expected that HIP would increase the

fatigue life of the vertical samples because the LOF defects may intersect the surface of the sample if the samples were HIPed after machining. Because the HIP process does not alleviate surface defects and porosity [28, 130], the fatigue life of vertically oriented specimen following machining then HIP in 4-point bend loading could be expected to decrease because the crack initiation sites would still exist and microstructural coarsening associated with HIP decreases the strength of the microstructure [8, 87, 106, 128]. However, if the samples are HIPed before machining, the HIP process is expected to be effective on both orientations for reducing porosity and increasing fatigue resistance. This demonstrates that it is imperative to HIP before machining to increase the fatigue life of EBM-fabricated Ti-6Al-4V.

4.5.2.2. Interrupted Fatigue Tests

Results of interrupted fatigue tests are provided in Figure 56. The tests revealed that the vertical specimen initiated fatigue cracks and failed earlier than the horizontal specimen.

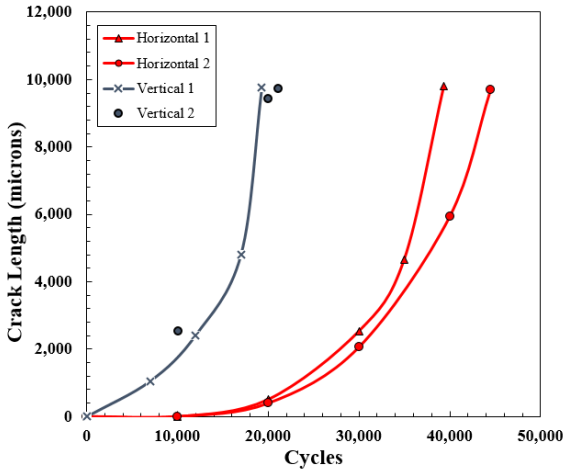

Figure 56. Measured crack length as function of fatigue cycles.

The vertical specimens were observed to have multiple cracks at cycles as low as 7,000. Cracks were not observed in horizontally-oriented specimen until cycle 20,000 and no cracks were observed at cycle 10,000. The crack growth rate (da/dN) is the slope of the fatigue cycles vs. crack length curves and steeper slopes indicate a faster growth rate. The crack growth rates at various average crack lengths were calculated numerically using the secant method outlined by Virkler [204] (see appendix for example calculations and equations) and plotted as a function of average crack length, $\bar{a}_i$ (Fig. 57).

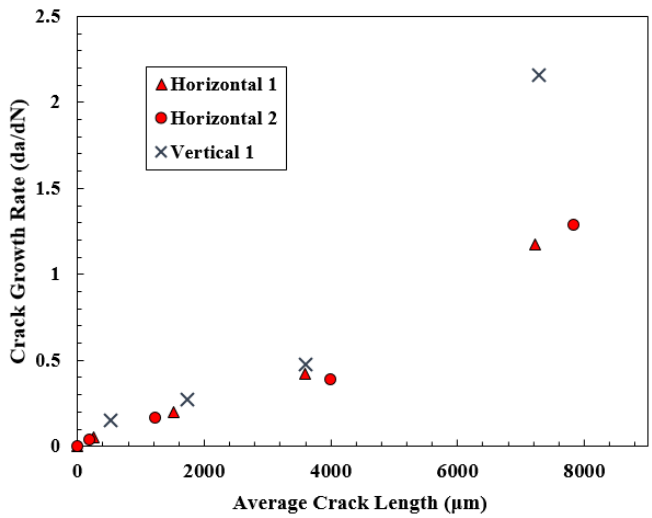

Figure 57. Crack growth rate (microns/cycle) calculated using Secant method and plotted against average crack length.

Although limited data available, upon inspection of Figure 57, it appears the crack growth rates of the vertical sample are equal to those of the horizontal specimen at a given average crack length. The final vertical data point (~7000 µm crack length, da/dN ~ 2.25 µm/cycle) is considered an outlier because the other vertical data points are similar to the horizontal

growth rates. The crack growth rate of Ti-6Al-4V was shown to be dependent on microstructure [205] and a degree of anisotropy for crack growth rates was observed in EBM fabricated Ti-6Al-4V [126] so it is possible for the crack growth rate to be dependent on build orientation, but it is not evident in this study.

It should be noted that the 'Vertical 2' specimen was left out of the da/dN calculation because the most damaging crack initiated at a LOF defect that intercepted the surface and not at a hole, as indicated in Fig. 58.

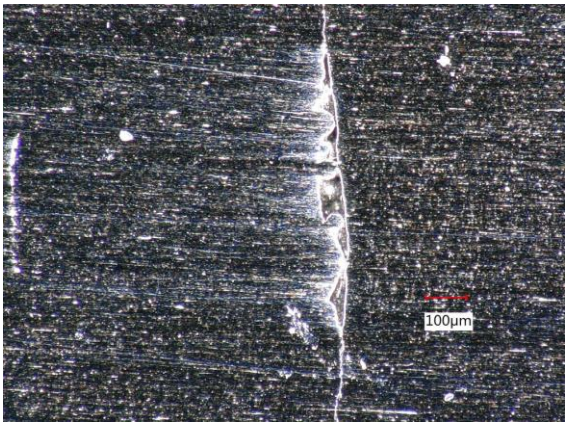

Figure 58. Crack initiating at a LOF defect intercepting the surface of a vertical specimen at 10,000 cycles.

The sample did not fail significantly earlier than 'Vertical 1', but the most damaging crack initiated by a different mechanism than the other samples. 'Vertical 1' cracks initiated at a machined hole but earlier than the horizontal samples. Multiple cracks were observed initiating at both holes in 'Vertical 1', at cycle 7,000 (Fig. 59). Many of the cracks are not symmetric with the hole and appear to be initiating from defects at the surface.

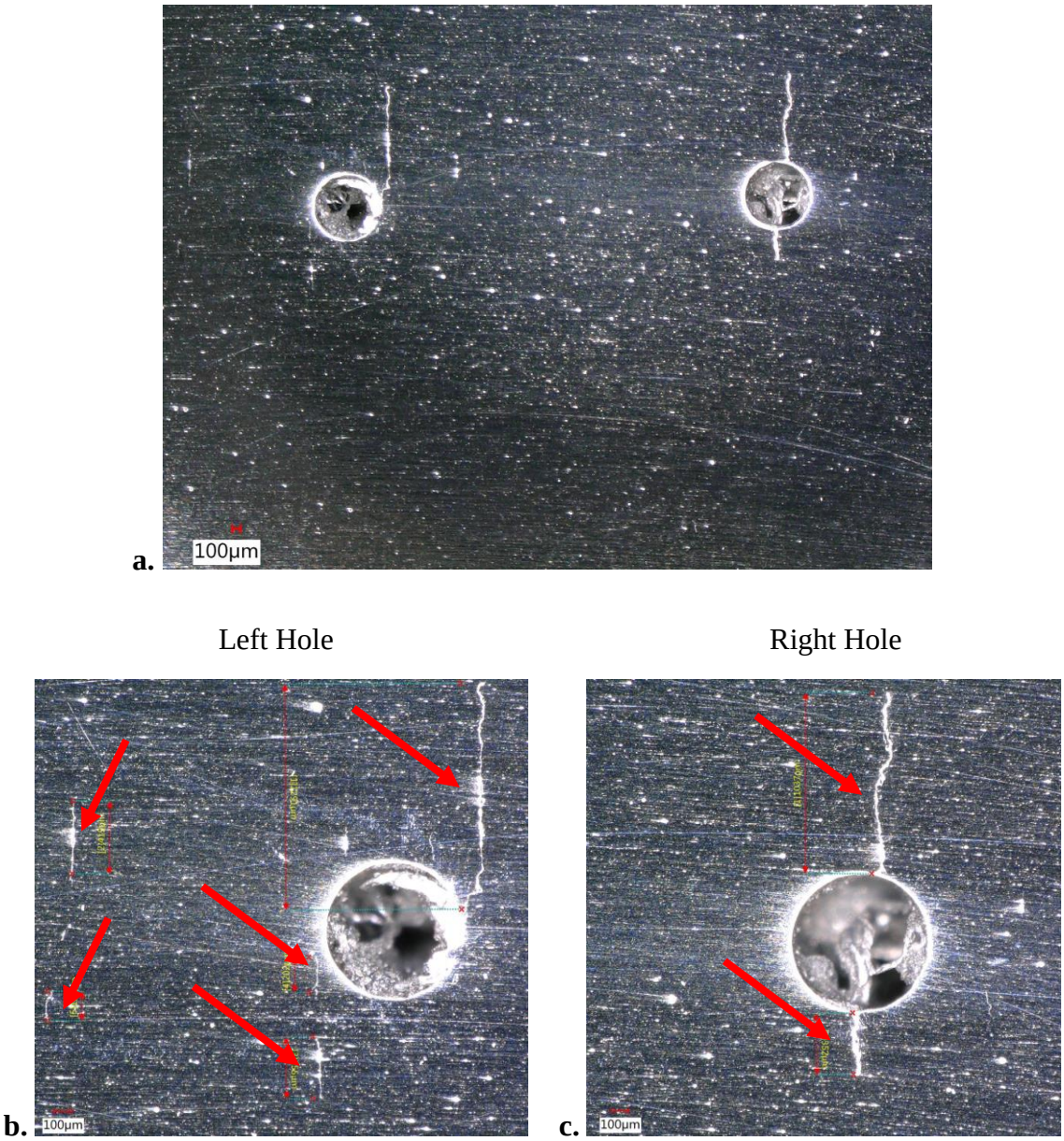

Figure 59. Interrupted fatigue test crack monitoring of specimen 'Vertical 1' showing multiple cracks initiating at both holes at cycle 7,000. The red arrows indicate independent cracks.

4.5.3. Effects of Build Geometry and Volume on Fatigue Life

It is widely reported in the literature that the wall thickness of EBM-fabricated parts has an effect on the microstructure because of different thermal inputs [77, 88, 100, 173]. In thin-walled structures, a fine microstructure with mixed α′ and α+β phases is observed and thicker walled structures display a coarser microstructure [77, 100, 173]. Fig. 60 shows the fatigue life of test bars machined from blocks with different wall thicknesses.

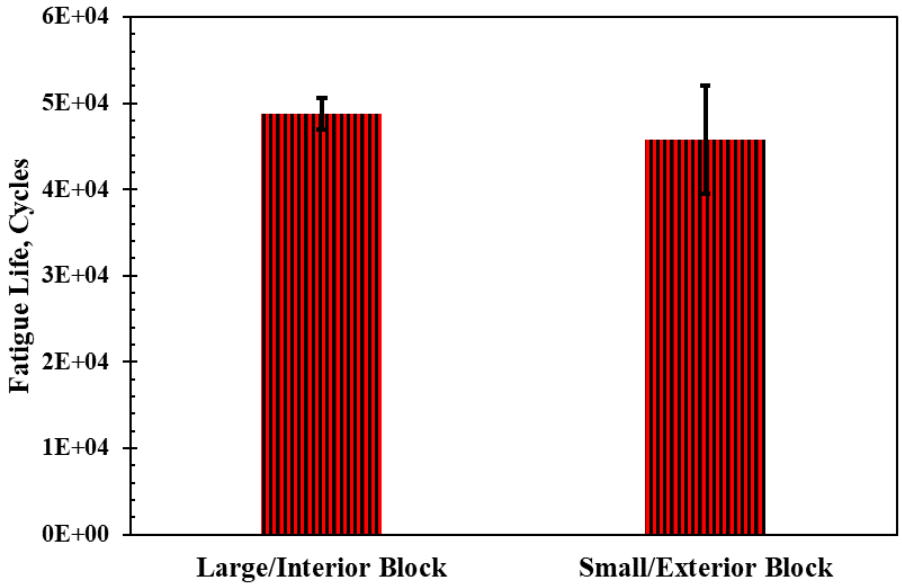

Figure 60. Fatigue cycles to failure of parts with different wall thicknesses.

The results indicate that there is no statistically significant difference between wall thickness and fatigue life in this study. The interior block displayed a higher average fatigue life, but the difference was not statistically significant ($F = 0.45$, $p = 0.532$ when $\alpha = 0.05$). However, α′ has been observed in thin walled structures in other studies and α′ has a lower fatigue damage tolerance than α+β microstructures because of its lower ductility [51]. If the wall thickness is sufficiently thin, then a difference in fatigue behavior could be

observed. The parts fabricated in this build showed similar hardness regardless of wall thickness and thus it is expected that little difference in the microstructural features was present.

4.5.4. Effects of Scan Path on Fatigue

Because additive manufacturing allows for incorporating internal fine features (such as cooling channels and fastener holes) without machining, it is important to study the effects of building internal features on fatigue life. As shown previously in section 4.5.1.2, melt pool overlap resulted in a smaller than designed hole with a rough internal surface. While traditional machining may not be possible to eliminate the rough surface in internal complex features, a process like chemical etching [105] could be used. To compare the fatigue behavior of a sample with internal features partially built by the EBM process and then post-processed to the final dimension, parts with undersized holes were reamed to final dimension ('reamed holes') and then compared to parts with machined holes ('machined holes'), shown schematically in Fig 61a. This equalizes the diameter of the hole, but a different EBM scan path was used to fabricate the parts. The cycles to failure of the reamed holes against parts with machined holes are given in Fig. 61b.

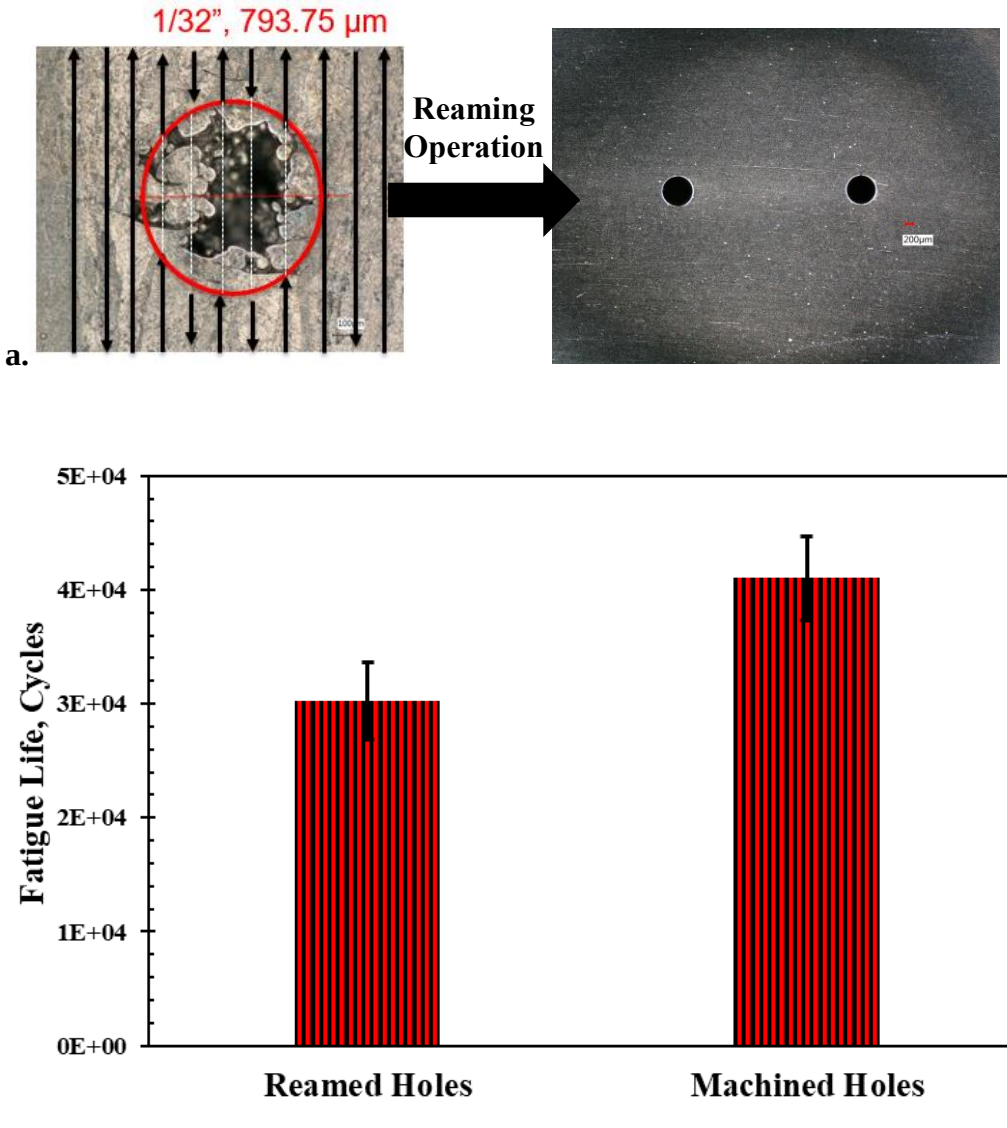

Figure 61. Schematic of machining process to obtain the 'reamed hole (a.) where black arrows indicate beam scans projected onto an as-built hole. Average cycles to failure of horizontally oriented parts machined from the center large block with either reamed or machined holes (b.). Parts tested at σ = 590 MPa.

ANOVA tests revealed a statistical significant difference at the 95% confidence interval in fatigue life between the samples with the machined holes and samples with reamed holes ($F = 9.42$ at $\alpha = 0.05$). The difference in fatigue life could have been attributed to either a change in scan path or the integrity of the hole as previously discussed in section 4.5.1.2. It was observed in literature that pores have a tendency to accumulate at the end of hatch lines and hatch turning points [116, 186]. An example is provided in Fig. 62, an X-Ray Computed Tomography (XCT) scan of a part with uni-directional hatching only. The hatch scans ended on one side of the part and porosity accumulates as the hatch lines end. Based off this observation, breaking the scan path by incorporating a small hole into the original build was expected to increase the porosity near the hole.

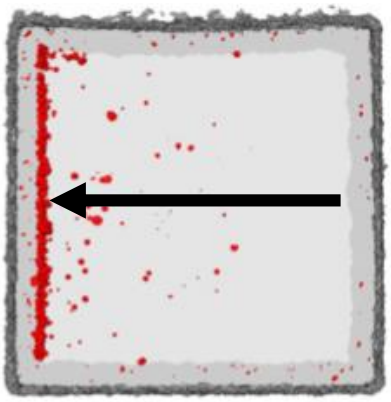

Figure 62. XCT scan projected onto an X-Y plane showing porosity distribution in a sample with unidirectional hatching (indicated by the black arrow). Figure adapted from [116].

After inspecting the fracture surfaces, it was concluded the difference in fatigue life can be attributed to the integrity of the reamed hole. SEM inspection of the fracture surface of the

sample with the reamed hole revealed the crack initiation site was not at the surface, but lack-of-fusion defects that border the bore the hole (Fig. 63). The defects are left over from the rough as-built surface and were not removed during the reaming process.

Sun and Liu [199, 200] indicated that surface roughness within the bore of a fastener hole decreases the fatigue strength. The bore of the reamed sample showed sharp cavities containing partially sintered powder particles as shown in Fig. 64. The cavities, left over from the surface roughness of the partially built hole from the EBM process, acted as stress concentrators and led to the decreased fatigue life observed in the samples with reamed holes. Despite the reaming to expand the undersized hole to the required dimension, the reaming did not sufficiently remove the rough surface left over from the EBM building process.

As previously discussed, porosity is commonly observed near turning points of hatch in fill scans [116, 186]. However, as shown in Fig. 65, pores were observed on the fracture surfaces of both samples with reamed holes and machined holes without indication that the reamed hole contained more or less porosity than the reamed hole sample. This was contrary to the hypothesis that there would be a greater amount of pores near the bore of the hole that was partially built during the EBM process as a result of the break in beam path needed to fabricate the hole.

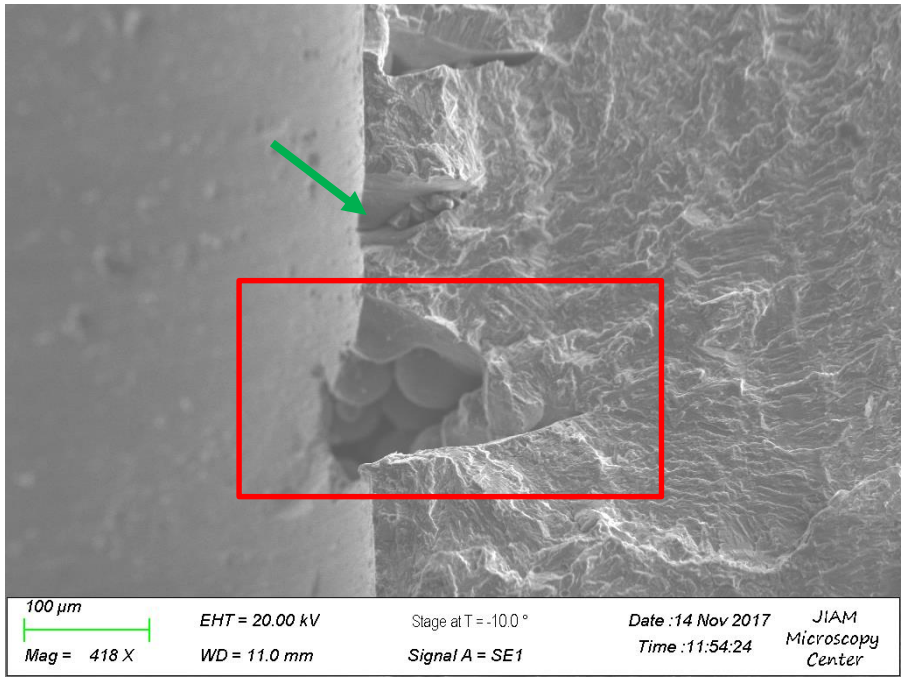

Figure 63. SEM micrograph of a fracture surface of a sample with a reamed hole. Crack initiation site is outlined in red and green arrows indicate surface defects the reaming process did not remove.

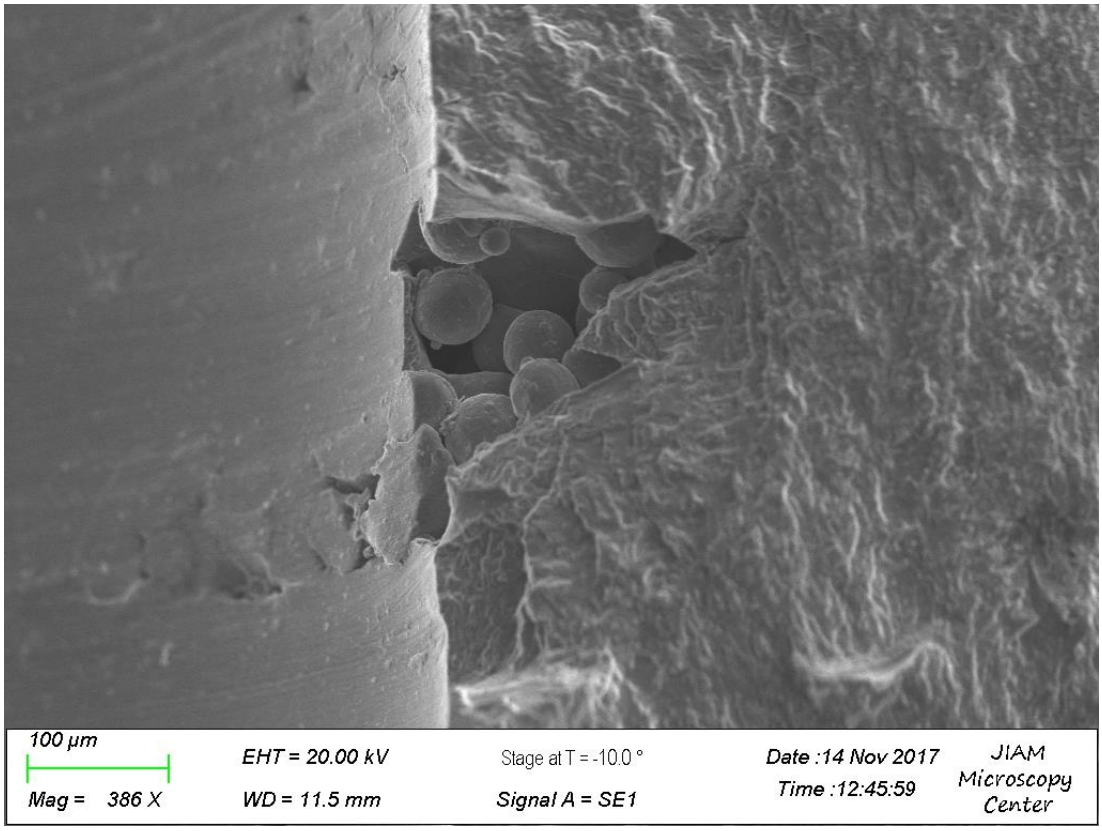

Figure 64. Sharp cavity along the bore of the sample with reamed hole remnant of the surface roughness of the as-fabricated hole.

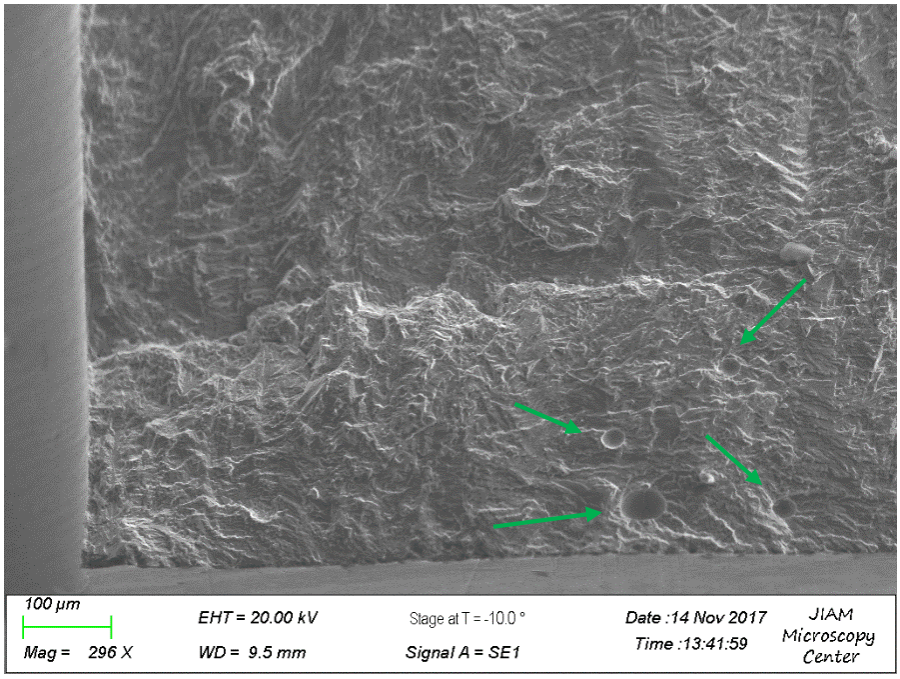

a.

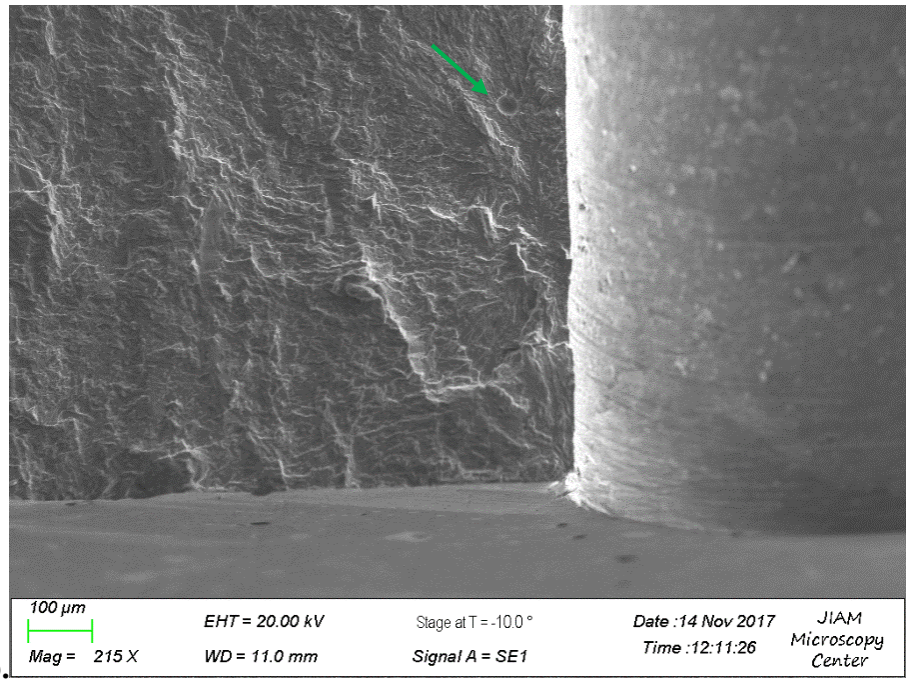

b.

Figure 65. Fracture surface images of the specimen with machined hole (a. & b.). The green arrows indicate gas pores.

4.5.5. Comparison to Conventional Ti-6Al-4V

A number of different EBM material conditions were compared to conventionally manufactured Ti-6Al-4V specimen and the results are provided in Fig. 66.

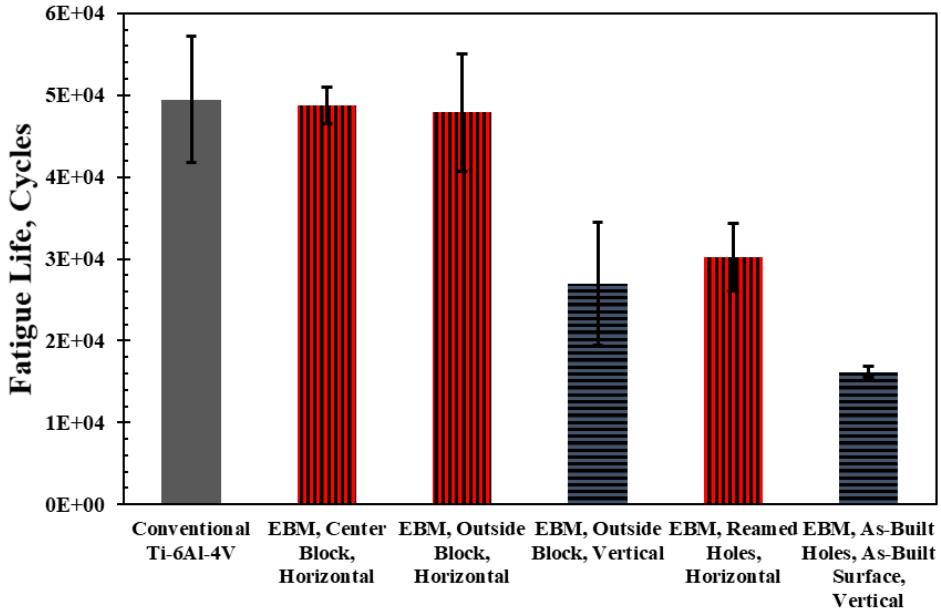

Figure 66. Fatigue resistance of EBM material (horizontal and machined) compared to conventional Ti-6Al-4V.

The horizontally-oriented EBM samples with machined holes, on average, failed in less cycles than the conventional material. However, 1-way ANOVA tests showed the difference is not statistically significant at the 95% confidence interval ($F = 2.69$, $p = 0.176$ when $\alpha = 0.05$). The slightly higher average fatigue resistance of the conventional material is most likely attributed to the pores and voids in the EBM material that were not readily observed in the conventional material, as shown in Fig. 67. Other conditions (vertically oriented, reamed holes, rough surfaces) all displayed significantly lower fatigue resistances compared to the conventionally manufactured material.

a.

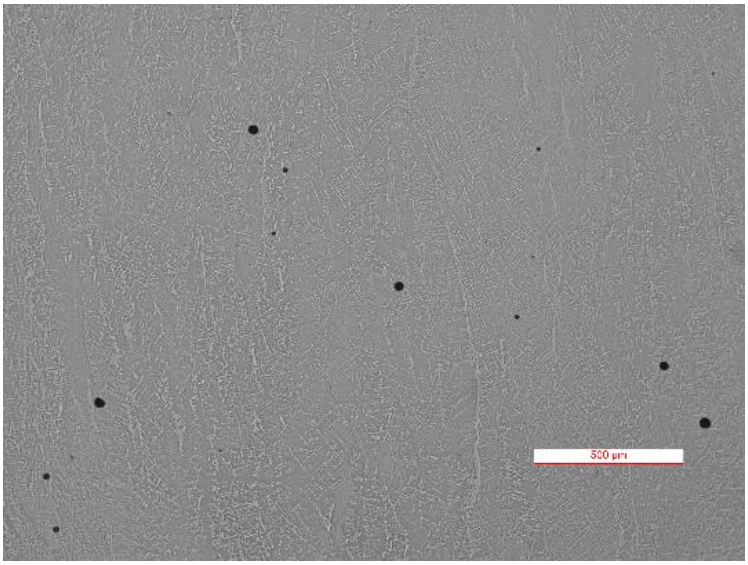

b.

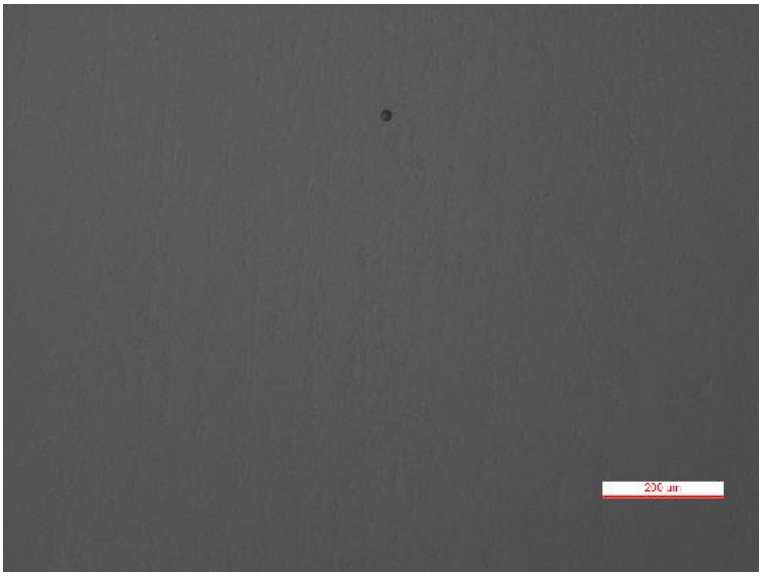

Figure 67. Example defects observed in EBM (a.) and conventional (b.) material.

The horizontal EBM and conventional samples, all with machined holes and polished and fine ground surfaces, displayed similar crack initiation sites at the machined hole. Although the fine lamellar microstructure has superior crack propagation resistance compared to other Ti-6Al-4V morphologies [206, 207] and EBM as-fabricated material was shown to have comparable crack growth behavior to cast and wrought Ti-6Al-4V regardless of defects [126], the conventional samples in this study still displayed a slightly higher average fatigue life than the EBM material. Figure 68 shows fracture surfaces of conventional (a) and a horizontally-oriented EBM (b) fatigued samples. Note that the crack initiates in both samples at the edge of the machined hole, but porosity defects are observed in the EBM material and not the conventional. Void and defect size, location, and proximity to surface has been shown to influence crack initiation [208, 209]. Thus the voids and defects in the EBM material could lead to early initiation or have little influence depending on their proximity to the machined hole in the specimen.

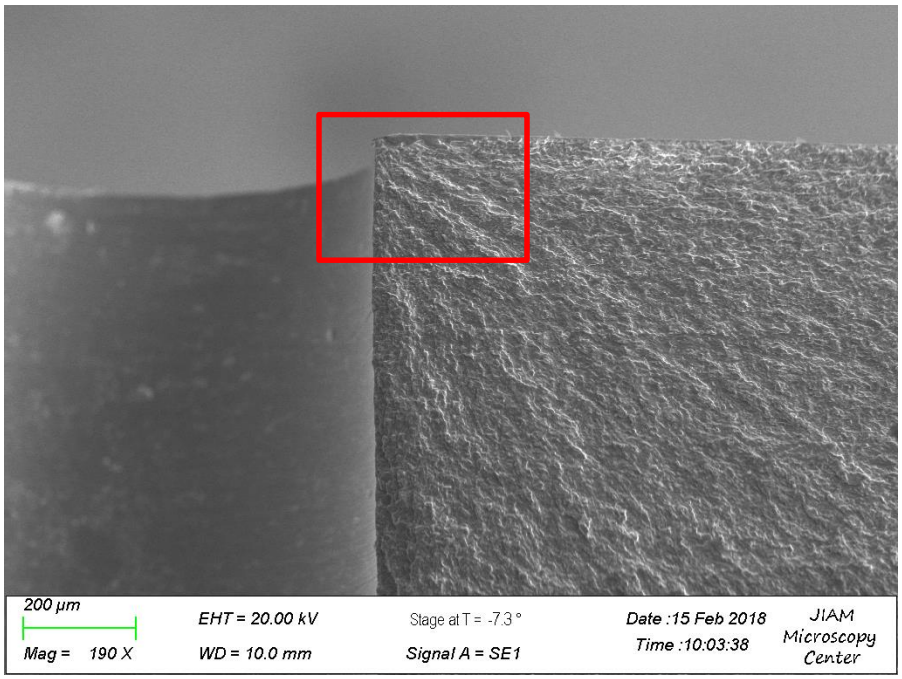

a.

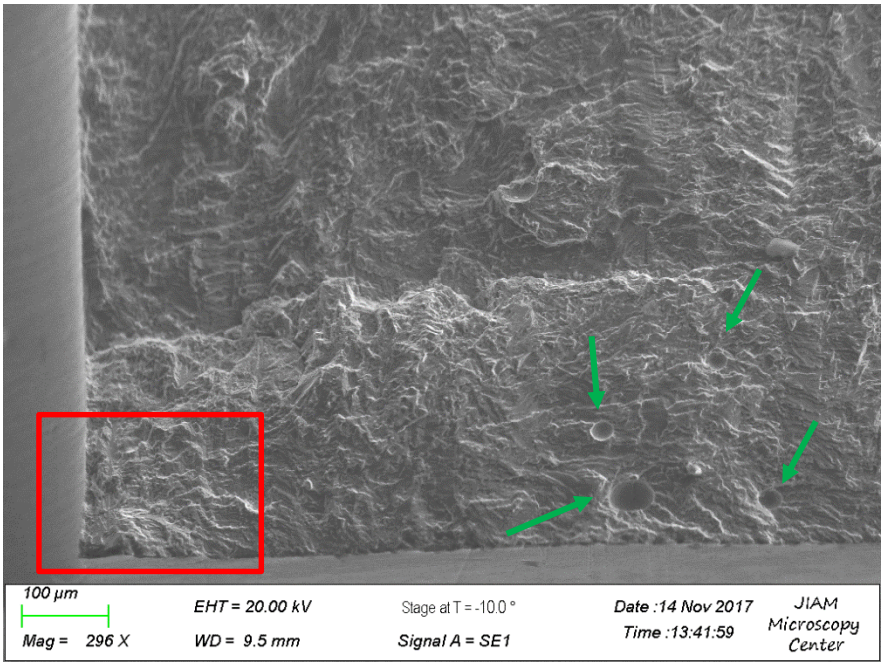

b.

Figure 68. SEM images of conventional (a.) and horizontal EBM specimen (b.). Defects are indicated by green arrows in the EBM specimen crack initiation sites by red boxes.

5. RECOMMENDED PRACTICE FOR FATIGUE APPLICATIONS

Review of the open literature and the results of this report indicate that the surface roughness and defects that are present in EBM-fabricated components limit their use for fatigue limited applications. A number of studies in literature have identified non-traditional methods, both in-situ and post-process, that could potentially increase the fatigue damage tolerance of EBM-fabricated Ti-6Al-4V components by alleviating the surface roughness and interior defects without machining nor HIP. This section will review and discuss a number of those processes and make recommendations to optimize the EBM process for best fatigue performance.

5.1. Current Recommended Best Design Practice

Currently, HIP and machining are both necessary to achieve adequate fatigue damage tolerance for aerospace applications. Some studies have shown process parameter modifications alter surface roughness [99, 112, 113, 210] and the density (porosity) [78, 87, 109, 110, 112, 116, 122] of the EBM-fabricated components, but only limited success was obtained. As a powder-bed fusion process, it may not be possible to achieve the surface roughness values one source recommended for aerospace applications, R_a = 3.2 μm [201], without post-process machining. Because the surface roughness is most detrimental to fatigue, machining is required to both eliminate the surface roughness and also hit dimensional tolerances, which can fluctuate from original design [211] (the resolution of the EBM process is 100 – 200 μm [20]). Therefore, the process should be optimized to reduce the internal porosity in an effort to eliminate the post-process HIP while planning

for post-process machining. This includes optimizing the energy input from the electron beam [109, 116] and ensuring that the scan length is always less than 100 mm for sufficient energy input [117]. Until the EBM process can be optimized to keep porosity limits below a certain size threshold as to not impact mechanical or fatigue properties [59, 212], HIP is required for fatigue applications to effectively eliminate the porosity defects and homogenize the microstructure.

Although post-process HIP and machining today are necessary for fatigue critical applications, some non-traditional methods are being discussed in the literature. The following sections outline a number of those methods. Each section is titled after a factor that must be mitigated or optimized for fatigue applications. Methods that improve the respective factor are then documented.

5.2. Surface Roughness

The surface roughness was identified as most detrimental to fatigue performance as it provides early surface crack initiation sites greatly reducing the total fatigue life. The stair-step surface and partially sintered powders is the greatest hindrance to widespread use for fatigue applications. Rather than traditional machining, laser ablation is a manufacturing process that can lessen the surface roughness of EBM-fabricated components. Laser ablation uses a high-energy laser beam to vaporize a small amount of material from the surface of a part, while an inert gas disperses the vapors and protects the surface from oxidation [213]. Laser ablation is capable of reducing the surface roughness of the EBM-manufactured Ti-6Al-4V. Optimized laser parameters were shown to reduce the surface

roughness, R_a, from 31 μm to 13 μm while only removing 180 μm of the material with no heat-affected zone [214]. In comparison, forging results in R_a values of 12.5 μm to 3.2 μm [215]. An advantage of laser ablation is that it can be controlled to selectively vaporize areas while leaving other areas with the rough surface finish if needed for biomedical applications where rougher surfaces can be advantageous for medical implant osseointegration [216]. Laser ablation is limited because it is a post-process, which adds time and costs and optimized laser parameters were shown to only produce surface-roughness values comparable to rough forgings.

A non-traditional machining method that also shows promise to reduce surface roughness is rotary ultrasonic machining (RUM). RUM is a hybrid machining process that combines ultrasonic machining and conventional diamond grinding together to produce a machined product with superior surface finish and higher material removal rate than traditional machining methods [217]. Initial literature results have shown successful rotary ultrasonic machining of Ti-6Al-4V achieving R_a values below 0.3 μm with no change in surface chemical compositions [218, 219].

As opposed to post-process methods, it may be possible to reduce the roughness by altering the layer thickness and powder feed stock diameter. The surface roughness associated with the EBM manufactured parts originates from two sources: partially melted powder adhering to the surface and the stair-step or layering effects from melt pool solidification [131]. Reducing the layer thickness and powder size can improve the roughness of the

surface. Because the maximum surface roughness is related to the deposition layer thickness, a smaller layer thickness is expected to reduce the roughness [20, 103]. The melt-pool depth must be at least twice the layer thickness to ensure layer to layer adhering [121]. A reduction in the layer thickness requires less energy input, resulting in less melt-pool overflow and partially sintered powders on the surface.

In addition to the layer thickness, the powder size influences the surface roughness. During melting, partially-sintered powders can adhere to the outside surface of the build on what are often referred to as 'satellites' [20]. Smaller powders can improve the surface roughness by reducing the size of the satellites [20, 90]. In general, EBM has higher surface-roughness values, compared to laser AM systems because of the increase in powder size [20] (the EBM as-built surfaces have average roughness values of 30 - 50 μm [220]). Powder sizes for EBM systems are typically 45 - 106 μm, compared to laser AM powders, which are typically 10 - 45 μm [221]. The EBM technology requires powder with a larger diameter because of the powder smoking issues, the sudden uncontrolled spread of powder by electrostatic forces. Despite powder smoking issues, Karlsson et al. conducted successful builds on an EBM system using powder sized 25 - 45 μm. There was no significant improvement in surface roughness values but the process was not optimized for the smaller powder size [222].

There are a number of limitations to consider when reducing powder sizes and layer thickness. The first is the increased build time. Reduced layer sizes require more layers to

be melted for an equivalent part geometry. Software limitations do not permit layer-thickness reductions in fatigue-critical areas and the typical layer thickness of 50 μm for the remaining bulk of the part.

Reducing the powder size presents issues with build times in addition to other limitations. Smaller powders are more susceptible to powder smoke. Coarse powders are generally more resistant to powder smoking than fine powders, but higher powder bed temperatures and faster beam speeds can prevent powder smoking of smaller powders [222, 223]. The higher bed temperatures sinter more powder, allowing for a path to ground, and the faster beam speeds put less electrons into the build, lowering the negative charge build up on free powders. The fine powders, however, are also known to destabilize the vacuum [67].

5.3. Porosity

Literature and the results of this report have shown that closing the porosity is vital for fatigue applications. Although there is a significant improvement following machining, the EBM-fabricated parts still display lower average fatigue life than conventionally manufactured parts due to the interior pores, the presence of which can be reduced with increasing beam energy input. A possible method to increase the energy input without altering other machine settings is to increase the number of melt cycles. Morton et al. [224] studied the fatigue life of ‘L’-shaped brackets using different melt-cycle strategies to grade the microstructure. Selectively-melting the fatigue-critical corner area of the ‘L’ bracket to grade the microstructure with a second melt cycle gave a 22% increase in cycles to failure despite a 50% increase in the α lath size from the as-fabricated condition without machining

nor HIP [224]. It is expected that the increase in the fatigue life is attributed to the porosity closure in the graded area. In addition, an entire 'L'-shaped bracket underwent 3 melt cycles and showed a 208% increase in the fatigue resistance, compared to as-fabricated bracket despite a 142% in the α lath size. The fatigue life of the triple-melted part was comparable to the reference wrought bracket, but had to be machined to final dimensions because the part lost geometric specifications from the increased energy input and over melting [224]. The results serve as an example of how altering the machine process settings can increase the fatigue-damage tolerance by closing porosity without the need for post-process HIP.

5.4. Microstructure

Although the fine lamellar microstructure that is observed in EBM fabricated parts shows sufficient fatigue damage tolerance, an advantage that should be exploited in AM is the ability to control the energy input and control the microstructural features. By altering the energy input via scan strategies during the build, it is possible to control the microstructural evolution. This has been proven successful in controlling the crystallographic orientation of Inconel 718 by altering the electron beam current and scan velocity [225]. It has been widely observed that the columnar β grains are highly textured in the $\langle 001 \rangle$ direction [75, 87, 101]. In addition, there exists a texture of the α phase as a result of the preferential growth of the columnar β grains and the ensuing martensitic transformation upon rapid cooling [76]. In Ti-6Al-4V, the martensitic transformation obeys the Burgers orientation relationship (OR): $(0001)_{\alpha} \parallel \{110\}_{\beta}$ and $\{11\bar{2}0\}_{\alpha'} \parallel \langle \bar{1}11 \rangle_{\beta}$. This OR causes the $\langle 0001 \rangle$ of the α phase to be oriented 45° or 90° to the $\langle 001 \rangle$ direction of the β phase (parallel to the

build direction), resulting in the possible anisotropy in the mechanical properties [76]. The microstructural texture is defined as the crystallographic condition where a local region of adjacent grains has nearly the same orientation and slip characteristics as a single grain [59]. In these regions for Ti-6Al-4V, most of the α grains display the same crystallographic orientation, are referred to as 'macrozones' or 'macrograins' in the literature, and can be 100x greater than an individual α grain size [60]. Fatigue cracks in Ti-6Al-4V initiate on basal or prismatic planes of α [34, 60]. Texture can accelerate fatigue-crack initiation if the group of grains is oriented for easy slip [59]. On the contrary, the HCF life will increase if the texture is orientated with a limited number of prismatic or lying near the direction of the critical resolved shear stress [58] or if the critical resolved shear stress is perpendicular to basal planes [62, 226]. Texture can also limit the effectiveness of grain boundaries at stopping short crack growth [67]. High-angle grain boundaries are effective barriers to crack growth when none of the active slip systems are closely oriented [58, 227], but if a small crack encounters an α colony with a common basal plane, crack propagation continues with little resistance [228]. As the microstructure becomes more textured, the effective slip distance can exceed that of the actual colony sizes. Weaker textures that have an increased number of high-angle grain boundaries are preferred for fatigue performance [34]. If the build is oriented such that the resulting textured microstructure is oriented for easy slip, the fatigue performance will be greatly reduced. However, the opposite can occur if the microstructure is textured in an orientation for unfavorable slip. Thus, controlling crystallographic orientation in probable crack initiation areas could allow for better crack initiation resistance and increase the fatigue life of as-fabricated parts. Design and build of

parts that take advantage of the mechanical anisotropy inherited from the columnar grain growth and martensitic transformation could be utilized to increase fatigue resistance.

By altering the local heat input, it is possible to control the cooling rate and microstructural features. A fast scan produces a microstructure with refined α laths and prior β grains [86], while a slow scan speed would yield a coarsened microstructure. With this strategy, it would be possible to grade the microstructure of Ti-6Al-4V parts from fine grains near the surface to coarse grains in the bulk of the material. This process would optimize the microstructure for fatigue applications with a fine-grained microstructure near crack-initiation sites transitioning to a coarse lamellar microstructure to slow long crack growth. In general, coarse lamellar microstructures have low crack-propagation rates because of the increased crack-path tortuosity and bifurcation [46, 129, 207], and a fine-grained material displays better fatigue crack initiation because the grain boundaries stunt small crack growth [34, 59, 229]. Similar methods of grading the microstructure have been tried in friction stir welded (FSW) Ti-6Al-4V [230, 231], though with EBM, the microstructural gradient could not be as steep as seen in the FSW samples. As previously seen in this manuscript, closing the porosity through HIP and eliminating the rough surface by machining often increases the fatigue resistance of EBM-manufactured Ti-6Al-4V parts to levels comparable to superior than conventional Ti-6Al-4V material. If combined with a graded microstructure, the fatigue-damage tolerance could be maximized by manufacturing with EBM. However, it would be advantageous to achieve the same fatigue resistance while eliminating a post-process.

6. CONCLUSIONS

The fatigue behavior of Ti-6Al-4V fabricated by electron beam melting was extensively studied. The literature review demonstrated that the fatigue resistance of EBM components can be comparable to those with conventional microstructures after post-processing. However, surface roughness and interior porosity defects inherited by the EBM fabrication limit the fatigue strength if not removed or mitigated by machining and HIP process. The literature reviews also demonstrated the need to link EBM process conditions and variables to fatigue behavior to realize EBM's full potential and widespread use in the aerospace industry.

This study identified the build orientation, build volume, scan path, and surface finish as important EBM process parameters to vary and study the resulting fatigue behavior and mechanical properties. Microstructure, tensile strength, Vickers Hardness, and 4-point bend fatigue results were obtained and analyzed. The conclusions are summarized in the following statements.

- In contrast to other studies, no significant effects on Vickers hardness or microstructure was observed as a function of wall thickness or distance from build plate.
- The tensile strength (YS and UTS) were similar for both horizontal and vertical orientations but the vertically-oriented specimen showed a superior ductility due to an increased amount of grain boundaries in the vertical specimen.

- Surface roughness, both in the bore of a fastener-hole or internal cooling feature and outside surface, significantly reduced the fatigue life. It is recommended to remove a depth of at least 725 μm (0.0285”) of material to remove all surface roughness effects.
- An orientation dependence was observed in 4-poind bend fatigue tests where the horizontal specimen showed a statistically significant superior fatigue life after machining and polishing. Interrupted fatigue test crack monitoring and SEM fractography revealed multiple surface crack initiation sites from LOF and inter-layer defects near the surface of vertical specimen.
- Fastener holes or internal cooling channels in EBM parts must be sufficiently machined to rid the surface of all defects left from the EBM fabrication to avoid a reduction in fatigue life.
- EBM fabricated Ti-6Al-4V components can have comparable fatigue life to conventional counterparts, but have a slightly lower average cycles to failure because of the interior porosity.
- The combination of HIP and machining is today the most effective way to increase the fatigue damage tolerance, but there are methods, both in-situ and post-process, currently being studied that could increase the fatigue resistance without traditional machining and HIP. Optimizing the beam energy input to eliminate porosity and melt defects to potentially replace post-process HIP followed by machining is the most promising route.

This study has shown that EBM process conditions affect the fatigue behavior during 4-point bend loading. However, the results are encouraging for future research and applications of EBM, even for flight critical components, because the parts exhibited very good mechanical properties. With further research and deeper understanding of the process, EBM-fabricated Ti-6Al-4V has a promising future in the aerospace industry.

LIST OF REFERENCES

1. Zhang, J.-k., X.-q. Cheng, and Z.-n. Li, *Total fatigue life prediction for Ti-alloys airframe structure based on durability and damage-tolerant design concept.* Materials & Design, 2010. **31**(9): p. 4329-4335.
2. Welsch, G., R. Boyer, and E. Collings, *Materials properties handbook: titanium alloys*. 1993: ASM international.
3. Donachie, M.J., *Titanium: A Technical Guide* 2nd ed. 2000, Materials Park, OH, USA: ASM International. .
4. Malinov, S., et al., *Differential scanning calorimetry study and computer modeling of $\beta \Rightarrow \alpha$ phase transformation in a Ti-6Al-4V alloy.* Metallurgical and Materials Transactions A, 2001. **32**(4): p. 879-887.
5. Leyens, C. and P. M., *Titanium and Titanium Alloys: Fundamentals and Applications*. 2005, Weinheim: Wiley-VCH.
6. Lütjering, G. and J.C. Williams, *Titanium*. 2007: Springer Science & Business Media.
7. Elmer, J., et al., *Phase transformation dynamics during welding of Ti–6Al–4V.* Journal of applied physics, 2004. **95**(12): p. 8327-8339.
8. Lu, S., et al., *Microstructure and mechanical properties of long Ti-6Al-4V rods additively manufactured by selective electron beam melting out of a deep powder bed and the effect of subsequent hot isostatic pressing.* Metallurgical and Materials Transactions A, 2015. **46**(9): p. 3824-3834.
9. Safdar, A., et al., *Evaluation of microstructural development in electron beam melted Ti-6Al-4V.* Materials Characterization, 2012. **65**: p. 8-15.
10. Tan, X., et al., *Graded microstructure and mechanical properties of additive manufactured Ti–6Al–4V via electron beam melting.* Acta Materialia, 2015. **97**: p. 1-16.
11. Sanders, D. *Titanium Manufacturing Processes and Alloy Selection for Aerospace Applications* in *International Titanium Association Conference* 2012. Atlanta, GA.
12. Veiga, C., J. Davim, and A. Loureiro, *Review on machinability of titanium alloys: the process perspective.* Rev. Adv. Mater. Sci, 2013. **34**: p. 148-164.
13. Sacristan, I., et al., *Influence of oxygen content on the machinability of Ti-6Al-4V alloy.* The International Journal of Advanced Manufacturing Technology, 2016. **86**(9-12): p. 2989-3005.
14. Cantero, J., et al., *Dry drilling of alloy Ti–6Al–4V.* International Journal of Machine Tools and Manufacture, 2005. **45**(11): p. 1246-1255.
15. Hoyne, A.C., C. Nath, and S.G. Kapoor, *On cutting temperature measurement during titanium machining with an atomization-based cutting fluid spray system.* Journal of Manufacturing Science and Engineering, 2015. **137**(2): p. 024502.
16. Ezugwu, E. and Z. Wang, *Titanium alloys and their machinability—a review.* Journal of materials processing technology, 1997. **68**(3): p. 262-274.
17. Hall, J., *AIRCRAFT ACCIDENT REPORT: Uncontained Engine Failure DELTA AIR LINES Flight 1288 MCDONNELL DOUGLAS MD-88.* Washington, DC, 1996. **20594**.

18. Atzeni, E. and A. Salmi, *Economics of additive manufacturing for end-usable metal parts.* The International Journal of Advanced Manufacturing Technology, 2012. **62**(9): p. 1147-1155.
19. Liang, W., et al., *Electrical discharge machining of electron beam melting formed shrouded blisk.* The International Journal of Advanced Manufacturing Technology, 2016. **87**(5-8): p. 2319-2326.
20. Sames, W.J., et al., *The metallurgy and processing science of metal additive manufacturing.* International Materials Reviews, 2016. **61**(5): p. 315-360.
21. Arcam-AB, *Arcam History.* 2017.
22. Hiemenz, J., *Electron beam melting.* Advanced materials & processes, 2007. **165**(3): p. 45-46.
23. Keist, J.S. and T.A. Palmer, *Development of strength-hardness relationships in additively manufactured titanium alloys.* Materials Science and Engineering: A, 2017. **693**: p. 214-224.
24. Ibrahim, R.A., *Handbook of Structural Life Assessment*. 2017, Hobeken, NJ: John Wiley and Sons.
25. Campbell, F.C., *Elements of metallurgy and engineering alloys*. 2008: ASM International.
26. Cowles, B., *High cycle fatigue in aircraft gas turbines—an industry perspective.* International Journal of Fracture, 1996. **80**(2-3): p. 147-163.
27. Bache, M. and W. Evans, *Impact of texture on mechanical properties in an advanced titanium alloy.* Materials Science and Engineering: A, 2001. **319**: p. 409-414.
28. Yadollahi, A. and N. Shamsaei, *Additive manufacturing of fatigue resistant materials: Challenges and opportunities.* International Journal of Fatigue, 2017. **98**: p. 14-31.
29. Åkerfeldt, P., R. Pederson, and M.-L. Antti, *A fractographic study exploring the relationship between the low cycle fatigue and metallurgical properties of laser metal wire deposited Ti–6Al–4V.* International Journal of Fatigue, 2016. **87**: p. 245-256.
30. Bridier, F. 2006, University of Poitiers
31. Bowden, D.M. and W.H. Peter, *Near-net shape fabrication using low-cost titanium alloy powders*. 2012, The Boeing Company.
32. Li, P., et al., *Critical assessment of the fatigue performance of additively manufactured Ti–6Al–4V and perspective for future research.* International Journal of Fatigue, 2016. **85**: p. 130-143.
33. Seifi, M., et al., *Overview of materials qualification needs for metal additive manufacturing.* JoM, 2016. **68**(3): p. 747-764.
34. Hall, J., *Fatigue crack initiation in alpha-beta titanium alloys.* International journal of fatigue, 1997. **19**(93): p. 23-37.
35. Callister, W.D. and D.G. Rethwisch, *Fundamentals of materials science and engineering*. Vol. 471660817. 2000: Wiley London.
36. Zarkades, A. and F. Larson, *The Science, Technology and Application of Titanium (ed. RI Jaffee and NE Promisel) 933*. 1970, Pergamon, Oxford.

37. Buirette, C., et al., *Study of crack propagation mechanisms during Charpy impact toughness tests on both equiaxed and lamellar microstructures of Ti–6Al–4V titanium alloy.* Materials Science and Engineering: A, 2014. **618**: p. 546-557.
38. Swarnakar, A.K., O. Van der Biest, and B. Baufeld, *Thermal expansion and lattice parameters of shaped metal deposited Ti–6Al–4V.* Journal of Alloys and Compounds, 2011. **509**(6): p. 2723-2728.
39. Newkirk, J. and A. Geisler, *Crystallographic aspects of the beta to alpha transformation in titanium.* Acta Metallurgica, 1953. **1**(3): p. 370373-371374.
40. Porter, D.A., K.E. Easterling, and M. Sherif, *Phase Transformations in Metals and Alloys, (Revised Reprint)*. 2009: CRC press.
41. Pilchak, A., R. Williams, and J. Williams, *Crystallography of fatigue crack initiation and growth in fully lamellar Ti-6Al-4V.* Metallurgical and Materials Transactions A, 2010. **41**(1): p. 106.
42. Ahmed, T. and H. Rack, *Phase transformations during cooling in α+ β titanium alloys.* Materials Science and Engineering: A, 1998. **243**(1): p. 206-211.
43. Mur, F.G., D. Rodriguez, and J. Planell, *Influence of tempering temperature and time on the α'-Ti-6Al-4V martensite.* Journal of alloys and compounds, 1996. **234**(2): p. 287-289.
44. Imam, M. and C. Gilmore, *Fatigue and microstructural properties of quenched Ti-6Al-4V.* Metallurgical and Materials Transactions A, 1983. **14**(1): p. 233-240.
45. Jovanović, M., et al., *The effect of annealing temperatures and cooling rates on microstructure and mechanical properties of investment cast Ti–6Al–4V alloy.* Materials & design, 2006. **27**(3): p. 192-199.
46. Matsumoto, H., et al., *Room-temperature ductility of Ti–6Al–4V alloy with α' martensite microstructure.* Materials Science and Engineering: A, 2011. **528**(3): p. 1512-1520.
47. Shi, R., *Variant selection during alpha precipitation in titanium alloys: A simulation study*. 2014: The Ohio State University.
48. Benedetti, M. and V. Fontanari, *The effect of bi-modal and lamellar microstructures of Ti-6Al-4V on the behaviour of fatigue cracks emanating from edge-notches.* Fatigue & fracture of engineering materials & structures, 2004. **27**(11): p. 1073-1089.
49. Roder, O., et al. *Influence of Simulated Foreign Object Damage on the High Cycle Fatigue of a Ti-6Al-4V Alloy for Gas Turbine Blades*. in *Proceedings of the Fourth National Turbine Engine High Cycle Fatigue (HCF) Conference*. 1999. Universal Technology Corp., Dayton, OH, CD-Rom.
50. Oliveira, V., et al., *Preparation and characterization of Ti-Al-Nb alloys for orthopedic implants.* Brazilian Journal of Chemical Engineering, 1998. **15**(4): p. 326-333.
51. Fan, Y., et al., *Relationships among the microstructure, mechanical properties, and fatigue behavior in thin Ti6Al4V.* Advances in Materials Science and Engineering, 2016. **2016**.

52. Yoder, G., L. Cooley, and T. Crooker, *Observations on microstructurally sensitive fatigue crack growth in a Widmanstätten Ti-6Al-4V alloy.* Metallurgical and Materials Transactions A, 1977. **8**(11): p. 1737-1743.
53. Nalla, R., et al., *Influence of microstructure on high-cycle fatigue of Ti-6Al-4V: bimodal vs. lamellar structures.* Metallurgical and Materials Transactions A, 2002. **33**(3): p. 899-918.
54. Ivanova, S.G., R.R. Biederman, and R.D. Sisson, *Investigation of fatigue crack initiation in Ti-6Al-4V during tensile-tensile fatigue.* Journal of materials engineering and performance, 2002. **11**(2): p. 226-231.
55. Wu, G., et al., *Effect of microstructure on the fatigue properties of Ti–6Al–4V titanium alloys.* Materials & Design, 2013. **46**: p. 668-674.
56. Bridier, F., P. Villechaise, and J. Mendez, *Slip and fatigue crack formation processes in an α/β titanium alloy in relation to crystallographic texture on different scales.* Acta Materialia, 2008. **56**(15): p. 3951-3962.
57. Ding, R., Z. Guo, and A. Wilson, *Microstructural evolution of a Ti–6Al–4V alloy during thermomechanical processing.* Materials Science and Engineering: A, 2002. **327**(2): p. 233-245.
58. Oberwinkler, B., A. Lettner, and W. Eichlseder, *Multiscale fatigue crack observations on Ti–6Al–4V.* International Journal of Fatigue, 2011. **33**(5): p. 710-718.
59. Chan, K.S., *Roles of microstructure in fatigue crack initiation.* International Journal of Fatigue, 2010. **32**(9): p. 1428-1447.
60. Le Biavant, K., S. Pommier, and C. Prioul, *Local texture and fatigue crack initiation in a Ti-6Al-4V titanium alloy.* Fatigue & Fracture of Engineering Materials & Structures, 2002. **25**(6): p. 527-545.
61. Knobbe, H., et al., *Initiation and propagation of short fatigue cracks in forged Ti6Al4V.* Procedia Engineering, 2010. **2**(1): p. 931-940.
62. Bache, M., *Processing titanium alloys for optimum fatigue performance.* International Journal of Fatigue, 1999. **21**: p. S105-S111.
63. Bache, M., et al., *The effects of texture in titanium alloys for engineering components under fatigue.* International journal of fatigue, 2001. **23**: p. 153-159.
64. Bache, M., W. Evans, and M. McElhone, *The effects of environment and internal oxygen on fatigue crack propagation in Ti-6Al-4V.* Materials Science and Engineering: A, 1997. **234**: p. 918-922.
65. Merson, E., R. Brydson, and A. Brown. *The effect of crystallographic orientation on the mechanical properties of titanium*. in *Journal of Physics: Conference Series*. 2008. IOP Publishing.
66. Ohldin, P. *Series production of CE-certified orthopedic implants with integrated porous structures for improved bone ingrowth*. in *Proceedings of the 21st International DAAAM Symposium*. 2010.
67. Ramakrishnaiah, R., et al., *Preliminary fabrication and characterization of electron beam melted Ti–6Al–4V customized dental implant.* Saudi journal of biological sciences, 2017. **24**(4): p. 787-796.

68. Suska, F., et al., *Electron beam melting manufacturing technology for individually manufactured jaw prosthesis: a case report.* Journal of Oral and Maxillofacial Surgery, 2016. **74**(8): p. 1706. e1-1706. e15.
69. Dehoff, R.R., et al., *Case study: additive manufacturing of aerospace brackets.* Advanced Materials and Processes, 2013. **171**(3).
70. Rawal, S., J. Brantley, and N. Karabudak. *Additive manufacturing of Ti-6Al-4V alloy components for spacecraft applications*. in *Recent Advances in Space Technologies (RAST), 2013 6th International Conference on*. 2013. IEEE.
71. Molitch-Hou, M. *Rolls-Royce Flies Largest 3D Printed Part Ever Flown*. 2015; Available from: 3dprintingindustry.com.
72. Saunders, S. *GE Aviation Is Using Additive Manufacturing to Change How Aircraft Engines Are Manufactured*. 2017; Available from: 3DPrint.com.
73. Riedlbauer, D., et al., *Macroscopic simulation and experimental measurement of melt pool characteristics in selective electron beam melting of Ti-6Al-4V.* The International Journal of Advanced Manufacturing Technology, 2017. **88**(5-8): p. 1309-1317.
74. Froes, F.H., *Titanium* 2015: ASM International.
75. Al-Bermani, S.S., et al., *The Origin of Microstructural Diversity, Texture, and Mechanical Properties in Electron Beam Melted Ti-6Al-4V.* Metallurgical and Materials Transactions A, 2010. **41**(13): p. 3422-3434.
76. Shui, X., et al., *Effects of post-processing on cyclic fatigue response of a titanium alloy additively manufactured by electron beam melting.* Materials Science and Engineering: A, 2017. **680**: p. 239-248.
77. Kok, Y., et al., *Geometry dependence of microstructure and microhardness for selective electron beam-melted Ti–6Al–4V parts.* Virtual and Physical Prototyping, 2016. **11**(3): p. 183-191.
78. Gong, X., et al., *Beam speed effects on Ti–6Al–4V microstructures in electron beam additive manufacturing.* Journal of Materials Research, 2014. **29**(17): p. 1951-1959.
79. Galarraga, H., et al., *Effects of heat treatments on microstructure and properties of Ti-6Al-4V ELI alloy fabricated by electron beam melting (EBM).* Materials Science and Engineering: A, 2017. **685**: p. 417-428.
80. Rafi, H., et al., *Microstructures and mechanical properties of Ti6Al4V parts fabricated by selective laser melting and electron beam melting.* Journal of materials engineering and performance, 2013. **22**(12): p. 3872-3883.
81. Esaka, H., et al., *Growth direction of cellular and dendritic interface in a constrained growth condition.* Materials Transactions, 2002. **43**(6): p. 1312-1317.
82. Lewandowski, J.J. and M. Seifi, *Metal additive manufacturing: a review of mechanical properties.* Annual Review of Materials Research, 2016. **46**: p. 151-186.
83. Ackelid, U. and M. Svensson. *Additive manufacturing of dense metal parts by electron beam melting*. in *Proceedings of the Materials Science and Technology Conference, Pittsburgh, PA, USA*. 2009.

84. Rafi, H.K., et al. *Mechanical property evaluation of Ti-6Al-4V parts made using electron beam melting*. in *Proceedings of the Solid Freeform Fabrication Symposium*. 2012.
85. Edwards, P., A. O'Conner, and M. Ramulu, *Electron beam additive manufacturing of titanium components: properties and performance.* Journal of Manufacturing Science and Engineering, 2013. **135**(6): p. 061016.
86. Hrabe, N. and T. Quinn, *Effects of processing on microstructure and mechanical properties of a titanium alloy (Ti–6Al–4V) fabricated using electron beam melting (EBM), Part 2: Energy input, orientation, and location.* Materials Science and Engineering: A, 2013. **573**: p. 271-277.
87. Cunningham, R., et al., *Evaluating the effect of processing parameters on porosity in electron beam melted Ti-6Al-4V via synchrotron X-ray microtomography.* JOM, 2016. **68**(3): p. 765-771.
88. Wang, P., et al., *Spatial and geometrical-based characterization of microstructure and microhardness for an electron beam melted Ti–6Al–4V component.* Materials & Design, 2016. **95**: p. 287-295.
89. Guo, C., W. Ge, and F. Lin, *Effects of scanning parameters on material deposition during Electron Beam Selective Melting of Ti-6Al-4V powder.* Journal of Materials Processing Technology, 2015. **217**: p. 148-157.
90. Hrabe, N., T. Gnäupel-Herold, and T. Quinn, *Fatigue properties of a titanium alloy (Ti–6Al–4V) fabricated via electron beam melting (EBM): Effects of internal defects and residual stress.* International Journal of Fatigue, 2017. **94**: p. 202-210.
91. Galarraga, H., et al., *Effects of the microstructure and porosity on properties of Ti-6Al-4V ELI alloy fabricated by electron beam melting (EBM).* Additive Manufacturing, 2016. **10**: p. 47-57.
92. Zäh, M.F. and S. Lutzmann, *Modelling and simulation of electron beam melting.* Production Engineering, 2010. **4**(1): p. 15-23.
93. Kahnert, M., S. Lutzmann, and M. Zaeh. *Layer formations in electron beam sintering*. in *Solid freeform fabrication symposium*. 2007.
94. Petrovic, V. and R. Niñerola, *Powder recyclability in electron beam melting for aeronautical use.* Aircraft Engineering and Aerospace Technology: An International Journal, 2015. **87**(2): p. 147-155.
95. Nandwana, P., et al., *Recyclability study on Inconel 718 and Ti-6Al-4V powders for use in electron beam melting.* Metallurgical and Materials Transactions B, 2016. **47**(1): p. 754-762.
96. Tang, H., et al., *Effect of powder reuse times on additive manufacturing of Ti-6Al-4V by selective electron beam melting.* Jom, 2015. **67**(3): p. 555-563.
97. F2924-14, A., *Standard Specification for Additive Manufacturing Titanium-6 Aluminum-4 Vanadium with Powder Bed Fusion*. 2013, ASTM International: West Conshohocken, PA.
98. Yan, M., et al., *Review of effect of oxygen on room temperature ductility of titanium and titanium alloys.* Powder metallurgy, 2014. **57**(4): p. 251-257.

99. Safdar, A., et al., *Effect of process parameters settings and thickness on surface roughness of EBM produced Ti-6Al-4V.* Rapid Prototyping Journal, 2012. **18**(5): p. 401-408.
100. Tan, X., et al., *An experimental and simulation study on build thickness dependent microstructure for electron beam melted Ti–6Al–4V.* Journal of Alloys and Compounds, 2015. **646**: p. 303-309.
101. Antonysamy, A.A., J. Meyer, and P. Prangnell, *Effect of build geometry on the β-grain structure and texture in additive manufacture of Ti 6Al 4V by selective electron beam melting.* Materials characterization, 2013. **84**: p. 153-168.
102. Hrabe, N. and T. Quinn, *Effects of processing on microstructure and mechanical properties of a titanium alloy (Ti–6Al–4V) fabricated using electron beam melting (EBM), part 1: Distance from build plate and part size.* Materials Science and Engineering: A, 2013. **573**: p. 264-270.
103. Kobryn, P. and S. Semiatin. *Mechanical properties of laser-deposited Ti-6Al-4V*. in *Solid Freeform Fabrication Proceedings*. 2001. Austin.
104. Murr, L., et al., *Microstructures and mechanical properties of electron beam-rapid manufactured Ti–6Al–4V biomedical prototypes compared to wrought Ti–6Al–4V.* Materials characterization, 2009. **60**(2): p. 96-105.
105. Sun, Y., et al., *The influence of As-Built surface conditions on mechanical properties of Ti-6Al-4V additively manufactured by selective electron beam melting.* JOM, 2016. **68**(3): p. 791-798.
106. Tang, H., et al., *Microstructure, mechanical properties, and flatness of SEBM Ti-6Al-4V sheet in as-built and hot isostatically pressed conditions.* JOM, 2017. **69**(3): p. 466-471.
107. Wang, P., et al. *Effect of building height on microstructure and mechanical properties of big-sized Ti-6Al-4V plate fabricated by electron beam melting*. in *MATEC Web of Conferences*. 2015. EDP Sciences.
108. Sochalski-Kolbus, L., et al., *Comparison of residual stresses in Inconel 718 simple parts made by electron beam melting and direct laser metal sintering.* Metallurgical and Materials Transactions A, 2015. **46**(3): p. 1419-1432.
109. Gong, H., et al. *Defect morphology in Ti–6Al–4V parts fabricated by selective laser melting and electron beam melting*. in *24rd Annual International Solid Freeform Fabrication Symposium—An Additive Manufacturing Conference, Austin, TX, Aug*. 2013.
110. Mohammad, A., et al., *Effect of melt parameters on density and surface roughness in electron beam melting of gamma titanium aluminide alloy.* Rapid Prototyping Journal, 2017. **23**(3): p. 474-485.
111. Schwerdtfeger, J., R.F. Singer, and C. Körner, *In situ flaw detection by IR-imaging during electron beam melting.* Rapid Prototyping Journal, 2012. **18**(4): p. 259-263.
112. Abdeen, D.H., et al., *Effect of processing parameters of electron beam melting machine on properties of Ti-6Al-4V parts.* Rapid Prototyping Journal, 2016. **22**(3): p. 609-620.
113. Klingvall Ek, R., et al., *The effect of EBM process parameters upon surface roughness.* Rapid Prototyping Journal, 2016. **22**(3): p. 495-503.

114. Wang, P., et al., *Effects of Processing Parameters on Surface Roughness of Additive Manufactured Ti-6Al-4V via Electron Beam Melting.* Materials, 2017. **10**(10): p. 1121.
115. Mahale, T.R., *Electron Beam Melting of Advanced Materials and Structures, mass customization, mass personalization.* 2009.
116. Tammas-Williams, S., et al., *XCT analysis of the influence of melt strategies on defect population in Ti–6Al–4V components manufactured by Selective Electron Beam Melting.* Materials Characterization, 2015. **102**: p. 47-61.
117. De Formanoir, C., et al., *Electron beam melted Ti–6Al–4V: Microstructure, texture and mechanical behavior of the as-built and heat-treated material.* Materials Science and Engineering: A, 2016. **652**: p. 105-119.
118. Everhart, W., J. Dinardo, and C. Barr, *The Effect of Scan Length on the Structure and Mechanical Properties of Electron Beam-Melted Ti-6Al-4V.* Metallurgical and Materials Transactions A, 2017. **48**(2): p. 697-705.
119. Scharowsky, T., A. Bauereiß, and C. Körner, *Influence of the hatching strategy on consolidation during selective electron beam melting of Ti-6Al-4V.* The International Journal of Advanced Manufacturing Technology, 2017: p. 1-10.
120. Scharowsky, T., et al., *Influence of the scanning strategy on the microstructure and mechanical properties in selective electron beam melting of Ti–6Al–4V.* Advanced Engineering Materials, 2015. **17**(11): p. 1573-1578.
121. Juechter, V., et al., *Processing window and evaporation phenomena for Ti–6Al–4V produced by selective electron beam melting.* Acta Materialia, 2014. **76**: p. 252-258.
122. Kirchner, A., et al., *Process window for electron beam melting of Ti-6Al-4V.* Powder Metallurgy, 2015. **58**(4): p. 246-249.
123. ASTM, *Standard Specification for Wrought Titanium-6Aluminum-4Vanadium ELI (Extra Low Interstitial) Alloy for Surgical Implant Applications (UNS R56401)*, in *Standard F136*. 2013, ASTM International.
124. ASTM, *Standard Specification for Titanium and Titanium Alloy Bars and Billets*, in *Standard B348*. 2013, ASTM International.
125. Joshi, G.V., et al., *Fatigue testing of electron beam-melted Ti-6Al-4V ELI alloy for dental implants.* Journal of Biomedical Materials Research Part B: Applied Biomaterials, 2013. **101**(1): p. 124-130.
126. Seifi, M., et al., *Evaluation of orientation dependence of fracture toughness and fatigue crack propagation behavior of as-deposited ARCAM EBM Ti-6Al-4V.* Jom, 2015. **67**(3): p. 597-607.
127. Zhai, Y., H. Galarraga, and D.A. Lados, *Microstructure, static properties, and fatigue crack growth mechanisms in Ti-6Al-4V fabricated by additive manufacturing: LENS and EBM.* Engineering failure analysis, 2016. **69**: p. 3-14.
128. Facchini, L., et al., *Microstructure and mechanical properties of Ti-6Al-4V produced by electron beam melting of pre-alloyed powders.* Rapid Prototyping Journal, 2009. **15**(3): p. 171-178.

129. Greitemeier, D., et al., *Fatigue performance of additive manufactured TiAl6V4 using electron and laser beam melting.* International Journal of Fatigue, 2017. **94**: p. 211-217.
130. Kahlin, M., H. Ansell, and J. Moverare, *Fatigue behaviour of notched additive manufactured Ti6Al4V with as-built surfaces.* International Journal of Fatigue, 2017. **101**: p. 51-60.
131. Greitemeier, D., et al., *Effect of surface roughness on fatigue performance of additive manufactured Ti–6Al–4V.* Materials Science and Technology, 2016. **32**(7): p. 629-634.
132. Atkinson, H. and S. Davies, *Fundamental aspects of hot isostatic pressing: an overview.* Metallurgical and Materials Transactions A, 2000. **31**(12): p. 2981-3000.
133. Lograsso, B. and D. Koss, *Densification of titanium powder during hot isostatic pressing.* Metallurgical and Materials Transactions A, 1988. **19**(7): p. 1767-1773.
134. Morrissey, R., D. McDowell, and T. Nicholas, *Frequency and stress ratio effects in high cycle fatigue of Ti-6Al-4V.* International Journal of Fatigue, 1999. **21**(7): p. 679-685.
135. Karl, M. and J.R. Kelly, *Influence of loading frequency on implant failure under cyclic fatigue conditions.* Dental materials, 2009. **25**(11): p. 1426-1432.
136. Hidetoshi, S., S. Hiroyuki, and T. Kiyotaka, *Surface crack initiation in pure titanium under various stress frequencies.* Engineering fracture mechanics, 1994. **49**(2): p. 317-321.
137. Sakamoto, H., S. Takezono, and T. Nakano, *Effect of stress frequency on fatigue crack initiation in titanium.* Engineering Fracture Mechanics, 1988. **30**(3): p. 373-382.
138. Satoh, M., *Effect of stress frequency on fatigue crack propagation in titanium.* Journal of Engineering Materials and Technology, 1982. **104**: p. 257.
139. Chan, K.S., et al., *Fatigue life of titanium alloys fabricated by additive layer manufacturing techniques for dental implants.* Metallurgical and Materials Transactions A, 2013. **44**(2): p. 1010-1022.
140. Du, D.X., et al. *The effects of machined workpiece surface integrity on the fatigue life of TC21 titanium alloy*. in *Advanced Materials Research*. 2012. Trans Tech Publ.
141. Zhu, L., et al., *Effect of Surface Roughness on Very High Cycle Fatigue Behavior of Ti-6Al-4V Alloy.* Acta Metall Sin, 2016. **52**(5): p. 583-591.
142. Che-Haron, C. and A. Jawaid, *The effect of machining on surface integrity of titanium alloy Ti–6%Al–4%V.* Journal of Materials Processing Technology, 2005. **166**(2): p. 188-192.
143. Tokaji, K., et al., *Fatigue behaviour of beta Ti-22V-4Al alloy subjected to surface-microstructural modification.* Journal of materials science, 2003. **38**(6): p. 1153-1159.
144. Witkin, D.B., T.V. Albright, and D.N. Patel, *Empirical Approach to Understanding the Fatigue Behavior of Metals Made Using Additive Manufacturing.* Metallurgical and Materials Transactions A, 2016. **47**(8): p. 3823-3836.

145. Jamshidinia, M., et al., *Fatigue properties of a dental implant produced by electron beam melting®(EBM).* Journal of Materials Processing Technology, 2015. **226**: p. 255-263.
146. Mann, J.Y., *Fatigue of materials.* CAMBRIDGE UNIVERSITY PRESS, LONDON. 1967. 155 P, 1967.
147. Van Hooreweder, B., et al., *Improving the fatigue performance of porous metallic biomaterials produced by Selective Laser Melting.* Acta biomaterialia, 2017. **47**: p. 193-202.
148. Kahlin, M., H. Ansell, and J. Moverare, *Fatigue behaviour of additive manufactured Ti6Al4V, with as-built surfaces, exposed to variable amplitude loading.* International Journal of Fatigue, 2017. **103**: p. 353-362.
149. Crupi, V., et al., *Influence of microstructure [alpha+ beta and beta] on very high cycle fatigue behaviour of Ti-6Al-4V alloy.* International Journal of Fatigue, 2017. **95**: p. 64-75.
150. Oberwinkler, B., et al., *Four Point Bending Fatigue Tests of Forged Ti 6Al 4V.* Materials Testing, 2009. **51**(9): p. 580-586.
151. Kirchner, A., et al., *Mechanical properties of Ti-6Al-4V fabricated by electron beam melting.* Key Engineering Materials, 2016. **704**.
152. Hemphill, M.A., et al., *Fatigue behavior of Al 0.5 CoCrCuFeNi high entropy alloys.* Acta Materialia, 2012. **60**(16): p. 5723-5734.
153. Svensson, M. and U. Ackelid. *Influence of Interstitial Elements on the Mechanical Properties of Ti-6Al-4V Produced with Electron Beam Melting*. in *Materials Science and Technology Conference*. 2011. Columbus, OH.
154. Peter, W.H., et al., *Understanding the Role of Hot Isostatic Pressing Parameters on the Microstructural Evolution of Ti-6Al-4V and Inconel 718 Fabricated by Electron Beam Melting*. 2015, Oak Ridge National Laboratory (ORNL); Manufacturing Demonstration Facility (MDF).
155. *Standard Specification for Additive Manufacturing Titanium-6 Aluminum-4 Vanadium with Powder Bed Fusion*. 2014, ASTM International.
156. Vander Voort, G. and A. Roosz, *Measurement of the interlamellar spacing of pearlite.* Metallography, 1984. **17**(1): p. 1-17.
157. Zhai, T., et al., *A self-aligning four-point bend testing rig and sample geometry effect in four-point bend fatigue.* International Journal of Fatigue, 1999. **21**(9): p. 889-894.
158. Nonaka, I., S. Setowaki, and Y. Ichikawa, *Effect of load frequency on high cycle fatigue strength of bullet train axle steel.* International Journal of Fatigue, 2014. **60**: p. 43-47.
159. Gallagher, J., et al., *Advanced high cycle fatigue (HCF) life assurance methodologies*. 2004, DAYTON UNIV OH RESEARCH INST.
160. Musuva, J. and J. Radon, *The effect of stress ratio and frequency on fatigue crack growth.* Fatigue & Fracture of Engineering Materials & Structures, 1979. **1**(4): p. 457-470.
161. Caton, M., et al., *Stress ratio effects on small fatigue crack growth in Ti–6Al–4V.* International Journal of Fatigue, 2012. **38**: p. 36-45.

162. Wanhill, R. and S. Barter, *Short/Small Fatigue Crack Growth*, in *Fatigue of Beta Processed and Beta Heat-treated Titanium Alloys*. 2012, Springer. p. 27-40.
163. Barter, S., M. Burchill, and M. Jones, *Measured fatigue crack growth increments versus predictions for small cracks in 7XXX aluminium alloys.* International Journal of Fatigue, 2017. **105**: p. 144-159.
164. De Matos, P., et al., *Reconstitution of fatigue crack growth in Al-alloy 2024-T3 open-hole specimens using microfractographic techniques.* Engineering fracture mechanics, 2005. **72**(14): p. 2232-2246.
165. Koike, M., et al., *Evaluation of titanium alloy fabricated using electron beam melting system for dental applications.* Journal of Materials Processing Technology, 2011. **211**(8): p. 1400-1408.
166. Wang, P., et al., *Study of Direct Fabrication of a Ti-6Al-4V Impeller on a Wrought Ti-6Al-4V Plate by Electron Beam Melting.* JOM, 2017. **69**(12): p. 2738-2744.
167. Tan, X., et al., *Revealing martensitic transformation and α/β interface evolution in electron beam melting three-dimensional-printed Ti-6Al-4V.* Scientific Reports, 2016. **6**: p. 26039.
168. Askeland, D.R. and P.P. Phule, *The Science and Engineering of Materials*. 5th ed. 2005, USA: Thompson Publishers.
169. Rack, H. and J. Qazi, *Titanium alloys for biomedical applications.* Materials Science and Engineering: C, 2006. **26**(8): p. 1269-1277.
170. SUI, Y.-w., et al., *Microstructures and hardness of Ti-6Al-4V alloy staging castings under centrifugal field.* Transactions of Nonferrous Metals Society of China, 2008. **18**(2): p. 291-296.
171. Mitzner, S., et al., *Grain refinement of freeform fabricated Ti-6Al-4V alloy using beam/arc modulation.* 2012.
172. Seifi, M., et al. *Process mapping, fracture and fatigue behavior of Ti-6Al-4V produced by EBM additive manufacturing*. in *Ti-2015: The 13th World Conference on Titanium*. 2016.
173. Wang, P., et al. *Recent progress of additive manufactured Ti-6Al-4V by electron beam melting*. in *Proceedings of the 2016 Annual International Solid Freeform Fabrication Symposium (SFF Symp 2016), Austin, TX, USA*. 2016.
174. Liu, C., et al., *Microstructure, texture and mechanical studies of an inconspicuous shear band formed during hot compression of Ti-6Al-4V alloy.* Materials Science and Engineering: A, 2017. **698**: p. 18-26.
175. Williams, J., R. Baggerly, and N. Paton, *Deformation behavior of HCP Ti-Al alloy single crystals.* Metallurgical and Materials Transactions A, 2002. **33**(3): p. 837-850.
176. Bridier, F., P. Villechaise, and J. Mendez, *Analysis of the different slip systems activated by tension in a α/β titanium alloy in relation with local crystallographic orientation.* Acta Materialia, 2005. **53**(3): p. 555-567.
177. Hertzberg, R.W., *Deformation and fracture mechanics of engineering materials.* 1989.

178. Welsch, G. and W. Bunk, *Deformation modes of the α-phase of Ti-6Al-4V as a function of oxygen concentration and aging temperature.* Metallurgical Transactions A, 1982. **13**(5): p. 889-899.
179. Kwon, J., et al., *Characterization of deformation anisotropies in an α-Ti alloy by nanoindentation and electron microscopy.* Acta Materialia, 2013. **61**(13): p. 4743-4756.
180. Ladani, L., J. Razmi, and S.F. Choudhury, *Mechanical anisotropy and strain rate dependency behavior of Ti6Al4V produced using E-beam additive fabrication.* Journal of Engineering Materials and Technology, 2014. **136**(3): p. 031006.
181. Markovsky, P. and V. Bondarchuk, *Influence of Strain Rate, Microstructure and Chemical and Phase Composition on Mechanical Behavior of Different Titanium Alloys.* Journal of Materials Engineering and Performance, 2017. **26**(7): p. 3431-3449.
182. Lee, W. and S. Huang, *Deformation and failure behaviour of Ti-6Al-4V alloy under high rate shear loading.* WIT transactions on modelling and simulation, 2005. **40**.
183. Salzbrenner, B.C., et al., *High-throughput stochastic tensile performance of additively manufactured stainless steel.* Journal of Materials Processing Technology, 2017. **241**: p. 1-12.
184. Wilson-Heid, A.E., et al., *Quantitative relationship between anisotropic strain to failure and grain morphology in additively manufactured Ti-6Al-4V.* Materials Science and Engineering: A, 2017. **706**: p. 287-294.
185. Bruno, J., A. Rochman, and G. Cassar, *Effect of Build Orientation of Electron Beam Melting on Microstructure and Mechanical Properties of Ti-6Al-4V.* Journal of Materials Engineering and Performance, 2017. **26**(2): p. 692-703.
186. Zhao, X., et al., *Comparison of the microstructures and mechanical properties of Ti–6Al–4V fabricated by selective laser melting and electron beam melting.* Materials & Design, 2016. **95**: p. 21-31.
187. Carroll, B.E., T.A. Palmer, and A.M. Beese, *Anisotropic tensile behavior of Ti–6Al–4V components fabricated with directed energy deposition additive manufacturing.* Acta Materialia, 2015. **87**: p. 309-320.
188. Gil, F., et al., *Formation of α-Widmanstätten structure: effects of grain size and cooling rate on the Widmanstätten morphologies and on the mechanical properties in Ti6Al4V alloy.* Journal of Alloys and Compounds, 2001. **329**(1-2): p. 142-152.
189. Sun, Y., et al., *Layer Additive Production or Manufacturing of Thick Sections of Ti-6Al-4V by Selective Electron Beam Melting (SEBM).* JOM, 2017. **69**(10): p. 1836-1843.
190. Inc., A.S.M. *Titanium Ti-6Al-4V (Grade 5), Annealed*. 2017; Available from: http://asm.matweb.com/search/SpecificMaterial.asp?bassnum=mtp641.
191. Dipen, B., B. Ketul, and P. Dipal, *Stress Concentration Factor Converts Into Stress Intensity Factor Using ANSYS.* European Journal of Advances in Engineering and Technology, 2015. **2**(1): p. 46-49.
192. Kim, N.-H., B.V. Sankar, and N.H. Kim, *Introduction to finite element analysis and design*. 2009: Wiley.

193. Riley, W.F., L.D. Sturges, and D.H. Morris, *Statics and mechanics of materials: an integrated approach*. 1995: John Wiley & Sons Inc.
194. Chan, K.S., *Characterization and analysis of surface notches on Ti-alloy plates fabricated by additive manufacturing techniques.* Surface Topography: Metrology and Properties, 2015. **3**(4): p. 044006.
195. Peterson, R.E. and R. Peterson, *Stress concentration factors*. 1967: John Wiley and Sons.
196. Campbell, I., D. Bourell, and I. Gibson, *Additive manufacturing: rapid prototyping comes of age.* Rapid prototyping journal, 2012. **18**(4): p. 255-258.
197. Faludi, J., et al., *Comparing environmental impacts of additive manufacturing vs traditional machining via life-cycle assessment.* Rapid Prototyping Journal, 2015. **21**(1): p. 14-33.
198. Ralph, W.C., et al., *Fatigue performance of production-quality aircraft fastener holes.* International journal of fatigue, 2007. **29**(7): p. 1319-1327.
199. Liu, J., et al., *The effect of holes quality on fatigue life of open hole.* Materials Science and Engineering: A, 2007. **467**(1): p. 8-14.
200. Sun, D., et al., *Hole-making and its Impact on the Fatigue Response of Ti-6AL-4V Alloy.* Procedia CIRP, 2016. **56**: p. 289-292.
201. Bagehorn, S., J. Wehr, and H. Maier, *Application of mechanical surface finishing processes for roughness reduction and fatigue improvement of additively manufactured Ti-6Al-4V parts.* International Journal of Fatigue, 2017. **102**: p. 135-142.
202. Dirgantara, T. and M. Aliabadi, *Stress intensity factors for cracks in thin plates.* Engineering fracture mechanics, 2002. **69**(13): p. 1465-1486.
203. Kasperovich, G. and J. Hausmann, *Improvement of fatigue resistance and ductility of TiAl6V4 processed by selective laser melting.* Journal of Materials Processing Technology, 2015. **220**: p. 202-214.
204. Virkler, D.A., B. Hillberry, and P. Goel, *The statistical nature of fatigue crack propagation.* Journal of Engineering Materials and Technology, 1979. **101**(2): p. 148-153.
205. Irving, P. and C. Beevers, *Microstructural influences on fatigue crack growth in Ti□ 6Al□ 4V.* Materials Science and Engineering, 1974. **14**(3): p. 229-238.
206. Shunmugavel, M., A. Polishetty, and G. Littlefair, *Microstructure and Mechanical Properties of Wrought and Additive Manufactured Ti-6Al-4 V Cylindrical Bars.* Procedia Technology, 2015. **20**: p. 231-236.
207. Verdhan, N., et al., *Effect of microstructure on the fatigue crack growth behaviour of a near-α Ti alloy.* International Journal of Fatigue, 2015. **74**: p. 46-54.
208. Liu, Q.C., et al. *The effect of manufacturing defects on the fatigue behaviour of Ti-6Al-4V specimens fabricated using selective laser melting*. in *Advanced Materials Research*. 2014. Trans Tech Publ.
209. Xu, Z., W. Wen, and T. Zhai, *Effects of pore position in depth on stress/strain concentration and fatigue crack initiation.* Metallurgical and Materials Transactions A, 2012. **43**(8): p. 2763-2770.

210. Scharowsky, T., et al., *Melt pool dynamics during selective electron beam melting.* Applied Physics A, 2014. **114**(4): p. 1303-1307.
211. Weißmann, V., et al., *Comparison of single Ti6Al4V struts made using selective laser melting and electron beam melting subject to part orientation.* Metals, 2017. **7**(3): p. 91.
212. Leuders, S., et al., *On the mechanical behaviour of titanium alloy TiAl6V4 manufactured by selective laser melting: Fatigue resistance and crack growth performance.* International Journal of Fatigue, 2013. **48**: p. 300-307.
213. Dubey, A.K. and V. Yadava, *Laser beam machining—a review.* International Journal of Machine Tools and Manufacture, 2008. **48**(6): p. 609-628.
214. Mohammad, A., M.K. Mohammed, and A.M. Alahmari, *Effect of laser ablation parameters on surface improvement of electron beam melted parts.* The International Journal of Advanced Manufacturing Technology, 2016. **87**(1-4): p. 1033-1044.
215. Vorberger, T.V. and J. Raja. *National Institute of Standards and Technology: Calibration*. 1990; Available from: www. nist.gov/calibrations/upload/89-4088.pdf.
216. Sidambe, A., I. Todd, and P. Hatton, *Effects of build orientation induced surface modifications on the in vitro biocompatibility of electron beam melted Ti6Al4V.* Powder Metallurgy, 2016. **59**(1): p. 57-65.
217. Singh, R.P. and S. Singhal, *Rotary ultrasonic machining: a review.* Materials and Manufacturing Processes, 2016. **31**(14): p. 1795-1824.
218. Ahmed, N., et al., *Electron beam melting of titanium alloy and surface finish improvement through rotary ultrasonic machining.* The International Journal of Advanced Manufacturing Technology, 2017. **92**(9-12): p. 3349-3361.
219. Kuruc, M., T. Vopát, and J. Peterka, *Surface roughness of poly-crystalline cubic boron nitride after rotary ultrasonic machining.* Procedia Engineering, 2015. **100**: p. 877-884.
220. Algardh, J.K., et al., *Thickness dependency of mechanical properties for thin-walled titanium parts manufactured by Electron Beam Melting (EBM)®.* Additive Manufacturing, 2016. **12**: p. 45-50.
221. AP&C. *Designed for Additive Manufacturing*. 2017; Available from: http://advancedpowders.com/our-plasma-atomized-powders/spherical-powders-designed-for-additive-manufacturing/.
222. Karlsson, J., et al., *Characterization and comparison of materials produced by Electron Beam Melting (EBM) of two different Ti–6Al–4V powder fractions.* Journal of Materials Processing Technology, 2013. **213**(12): p. 2109-2118.
223. Cordero, Z.C., et al., *Powder bed charging during electron-beam additive manufacturing.* Acta Materialia, 2017. **124**: p. 437-445.
224. Morton, P.A., et al., *Enhancement of low-cycle fatigue performance from tailored microstructures enabled by electron beam melting additive manufacturing technology.* Journal of Mechanical Design, 2015. **137**(11): p. 111412.

225. Dehoff, R., et al., *Site specific control of crystallographic grain orientation through electron beam additive manufacturing.* Materials Science and Technology, 2015. **31**(8): p. 931-938.
226. Sackett, E., L. Germain, and M.R. Bache, *Crystal plasticity, fatigue crack initiation and fatigue performance of advanced titanium alloys.* International Journal of Fatigue, 2007. **29**(9): p. 2015-2021.
227. Zhai, T., A. Wilkinson, and J. Martin, *A crystallographic mechanism for fatigue crack propagation through grain boundaries.* Acta materialia, 2000. **48**(20): p. 4917-4927.
228. Pilchak, A., et al., *Low ΔK faceted crack growth in titanium alloys.* International Journal of Fatigue, 2009. **31**(5): p. 989-994.
229. Oberwinkler, B., M. Riedler, and W. Eichlseder, *Importance of local microstructure for damage tolerant light weight design of Ti–6Al–4V forgings.* International Journal of Fatigue, 2010. **32**(5): p. 808-814.
230. Pilchak, A., M. Juhas, and J. Williams, *Microstructural changes due to friction stir processing of investment-cast Ti-6Al-4V.* Metallurgical and materials Transactions A, 2007. **38**(2): p. 401-408.
231. Pilchak, A., et al., *Friction stir processing of investment-cast Ti-6Al-4V: Microstructure and properties.* Metallurgical and Materials Transactions A, 2008. **39**(7): p. 1519-1524.
232. Günther, J., et al., *Fatigue life of additively manufactured Ti–6Al–4V in the very high cycle fatigue regime.* International Journal of Fatigue, 2017. **94, Part 2**: p. 236-245.
233. Brandl, E., C. Leyens, and F. Palm. *Mechanical properties of additive manufactured Ti-6Al-4V using wire and powder based processes*. in *IOP conference series: materials science and engineering*. 2011. IOP Publishing.
234. Mohammadhosseini, A., et al., *Microstructure and mechanical properties of Ti–6Al–4V manufactured by electron beam melting process.* Materials Research Innovations, 2013. **17**(sup2): p. s106-s112.
235. Peters, J. and G. Lütjering, *Comparison of the fatigue and fracture of α+ β and β titanium alloys.* Metallurgical and materials transactions A, 2001. **32**(11): p. 2805-2818.

APPENDIX

Table 7. Fatigue Data Reference Chart

Symbol	Trend Line Pattern	Reference	Arcam Machine	Heat Treatment	Surface Condition	Build Orientation
		[90]	S12	As-Built	Machined	Vertical
		[90]	S12	Stress Relieved, 5 hr. at 650°C in air, furnace cooled	Machined	Vertical
		[90]	S12	HIP, 2 hr. at 900°C at 100 MPa under Ar, 12 C/min. heating and cooling rate	Machined	Vertical
		[129]	A2	Annealed at 710 C for 2 hr. in vacuum	As-built	Vertical
		[129]	A2	Annealed at 710 C for 2 hr. in vacuum	Machined	Vertical
		[129]	A2	HIP at 920° C at 100 MPa under Ar	As-built	Vertical
		[129]	A2	HIP at 920° C at 100 MPa under Ar	Machined	Vertical
		[84]	S400	As-Built	As-Built	Vertical
		[84]	S400	As-Built	As-Built	Horizontal
		[84]	S400	As-Built	Machined	Vertical
		[84]	S400	As-Built	Machined	Horizontal
		[232]	A2X	As Built	Machined & Polished	Vertical
		[83]	-	As-Built	Machined	Vertical
		[83]	-	HIP for 2 hr. at 920C at 100 MPa in Ar	Machined	Vertical
		[83]	-	As-Built	Machined	Horizontal
		[83]	-	HIP for 2 hr. at 920C at 100 MPa in Ar	Machined	Horizontal
		[85]	A1	As-Built	As-Built	Vertical
		[85]	A1	As-Built	As-Built	Horizontal
		[85]	A1	As-Built	Machined	Vertical
		[85]	A1	As-Built	Machined	Horizontal

Table 7 Continued. Fatigue Data Reference Chart

Symbol	Trend Line Pattern	Reference	Arcam Machine	Heat Treatment	Surface Condition	Build Orientation
		[85]	A1	As-Built	Machined and Shot Peened	Vertical
		[85]	A1	As-Built	Machined and Shot Peened	Horizontal
		[233]	A2	HIP for 4 hr. at 843°C at 100 MPa, furnace cooled	Machined	Vertical
		[154]	Q10	As-Built	As-Built	Vertical
		[154]	Q10	As-Built	As-Built	Horizontal/ Transverse
		[144]	S12	HIP for 2 hr. at 100 MPa, 900C	As-Built	Vertical
		[144]	S12	HIP for 2 hr. at 100 MPa, 900C	As-Built	Vertical
		[144]	S12	HIP for 2 hr. at 100 MPa, 900C	As-Built	Vertical
		[234]	A1	As-Built	Machined	Vertical
		[234]	A1	HIP at 1034 bar at 900°C for 2 hr.	Machined	Vertical
		[53, 55]	-	Lamellar	-	-
		[55, 235]	-	Bimodal	-	-

Burgers Orientation Relation – Example Variant

The following describes the orientation relationship between the solid-state β (bcc) and α (hcp) phase transformation. The two phases are related such that

$$(0001)_\alpha \ || \ (110)_\beta$$
$$\langle 2\bar{1}\bar{1}0\rangle_\alpha \ || \ \langle 1\bar{1}1\rangle_\beta$$

Where parenthesis denote planes and chevrons directions. Schematics of the parallel planes in their respective crystal structures and a schematic of the orientation relationship viewed from the *c* direction are provided below. One of the 12 varianets is shown in Figure 69 is adapted from [41].

$$\langle \bar{1}1\bar{1}\rangle_\beta \ ||$$
$$\langle \bar{2}110\rangle_\alpha$$

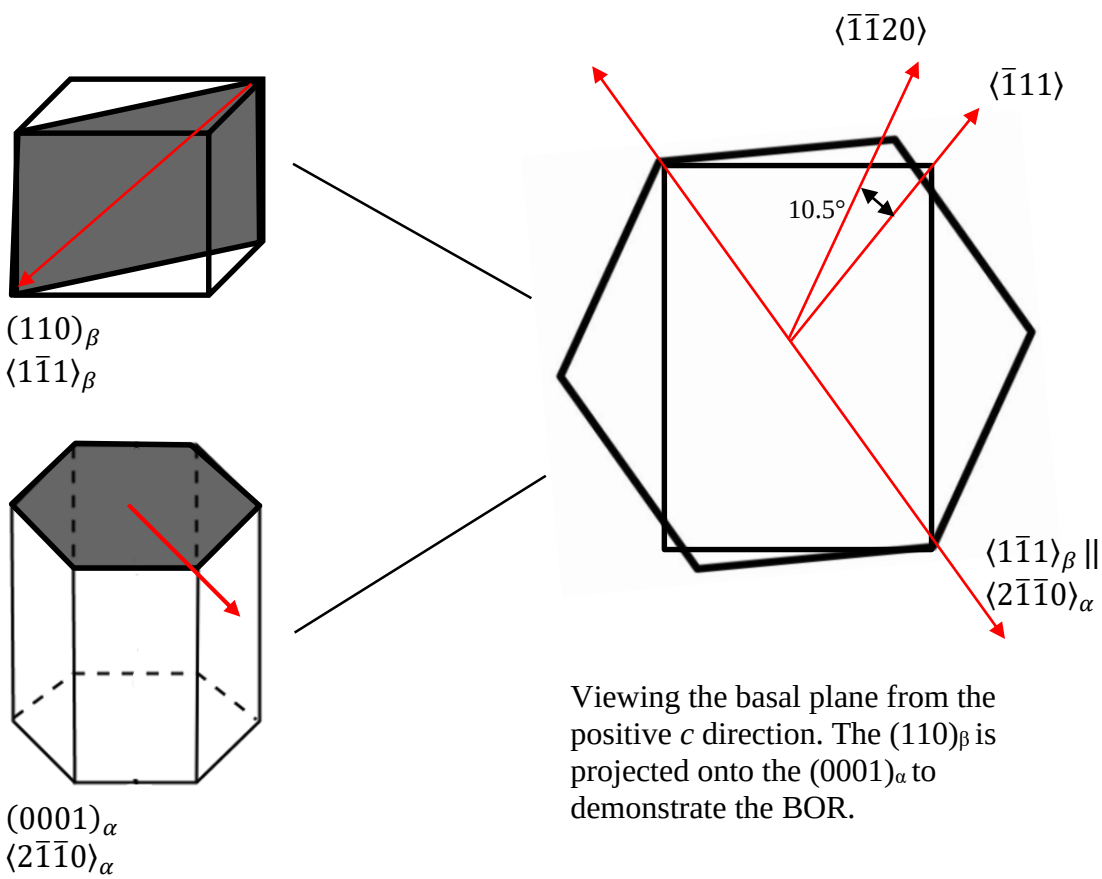

Figure 69. Schematic of an example variant of the Burgers Orientation Relationship adapted from [41].

Crack Growth Rate Calculation Example – Secant Method, Horizontal Sample

The following outlines the crack growth ($\frac{da}{dN}$) calculation using the Secant method and provides and example. The equations and method are outlined by Virkler [204]. The method is shown schematically in Figure 70.

Average Crack Length, $\bar{a}_i$

$$\bar{a}_i = \frac{(a_i + a_{i+1})}{2}$$

Slope of the line connecting 2 adjacent data points approximates the growth rate, $\frac{da}{dN}$

$$\frac{da}{dN_i} = \frac{(a_{i+1} - a_i)}{(N_{i+1} - N_i)}$$

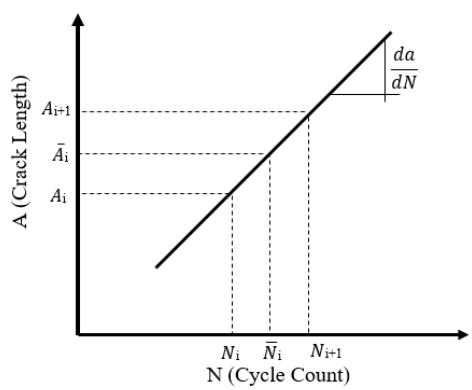

Figure 70. Schematic of the Secant Method for calculating fatigue crack growth rate. Adapted from [204].

Table 8. Example Calculations for Crack Growth Rate, da/dN.

Cycle	Crack Length, a_i (μm)	$a_{(i+1)}$	$a_{(i+1)}$-a_i	N_i	$N_{(i+1)}$	$N_{(i+1)}$-N_i	da/dN_i (μm/cycle)	average crack length (μm)
0	0	0	0	0	10000	10000	0	0
10000	0	507.5	507.5	10000	20000	10000	0.05075	253.75
20000	507.5	2527.5	2020	20000	30000	10000	0.202	1517.5
30000	2527.5	4641.5	2114	30000	35000	5000	0.4228	3584.5
35000	4641.5	9791.7	5150.2	35000	39389	4389	1.17	7216.6
39389	9791.7	0	x	39389	x	x	x	x

VITA

Andrew H. Chern was born September, 24 1991 in Nashville, Tennessee. He received his Bachelor of Science degree in Materials Science and Engineering from the University of Wisconsin in 2015. Upon completion, Andrew interned at J&L Fiber Services, A PCC Company in Waukesha, Wisconsin before returning to school to study Mechanical Engineering at the University of Tennessee, Knoxville. There he worked as a teaching assistant and graduate researcher while working to complete his Master of Science degree.